

THESIS APPROVAL

The abstract and thesis of Patrick J. Bardel for the Master of Science in Geography were presented May 10, 2001, and accepted by the thesis committee and the department.

COMMITTEE APPROVALS:

Andrew G. Fountain, Chair

Daniel Johnson

Ric Vrana

Roy Koch
Representative of the Office of Graduate Studies

DEPARTMENT APPROVAL

Teresa Bulman, Chair

ABSTRACT

An abstract of the thesis of Patrick J. Bardel for the Master of Science in Geography presented May 10, 2001.

Title: Surface Mapping of Polar Glaciers Using Synthetic Aperture Radar.

Synthetic aperture radar (SAR) images were acquired of Taylor Valley, Antarctica in January 1999 in coordination with ground-based measurements to assess SAR detection of the snowline on dry polar glaciers. I anticipated significant penetration of the radar wave resulting in an offset of the SAR detected snowline relative to the true snowline, results indicated no detectable displacement of the SAR snowline. Results showed that snow depths of 15 cm over ice can be detected on the imagery. I hypothesize that the optical depth of thin snowpacks is enhanced by reflection and refraction of the radar beam by internal snow layers. The enhanced optical depth increases the volume scattering and thereby enhances backscatter sufficiently to be detected by the SAR. Consequently, SAR imagery may be used directly to image the position of transient snowlines in dry polar regions. Once a snowline is established using SAR, its variability can be measured over time and interpretations on changes on temperature and snowfall can be made. This information can be used to provide snowline data for incorporation into ice sheet climate models.

SURFACE MAPPING OF POLAR
GLACIERS USING SYNTHETIC APERTURE RADAR.

by

PATRICK J. BARDEL

A thesis submitted in partial fulfillment of the
requirements for the degree of

MASTER OF SCIENCE
in
GEOGRAPHY

Portland State University
2001

DEDICATION

This thesis is dedicated to my family. To my parents Don and Rose Bardel for their financial and moral support, and to my Daughter Aurelia Rose Bardel for her unconditional love and felicitousness.

ACKNOWLEDGEMENTS

I would like to express my appreciation to Dr. Andrew G. Fountain for his guidance throughout the course of this thesis. In addition I would like to thank William Abernathy for his invaluable aid as proofreader and reviewer. I would like to thank Jim Stapleton for his inestimable programming aid in getting the terrain correction to work. I would especially like to thank my review committee, Dr. Ric Vrana, Teresa Bulman, Roy Koch, and Dan Johnson.

Numerous people helped with this thesis that I have never had the privilege meeting but with whom I have corresponded frequently via email. Thanks to Dr. Dorothy Hall from NASA for the Synthetic Aperture Radar (SAR) data used in the thesis. Thanks to Dorothy Corbett, Tom Logan, and Chris Wyatt from The Alaska SAR Facility in helping Jim Stapleton and I to get the "Terrcorr" terrain correction to run. Thanks to Ron Kwok from the Jet Propulsion Laboratory for terrain correcting the Radarsat ScanSAR image and explanations about SAR and terrain correction. Thanks to Karen Lewis from University of Colorado for her opportune solution in figuring reflector inclination angle. Thanks to Dr. Ken Jezek and Hongxing Liu from Ohio State University for help with the digital elevation model.

TABLE OF CONTENTS

	PAGE
DEDICATION	<i>i</i>
ACKNOWLEDGEMENTS	<i>ii</i>
LIST OF TABLES	<i>vi</i>
LIST OF FIGURES.....	<i>vii</i>
CHAPTER	
I INTRODUCTION.....	1
II SITE DESCRIPTION	6
McMurdo Dry Valleys Long Term Ecological Research (LTER)	10
III SYNTHETIC APERTURE RADAR THEORY	12
Synthetic Aperture Radar Principles	14
Radar Distortions and Terrain Corrections	21
Radar Backscatter.....	23
Radar Penetration	27
SAR Platforms.....	28
Application of SAR to Snow and Ice	29
Radar Zones.....	32
IV METHODOLOGY OF THE DATA COLLECTION.....	37
Objective	37

	Experimental setup.....	37
	The Digital Elevation Model.....	42
	Surface-Based Measurements	42
	The Measured Surface Variables	48
V	RESULTS OF THE FIELD MEASUREMENTS.....	53
	Imagery.....	53
	Transects.....	56
VI	IMAGE PROCESSING	67
	Radiometric Calibration	68
	Foreshortening and Geocoding	69
	The Digital Elevation Model.....	71
	Terrcorr Steps.....	71
	Radarsat Terrain Correction.....	72
	Peculiar Characteristics of the Corrected SAR Images.	75
	Reflector Backscatter Shape of the ERS-2 Image.....	80
	Comparison of ERS-2 Images Between Manually Correlated, and Auto-Correlated	81
	Radarsat Image Evaluation.....	89
	Comparison of Radarsat Images Between Corrected and Un-Corrected	91
VII	IMAGE ANALYSIS	96
	Surface Brightness Variation	97
	Why Did the SAR Snowline Match With the actual Snowline?.....	107

	Comparison of Radarsat and ERS-2.....	117
	Howard Glacier	124
	Analysis of Other Features of the Valley	126
	Summary	141
VIII	DISCUSSION AND CONCLUSIONS.....	144
	Experiences and Recommendations.....	147
	Recommendation for Future Work	148
	REFERENCES.....	150
	APPENDICES	
A	McMurdo Dry Valley Long-Term Ecological Research Snow Pit Data for Commonwealth and Howard Glaciers.....	158
B	Transect Field Data for Commonwealth and Howard Glaciers.....	167
C	Full Description of Steps to Acquire Programs, Convert Data, and Run the Terrcorr Terrain Correction Program	182
D	November 2000 Snow Depths Near Sakes 19 and 21	188

LIST OF TABLES

	PAGE
Table 3.1: Radar Frequency Designations	14
Table 3.2: Dielectric values of some materials	27
Table 3.3. Radar instrument specifications for Radarsat, and ERS-2.	29
Table 3.4. Snow dielectric properties and penetration depth for wet and dry snow.	31
Table 3.5: The five glacier radar zones. SAR brightness and surface characteristics are described relative to facie	35
Table 5.1: Cover and snow depth at sites near the snowline.....	65
Table 6.1: The distance between reflectors on the ERS-2 image (m).....	83
Table 6.2: Azimuth of the reflectors on the ERS-2 image.	84
Table 6.3: The distance between reflectors on the Radarsat image (m).	92
Table 6.4: Azimuth of the reflectors on the ERS-2 image.	92
Table 7.1: Supervised and unsupervised SAR classification categories.....	103
Table 7.2: Temperatures at the Commonwealth Meteorological Station.....	109
Table 7.3: Reflection coefficients for the layers at Stakes 12 and 14.	114
Table 7.4: Comparison of SAR features.	128
Table 7.5: Brightness comparison of lake ice and nearby glacier ice.	140
Table 7.6: Average weekly temperature comparison between lake and glacier.	141

LIST OF FIGURES

	PAGE
Figures follow at the end of each chapter.	
Figure 1.1: Site maps.....	7
Figure 3.1: The electromagnetic spectrum.....	13
Figure 3.2: Operating principle of a SAR	15
Figure 3.3: Real antenna positions forming a synthetic aperture.....	17
Figure 3.4: Effect of pulse length.....	19
Figure 3.5: Slant and ground range	22
Figure 3.6: SAR geometric distortions.....	22
Figure 3.7: Diffuse, specular, corner, and volume reflection.....	24
Figure 3.8: Benson's generalized cross-section of glacier facies	34
Figure 4.1: ERS-2 and Radarsat look angles.....	38
Figure 4.2: Optical depth vs. actual depth.....	38
Figure 4.3: Snow stakes on Commonwealth and Howard Glaciers.....	39
Figure 4.4: Digital Elevation Model (DEM) of Southern Victoria Land.....	43
Figure 4.5: Ray diagrams of the reflections in a dihedral and a triangular trihedral corner reflector.....	45
Figure 4.6: Inclination angle	45
Figure 4.7: A trihedral corner reflector	47
Figure 4.8: Ice surface roughness measured from a 2 m bar to the ice surface	51
Figure 5.1: ERS-2 uncorrected SAR.....	54
Figure 5.2: Radarsat uncorrected SAR.....	55

Figure 5.3: The portion of Taylor Valley that was imaged by ERS-2	57
Figure 5.4: Surface characteristics along the transect on Commonwealth Glacier	59
Figure 5.5: Photographs of Commonwealth and Howard Glaciers	60
Figure 5.6: Cryoconite hole.....	61
Figure 5.7: Snow depths along the transect on Commonwealth Glacier	63
Figure 5.8: Sky and Water I	63
Figure 5.9: Snow stakes, radar reflectors, transect route, and sample sites on Commonwealth Glacier	63
Figure 5.10: Snow layers graph.....	64
Figure 5.11: Averaged snow depths along the transect on Howard Glacier .	66
Figure 6.1: Effect of a SAR beam scattering off specular surfaces of different incidence angles.....	70
Figure 6.2: Intermediate Terrcorr images of Commonwealth Glacier.....	73
Figure 6.3: Auto and un-corrected ERS-2 SAR of Commonwealth Glacier	74
Figure 6.4: Terrain and un-terrain corrected Radarsat ScanSAR.....	76
Figure 6.5: ERS-2 terrain corrected SAR.....	77
Figure 6.6: Radarsat terrain corrected SAR	79
Figure 6.7: Auto- and manual-correlation terrain correction of Commonwealth Glacier and surrounding area.....	82
Figure 6.8: ERS-2 SAR of Commonwealth Glacier and surrounding area ..	86
Figure 6.9: Slope and elevations (from DEM) of Commonwealth Glacier ..	87
Figure 6.10: ERS-2 SAR of Commonwealth Glacier with elevation contours	88
Figure 6.11: Manually-correlated and uncorrected ERS-2 SAR of	

Commonwealth Glacier.....	90
Figure 6.12: Terrain and un-corrected Radarsat ScanSAR of Howard Glacier	94
Figure 6.13: SAR local incidence angles	95
Figure 7.1: Corrected SAR brightness and surface measurements along the transect.....	98
Figure 7.2: SAR image brightness relative to surface elevation	99
Figure 7.3: Commonwealth Glacier ERS-2 SAR 1/15/1999 snow measurement locations	99
Figure 7.4: ERS-2 brightness to snow depth graph.....	100
Figure 7.5: Commonwealth Glacier ERS-2 SAR snowline classification maps	102
Figure 7.6: Comparison of Commonwealth Glacier	105
Figure 7.7: Detail of snowline on Commonwealth Glacier ERS-2 SAR.....	108
Figure 7.8: Enhanced volume backscatter.....	111
Figure 7.9: Commonwealth Glacier snow stratigraphy	112
Figure 7.10: Reflections and primary refractions of the SAR beam at stake 12.....	115
Figure 7.11: Uncorrected brightness comparison (along the transect) between Radarsat and ERS-2	118
Figure 7.12: Terrain corrected SAR image transect locations	119
Figure 7.13: Comparison of corrected and uncorrected brightness values along the transect.....	120
Figure 7.14: Corrected brightness comparison (along the transect) between Radarsat and ERS-2	122

Figure 7.15: Howard Glacier snow layers graph.....	125
Figure 7.16: Landsat and Radarsat comparison of Howard Glacier snowline	127
Figure 7.17: Six SAR views of Commonwealth Glacier	129
Figure 7.18: The terminus of Canada Glacier as represented by six SAR images.....	131
Figure 7.19: Aerial photo of Canada Glacier taken November 1993.....	132
Figure 7.20: Images of Taylor Glacier	134
Figure 7.21: Ripples on the upper Taylor Glacier as represented by four SAR images and one Landsat.....	135
Figure 7.22: Lower Taylor Glacier as represented by five SAR images	136
Figure 7.23: Radarsat ScanSAR image transect of the centerline of Taylor Glacier	137
Figure 7.24: Comparison of backscatter of lake surfaces by season.....	139

CHAPTER I

INTRODUCTION

The possibility of global climate change has caught the attention of both the scientific community and the public. Increasing levels of atmospheric carbon dioxide, affected by human activity, may be causing increasing global temperatures (Crowley, 2000; Watson, 1996). The phenomenon of the El Niño-Southern Oscillation (ENSO), the development of a cap of warm ocean water along the coast of Peru that blocks the upwelling of cold water (Sarachik, 1997), and how it affects weather around the planet have become a common concern in our society. Global Circulation Models (GCMs) have been developed to predict climate change, and the global warming trend is predicted to continue (Crowley, 2000; Watson, 1996). This temperature increase is believed to be melting glaciers and contributing to the rise in sea levels (O'Farrell et al., 1997; Oerlemans and Wegener, 1989).

Antarctica plays a critical role in global climate variation. Because of its large size and low temperatures, Antarctica is one of the largest energy sinks on earth (Tzeng et al., 1993). Ocean surface currents and subsiding flows circulate warmer water to Antarctica and cold water towards the equator (*ibid*). Latitudinal temperature gradients control meridional atmospheric flow that moves atmospheric heat and moisture to the pole (*ibid*).

To predict changes in the Antarctic Ice Sheet, GCMs are coupled with ice sheet models (Marsiat, 1996; Verbitsky and Saltzman, 1995). Because the response time between snowfall and glacier advance or retreat movement is so long, ice sheets will rarely obtain equilibrium (Fastook and Prentice, 1994). A warming Antarctica, however, may not contribute water to the oceans via melting, because it may also increase snow precipitation due to the atmosphere's increased ability to carry moisture to the continent (Budd et al., 1994; Fastook and Prentice, 1994; Krinner and Genthon, 1997; O'Farrell et al., 1997).

A vital parameter in ice sheet models is mass balance (Budd et al., 1994; Fastook and Prentice, 1994; Marsait, 1996; Van De Wal, 1996). Mass balance is the difference between mass gain (snowfall) and mass loss (ablation) over the whole ice body (Patterson, 1994). Because the atmosphere drives most of these processes, mass balance is a proxy measure of the climate (*ibid*). Changes in glacier and ice sheet mass balance are one of the most important components for predicting global sea level (Ohmura et al., 1996; Oerlemans, 1989; Oerlemans, 1992).

Mass balance changes are measured over a single year. These year-to-year changes in mass affect the position of the terminus after some lag time depending on the thickness, length, and temperature of the glacier (Patterson, 1994). The changes in advance or retreat of glaciers and ice sheets are responses to multiple past mass changes that occurred over different time scales (*ibid*).

The equilibrium line altitude (ELA) of a glacier is the dividing line between the region of yearly net mass accumulation (the accumulation zone)

and the region of yearly net mass loss (the ablation zone): at this line, the mass balance is zero, or at equilibrium (Patterson, 1994). The ELA moves up or down due to changes in meteorology (snowfall, latent and sensible heat). The ELA responds only to meteorological variations whereas terminus variations are a result of meteorology and ice dynamics. Thus, the ELA is an important variable in climate studies, energy balance studies, and runoff modeling. For temperate glaciers the transient snowline may be different than the ELA, but on Antarctic (polar) glaciers the snow line *is* the ELA (*ibid*). This is because of melt on a polar glacier. The sub-freezing, dry atmosphere sublimates the snow in place.

One of the most attractive techniques for tracking the ELA in Antarctica is satellite synthetic aperture radar (SAR). SAR has several benefits: it covers broad areas; it has a long wavelength allowing it to image through clouds; and it is self-illuminating allowing it to image in darkness. Therefore SAR has an all-weather, day/night capability, which is an attractive feature for imaging Antarctica because of the frequently cloudy skies near the continental margins and darkness throughout the austral winter. Compared to ground measurements, SAR is an inexpensive approach to monitoring the ELA position.

Although the US Navy has used radar (**RA**dio **D**etection and **R**anging) since 1934 for object detection (Ulaby et al., 1981), specific questions as to exactly how it interacts with different surfaces are now in the forefront of research. Various researchers have noted penetration of radar energy into snow surfaces (Bindschadler, 1998; Bindschadler et al., 1987; Fahnestock et al., 1993; Jezek, 1993a; Partington, 1998; Rott et al., 1993; Rott and Davis, 1993).

The penetration depth of SAR in dry snow was theoretically estimated to be 20 m (Ulaby et al., 1981); however, field studies comparing the SAR image with measured penetration are lacking. Because of penetration of radar energy into dry snow, the thinner snow margins are not detected, causing underestimation of the full extent of snow cover and could cause up-slope displacement of the ELA.

This thesis demonstrates a methodology for estimating the location of the ELA using SAR. This work has two important applications. First, defining the ELA on the Antarctic Ice Sheet will be more easily investigated on a large scale. Second, the McMurdo Long Term Ecological Research (LTER) project in Taylor Valley, Antarctica, will benefit by using SAR to monitor the ELA on more glaciers. The McMurdo LTER is part of a long-range collaborative investigation focusing on ecological processes. The entire LTER consists of 21 sites, one of which is in the McMurdo Dry Valleys (including Taylor, Wright and Victoria Valleys) (Figure 1.1) (Harris, 1998; Moorhead and Priscu, 1998). Currently five glaciers in the valley are monitored by field measurements, but with SAR a more complete picture of the variation in the ELA will be acquired. Since the valley's microbial communities depend on the influx of liquid water, understanding how the climate could change in this valley and estimating the corresponding levels of biotic activity will allow researchers to further understand how life exists in one of the most extreme environments on earth.

Additional applications of this research may be applied to the Martian Polar Ice Caps. Earth-bound radar imagery of the Martian Polar Ice Caps has shown the cap to be very heterogeneous (i.e. very fractured and lumpy) and

thus very reflective (Muhleman et al., 1995). A Magellan-type mission (which mapped Venus in 1990-1994 using a SAR) to Mars may resolve similar glacial zones discussed in this thesis.

CHAPTER II

SITE DESCRIPTION

To develop a method of using SAR to track the ELA, a study area must be selected. Four factors are required for a good study site. First, to examine dry snow conditions, to quantify SAR penetration, the glaciers must be polar glaciers. Second, a variety of glaciers must be in a close proximity to compare different glaciological features and topographic characteristics relative to the SAR position. Third, access to the study site must be available to support the investigation. Fourth, the surface travel over the glaciers must be accessible by foot; too many crevasses and icefalls would preclude surface travel and therefore this experiment. The glaciers in Taylor Valley, Antarctica meets all the requirements for this research.

Taylor Valley is about 35 km long and 12 km wide, extending from McMurdo Sound to the east and to the Taylor Glacier (an outlet glacier of the East Antarctic Ice Sheet) in the west (Figure 1.1). The Asgard Range bounds the Taylor Valley to the north and the Kurki Hills to the south, both rising 2,000 m.

The mean annual air temperature of Taylor Valley is -18°C , with summer (December and January) temperatures reaching 0°C and winter temperatures dropping as low as -40°C (Clow et al., 1988). Average monthly wind speeds range

from 2-4 m s⁻¹ in Taylor Valley. In 1995 the mean annual wind speeds ranged from 2.7-3.9 m s⁻¹ with peak averages 11-15 m s⁻¹ (*ibid*). Testifying to the high winds of the valley, ventifacts are found throughout the valley (Fountain et al., 1998).

Precipitation in the valleys is less than 10 cm water equivalent yr⁻¹; however it is mostly lost to sublimation and does not accumulate (Keys, 1980).

The winter climate is strongly influenced by episodic katabatic winds. The katabatic winds begin on the Polar Plateau with intense radiative cooling of the ground and subsequent downslope movement of cold near-surface air under the influence of gravity (Parish and Bromwich, 1987). As the air descends, it heats adiabatically and its relative humidity drops. These winds exhibit speeds up to 20 m s⁻¹ and persist for an average of six hours (Clow et al., 1988). At Lake Hoare, adjacent to Canada Glacier, katabatic winds greater than 5 m s⁻¹ occur 33% of the time during the winter; air temperatures increase 20-30° C; to approximately -12° C, and the relative humidity drops by 20-30% (*ibid*).

Meltwater streams originate from all glaciers in the valleys indicating surface melt during the austral summer (Fountain et al., 1998). Stream flow is dependent on melting ice and is determined, in part, by air temperature (Conovitz et al., 1998). This melt water is the primary limiting condition for life in the valley: during the short summer, the glacial meltwater transports water and the nutrients that the biologic community depends on (Conovitz et al., 1998; Moorhead and Priscu, 1998).

Snow has a very high albedo (the reflectivity of a surface) from 0.7-0.9 reflecting most of solar radiation, whereas ice has a much lower albedo, 0.2-0.4, absorbing more energy and melting more readily (Patterson, 1994). Because of this,

even a thin snow cover greatly influences glacial melt. A summer snowstorm covering the glacier ice stops almost all melt for weeks (Fountain et al., 1998).

Many glaciers in Taylor Valley have steep termini that form near-vertical cliffs (Fountain et al., 1998). Most of the glaciers are small ($3\text{-}5\text{ km}^2$) alpine glaciers that descend from altitudes of about 1000 m to the valley floor about 50 m above sea level. Net snow accumulation is only 0.1 m water equivalent (weq) averaged over the accumulation zone. Similarly the annual mass loss in the ablation zone is on the order of 0.1 m weq. The glaciers vary in roughness from smooth (roughness less than 1 cm) to extremely rough (10 m or more). The movements of the glaciers are slow, roughly 4 m yr^{-1} (Fountain, unpublished). The equilibrium line altitude (ELA) of the glaciers rises from about 200 m near McMurdo Sound to about 900 m at the western end of the valley (Fountain et al., 1999). The rise in the ELA results from a strong climatic gradient in the valley: snowfall decreases and windiness increases away from the coast. Since glaciological observations began in Taylor Valley, the snow in the accumulation zones has been dry, although thin ice layers in the snow indicates slight melting (Fountain et al., 1998). Melting is mostly limited to the exposed ice region near the lower margin of the glaciers (*ibid*). The mass changes of Taylor Valley glaciers are small: 10-30 cm of snow collecting in the accumulation zone and 6-15 cm of ice lost in the ablation zone (Fountain et al., 1999). The primary components of ablation in Taylor Valley are sublimation, evaporation, and melting. Surface energy calculations on Canada Glacier indicate that evaporation and sublimation accounts for up to 70-90% of the summer ablation, and melting 15-30% (calving accounts for 1-3%) (Lewis et al., 1995).

McMurdo Dry Valleys Long Term Ecological Research (LTER).

The National Science Foundation funded, McMurdo Dry Valleys Long Term Ecological Research (MCM-LTER) project, has studied the Taylor Valley ecosystem since 1993 (Fountain et al., 1999; Harris, 1998). The project is one of twenty-one sites representing diverse and unique ecosystems, ranging from the dry valleys in Antarctica, to a tropical rainforest in Puerto Rico (*ibid.*). Taylor Valley is relatively pristine, with a relatively sparse ecosystem (dominated by microbiota) with short food chains, and lacks all high plant and animal life (Moorhead and Priscu, 1998). The valley presents an opportunity for study of basic ecological processes without complications of higher organisms. The environment is very sensitive to physical changes and offers an opportunity for measuring response of the ecosystem to subtle climatic variation (Harris, 1998; Moorhead and Priscu, 1998). The life that exists in this polar desert is approaching the environmental limits of life on Earth (Moorhead and Priscu, 1998). It is an "end member" in the spectrum of environments studied by the LTER network (*ibid.*).

The glaciological research of the MCM-LTER project helps to define the controls on water flow variation in the valley that animates the biotic community. The project has produced a rich body of data that are useful for interpreting SAR data. The glaciological investigations in the valleys include mass balance measurements, surface energy balance calculations on the Canada Glacier, ice velocity measurements, and ice depth. These studies are focused on four glaciers: Canada, Commonwealth, Howard, and Taylor glaciers. Glacier mass balance data are

collected twice a year, once in the spring (November) and once in late summer (January), to provide winter and summer mass changes (Fountain et al., 1998). The measurements are based on a 130-stake network spread across the four glaciers. The main questions being answered by these measurements are (1) whether the glaciers are in balance with the current climate, (2) how surface slope and aspect affect ablation, and (3) methods for predicting glacial melt. The measurements at each stake include surface height change, snow density, and stratigraphic characteristics of the snow (including snow crystal size and form). From surface height change and density, mass change is calculated.

Nine meteorological stations are located in the dry valleys with eight in Taylor Valley (Doran et al., 1995). All stations measure air temperature, humidity, ice (or soil) temperature, wind speed/direction, snowfall, and incoming and outgoing solar flux. Stations located on Glaciers also measure longwave radiation and barometric pressure is measured at two stations (Lake Hoare and Canada Glacier). The sensors are queried every 30 seconds and store data every 15 minutes.

CHAPTER III

SYNTHETIC APERTURE RADAR THEORY

Among the remote sensing tools now available, radar is unique. It is an "active" sensor and emits its own beam of energy, which reflects off the earth and returns to the sensor. Thus radar collects data independent of solar illumination and because of its comparatively long wavelength, weather has minimal affect (Ulaby et al., 1981). Within the electromagnetic spectrum (Figure 3.1) radar is in the microwave range of ~ 1 cm to ~ 1 m.

When radar was first being developed by the military, the microwave spectrum was divided into bands (Table 3.1), with illogical designators to help conceal their applications (Campbell, 1996). Common terminology uses "microwave" as passive and "radar" is usually reserved for active microwave. Radar also refers to the sensor itself including: the transmitter, the antenna, the receiver, and the data handling equipment. Radar has been used since the early 1960s to image the surface (and near surface) of sea ice and glaciers (Hall, 1998). Airborne radars frequently use the L, C, K, and X-bands, satellite radars have used the C and L-band frequencies (Campbell, 1996). These

longer wavelengths are used in satellites because they are least sensitive to atmospheric attenuation by clouds, rain, and snow.

Table 3.1: Radar Frequency Designations.

Band	Wavelength (cm)
Ka	0.75-1.18
K	1.18-1.67
Ku	1.67-2.40
X	2.40-3.75
C	3.75-7.50
S	7.50-15.0
L	15.0-30.0
UHF	30.0-100.0
P	77.0-107.0

Because the microwave range is well removed from the visible spectrum, it interacts quite differently with surfaces compared to visible light. Although radar images look very similar to a black and white aerial photograph, they defy many of the intuitive interpretation we unconsciously apply to visible light images. The scattering properties of surfaces in the microwave range are affected by the electrical properties of the surface, its orientation, and its porosity. These factors will be discussed later. The short radar wavelengths yield higher resolutions but lower penetration of the atmosphere due to moisture. The long wavelengths readily penetrate atmospheric moisture, but yield lower resolutions and higher surface penetration (Campbell, 1996).

Synthetic Aperture Radar Principles.

Side looking, fixed-antenna-length airborne radar was developed by the military to image areas behind enemy lines while flying over safe territory

(Figure 3.2) (Avery and Berlin, 1992). For fixed-length antennas, resolution depends on antenna length and decreases with increasing distance from platform to target (Avery and Berlin, 1992). Thus satellite application of radar was largely precluded. To overcome the limitation of antenna size “Synthetic Aperture Radar” (SAR) was developed (Ulaby et al., 1981). In the same way that a wide photographic aperture allows more light to reach the film in a camera, a long antenna receives more radar waves. Antenna *length* is analogous to a camera aperture. A larger antenna (aperture) is synthetically produced by using the forward motion of the platform to carry a relatively small antenna to a new location (Figure 3.3) (Lillesand and Kiefer, 1994). Because of the beam shape, some areas are imaged multiple times (Figure 3.2); the successive portions are treated electronically as though each one were an individual element of the same antenna (Avery and Berlin, 1992). The concatenation of the signal modulations of the multiple returns for each target is what increases the resolution in a SAR image (Raney, 1998). For example, the European Remote Sensing (ERS)-2 SAR synthesizes the equivalent of a 4 kilometer-long antenna (Alaska SAR Facility website, 2000).

Radar measures the round-trip travel time of the emitted and reflected microwaves (i.e. time domain) as well as the signal strength (Avery and Berlin, 1992). Imaging radars transmit about 1500 pulses per second, each pulse lasting for 10-50 microseconds (Ulaby et al., 1981). Once the pulse reaches the Earth's surface, it is scattered and some of the scattered energy is directed back towards the antenna. The signal is converted to digital format and then either temporarily stored using the satellite's on-board tape or immediately transmitted to a ground receiving station (Jet

Propulsion Lab website, 2000).

On current satellite platforms, the radar beam is like-polarized. It is emitted vertically (V) or horizontally (H) and only the same polarization signals are accepted back into the SAR (called VV or HH) (Campbell, 1996). The space shuttle and various aircraft SARs can operate in multi-polarizations. They may be transmitting and receiving like *and/or* unlike polarizations.

Object range is calculated by using the time delay between emitted and reflected radar pulses (Avery and Berlin, 1992; Ulaby et al., 1981). Because the signal data is sorted by time delay, radars image to the side, rather than downward to remove ambiguities between the right or left return signals. Each pulse is coded so that the SAR knows *which* pulse is coming back: the first signal returning is from the near-range and the later signals are from progressively longer ranges until the last bit of information from the far-range is received (Avery and Berlin, 1992). The pulse length (how long the radar is emitting the pulse times the speed of light) determines range resolution (shorter the pulse, the higher the resolution) (Figure 3.4) (Campbell, 1996).

Azimuth, relative to the satellite, is calculated by measuring the doppler shift of the returning pulse relative to emitted pulse (Avery and Berlin, 1992). Doppler shift in the electromagnetic spectrum is analogous to the doppler shift of a whistle on a passing train: as it approaches, the whistle's tone is doppler shifted negatively (compressing incident wavelengths and producing a higher-pitched whistle), and as it moves away, it is doppler shifted positively (producing longer apparent wavelengths, and a lower-pitched whistle). In the same manner SAR measures the doppler shift, except the

platform is moving and the target is stationary. The area of the earth that is illuminated by the SAR sensor is a series of teardrop-shaped footprints. Surface features enter the illumination area, and in each successive pulse, move through it and exit with the features further from the sensor being illuminated more times (*ibid*). Using multi-look signal processing, the signal modulations (signatures of the returns for a specific target) are matched at each point in the SAR scene (Raney, 1998). This signal processing, called SAR processing, is done on ground-based computer systems. Since the satellite is moving relative to the Earth, this processing requires very precise data on the relative motion between the imaging platform and the target (Avery and Berlin, 1992). The achievable azimuth resolution of a SAR is approximately equal to one-half the length of the actual (real) antenna and does not depend on platform altitude (distance) (Raney, 1998; Ulaby et al., 1981).

The final SAR image is composed of many small squares. These squares, or pixels (*picture elements*), represent the averaged intensity of radar signal returning to the sensor, or backscatter, for an area on the ground. SAR image pixel size is controlled by the length of the actual (real) antenna (controlling azimuth resolution), radar pulse which determines range resolution, signal coherence which controls signal quality or “noise”, and the accuracy that the processor is able to match the signal modulations (Raney, 1998).

Radar Distortions and Terrain Corrections.

Initially, SAR distance is in slant range, or the inclined plane from the platform to the earth's surface (Figure 3.5). Maps, however, are made using plan-view ground distances. Using slant-to-ground range correction software, the satellite data are projected into ground distance. Each pixel represents a specific area on the ground and is re-projected into a standard grid (UTM, polar stereographic, etc). The pixels are then "geocoded" with evenly spaced in longitude and each row is assigned a specific latitude. Topographic distortions do occur because the radar data are originally collected in a time domain. They are foreshortening, layover, and shadowing.

Foreshortening occurs in mountainous terrain where the top of a mountain is close to the same distance from the platform as the bottom (Figure 3.6). Radar reflections returning from the base of the mountain arrive at very nearly the same time as those returning from the peak. The uncorrected image looks like the mountain's slope is much steeper than in reality. Layover is an extreme form of foreshortening and occurs when returns from a steep mountaintop arrives *before* its base (Figure 3.6). It is impossible to decorrelate the reflections to determine which is from the base or the top of the mountain and the image in this region has no recognizable features. Shadowing occurs in mountainous regions in the same way the sunlight casts shadows. Where the radar cannot illuminate some of the ground because a mountain blocks the radar beam, no returns are collected and become "no data" areas (Figure 3.6). These distortions are related to look angle from the platform

and surface topography (Lillesand and Kiefer, 1994). Look angle can vary not only from orbit to orbit, but also varies within a scene because the near-range has a smaller look angle than the far-range (*ibid*). For this reason, shadowing increases towards the far-range and foreshortening decreases (*ibid*). These terrain distortions (foreshortening, layover, and shadowing) can be minimized by employing known elevation data of the imaged area. This *terrain correction* will be discussed in detail in Chapter VI.

Radar Backscatter.

Bright pixels in a SAR image represent areas where a comparatively large fraction of the radar energy was reflected back, and dark pixels signify those areas from which little energy was returned. There are four types of radar scattering: diffuse, specular, volume and corner reflection (Figure 3.7). Diffuse scattering sends the incident energy in all directions (like light reflecting off a sheet of white paper). Specular reflection directs the incident radiation in a single direction (like light reflecting off a mirror). Volume reflection scatters the incident energy in all directions (like the dark, rich blue seen in a deep, clear lake, is a volume reflection of the visible blue light from varying depths in the lake). The fourth type of scattering is corner reflection, which occurs when a beam specularly reflects two or more times, reversing the energy directly back towards the source. This type of reflection is used in land surveying methods for laser range finding. In SAR images, it commonly occurs in urban areas where buildings provide an abundance of highly reflective

structures presenting right angles to incident radar (*ibid*). Naturally occurring corner reflectors include cliffs, fault lines, and tree trunks.

A variety of factors influence backscatter strength including: satellite ground-track, incidence angle, radar polarization, surface roughness, and the dielectric properties of the surface (Campbell, 1996). A satellite ground-track (the path on the earth directly below the satellite) that is parallel to a linear feature (e.g., a fault line, row of crops, or ocean waves) will produce a higher backscatter than a perpendicular ground-track. Similarly, variations in the incidence angle of the radar beam with respect to the earth's surface, low incidence angles yield a high backscatter; high incidence angles yield low backscatter (causing more specular reflection). Because of this, slopes facing the radar beam will have a higher backscatter than slopes facing away. As mentioned before discussing satellite look angle, on a geoid the far range will have a higher incidence angle causing more specular reflection than the near range which will have lower incidence angles.

Backscatter will also vary depending on the use of different polarization. VV polarization is most sensitive to vertically oriented features such as plant stalks and tree trunks (Avery and Berlin, 1992). HH polarization is more sensitive to horizontal oriented surfaces like roads, riverbeds, and faults.

Roughness relative to the radar wave is determined by three factors: size of the surface variation, wavelength of the radar signal, and incidence angle of the radar beam (Avery and Berlin, 1992). Objects that are as large as or larger than the wavelength of the radar beam reflect the radar energy and thus are "rough," appearing

bright. Objects smaller than the wavelength do not reflect much energy and appear dark (smooth) (Campbell, 1996). Roughness varies with wavelength: short-wavelength radar can discern smaller variations of roughness than long-wavelength radar. Incidence angle becomes less important in rough surfaces because the surface will be diffusely reflected (Figure 3.7) (Campbell, 1996).

Radar reflectivity also varies with an electrical property of the reflecting material called the *complex permittivity* ϵ_c , often called the *dielectric constant*. It is the measure of a medium's response to the presence of an electric field (Raney, 1998). Specifically it is:

$$\epsilon_c = \epsilon' + i\epsilon'' \quad (3-1)$$

where the first term on the right hand side, ϵ' , is the dielectric constant of the material, and the second term is the imaginary part, where i is the square root of -1 , and ϵ'' is the “lossy” part of the dielectric constant. The dielectric constant of the material (ϵ') is an absolute measure of the medium's response to an electrical field. When an electric field is applied to the medium, the molecules realign to the lowest energy state to fit their polarity to the electric field. Because the molecules are in a crystalline structure, they cannot completely align to the applied field. Different substances align with varying completeness and the success of the alignment is what the dielectric constant describes. The lossy part (or dielectric loss factor) of the dielectric constant (ϵ'') describes the lag time between the application of the electric field and response of the molecules in the medium. This lossy part is associated with the absorption of the electromagnetic radiation.

As the dielectric of a material increases, the reflectivity also increases (Table 3.2). Liquid water, because of its high dielectric, has a pronounced effect on a material's dielectric constant (Avery and Berlin, 1992). For example, as a dry porous medium (soil, sand, snow) increases wetness; its dielectric constant increases, causing its reflectivity to radar waves to increase. Incident radar waves specular reflect away from the platform resulting in a dark pixel. Conversely, a dry medium, having a low dielectric, allows the radar wave to penetrate and volume reflect, producing a much brighter return at the sensor (Figure 3.7d).

Table 3.2: Dielectric values of some materials.

Material	Dielectric constant of the material (ϵ')
Sea water	81 (Raney, 1998).
Fresh water	81 (<i>ibid</i>).
Wet earth	10-35 (Ulaby et al., 1981).
Dry earth	3-5 (<i>ibid</i>).
Dry snow	1-3 (<i>ibid</i>).

Radar Penetration.

Penetration of SAR energy into dry granular materials (e.g. sand or dry snow) has been documented for over a decade (Short and Blair, 1986). Radar penetrated 2 m of dry alluvium revealing buried igneous dikes in the Mojave Desert (Blom et al., 1984). Radar also penetrated “up to several meters” through dry sand in the Selma Sand Sheet in Sudan, exposing paleodrainage systems and buried geologic structures (Short and Blair, 1986; McCauley et al., 1982). For a single wavelength, the degree of penetration is related to the dielectric constant of the material (lower the constant, the

higher the penetration) and its density (lower the density, the deeper the penetration). Longer radar wavelengths are able to penetrate deeper than shorter wavelengths (Shi and Dozier, 1993).

SAR Platforms.

Orbiting SAR sensors include Shuttle Imaging Radar–C/X (SIR-C/X), Radarsat satellite (Canadian Space Agency), and European Remote Sensing –2 satellite (ERS-2, European Space Agency). SIR-C/X first operated 1994, is occasionally carried aboard the space shuttle and consists of three individual antennas: L-band (23.5 cm), C-band (5.8 cm), and X-band (3 cm). The L-band and C-band antennas can measure both horizontal and vertical polarizations. Because of the different polarizations, SIR-C/X aids in understanding the interaction of microwaves with surfaces in more ways than a single polarization SAR can.

Radarsat carries a single frequency C-band antenna, with a unique ability to steer its radar beam over a 500-kilometer range (Table 3.3) (Jezek et al., 1993). A wide variety of beam selections are available: the swath width can be adjusted from 45 to 500 kilometers, with resolutions from 8 to 100 meters, and incidence angles from 10° to 60°. Repeat coverage is available daily in the high latitudes, and in equatorial latitudes every six days (Canadian Space Agency website, 2000). The orbital period is 100.7 minutes and the polarization is HH. The European Remote Sensing satellite (ERS-2), launched in 1995, carries a C-band SAR, with VV

polarization (Table 3.3). It images a 100 km swath of the Earth's surface. Repeat coverage is available every three days, and has a resolution of 25 m.

Table 3.3. Radar instrument specifications for Radarsat, and ERS-2 (Campbell, 1996).

	Radarsat	ERS-2
Frequency/Band	5.3 GHz/C-band	5.3 GHz/C-band
Wavelength	5.66 cm	5.66 cm
Polarization	HH	VV
Accessible swath	50-500 km	100 km
Look angle(s)	20-59°	23°
Resolution	8-100 m	25 m
Launch date	1995	1995

Application of SAR to Snow and Ice.

Radar scattering from snow is dependent on its dielectric constant, which varies due to changes in water content. The snow's dielectric value influences whether the beam will reflect and/or penetrate the snowpack (Avery and Berlin, 1992). The imaginary part of the complex permittivity (ϵ'') is extremely sensitive to liquid water in the snow mixture, the greatest change of ϵ'' occurs over wetnesses of only 0-0.5%. So only a small amount of liquid water in the snowpack will begin to absorb the radar and lessen volume scattering. The radar penetrates dry snow and the energy scatters from the dielectric discontinuity between ice crystals and air (Hall, 1998; Ulaby et al., 1981). The scattering occurs at varying depths of the snow pack, sending the signal in all directions, yielding a bright return at the sensor (Hall, 1998; Jezek et al., 1993; Mätzler, 1987). As the snow pack increases wetness the dielectric constant increases, penetration decreases and specular reflection increases (Avery and Berlin, 1992). Larger incidence angles also increase

penetration resulting in deeper near-range penetration and shallower penetration at the far-range (Shi and Dozier, 1993).

Penetration in dry snow-packs is dominated by surface roughness, scattering by snow grains, and internal density contrasts (Hall, 1998; Rott and Mätzler, 1987; Shi and Dozier, 1993). As snow ages, grain size increases (Patterson, 1994), and changes the scattering properties, increasing reflectivity. Compared to new snow, firm (snow that survived the ablation season ~1 year old), with larger grain structure, yields a brighter reflection (Hall, 1998). Sublimation at depth creates large ice crystals in the shape of prisms, pyramids, or hollow hexagonal cups called depth hoar (Patterson, 1994). Depth hoar is highly porous and its density is low (100 to 300 kg m⁻³) with its large grain structure yields a bright SAR reflection.

At C-band frequencies, scattering losses in homogeneous dry snow are small and penetration depth can be calculated solely on the effective dielectric constant (ϵ) (Ahammer and Denoth, 1994; Rott et al., 1993; Rott and Davis, 1993). The value of ϵ can be calculated by volumetrically weighted average of the dielectric constants of the bulk material, air and ice (Rott et al., 1993; Rott and Davis, 1993). Using these relations Rott and Mätzler (1987) calculated penetration depths of 21.7 m at a wavelength of 4.9 cm (C-band) and 8.1 m at a wavelength of 3.1 cm (X-band) for dry, homogeneous, firm.

Table 3.4. Snow dielectric properties and penetration depth for wet, 6% liquid water, density 500 kg m⁻³ (Rott and Davis, 1993) and dry, 440 kg m⁻³ (Rott et al., 1993) snow. Dry snow figures in **bold**.

Band	X	C	C	L
Frequency (GHz)	10.3	5.3	5.2	1.25
ϵ'		2.95	1.87	3.23
ϵ''	.00021	0.571	0.0001	0.170
Depth of estimated penetration (m)	8.1	0.027	21.7	0.404

Equation 3-1 contains two parts for determining the dielectric or complex permittivity. The first term ϵ' , or dielectric constant of the material, relates to the snow. The second term ϵ'' , or the imaginary part, relates to the amount of moisture of the snow. The absorption of the electromagnetic field by moisture in the snow is described by this second term. The dielectric constant (ϵ) for dry snow, is calculated by adding the real part (ϵ') and the imaginary part (ϵ'') of for the frequency (f) using Mätzler's (1987) mixing formula:

$$\epsilon = \epsilon' + i\epsilon'' = \epsilon_d + \frac{23W}{1 - i\left(\frac{f}{f_0}\right)} \quad (3-2)$$

where ϵ_d is the dielectric constant for dry snow, W is the liquid water content (expressed as a volume fraction), and f_0 is the relaxation frequency of wet snow. The penetration depth was obtained by:

$$d = \frac{\lambda_0 \sqrt{\epsilon'}}{2\pi\epsilon''} \quad (3-3)$$

where λ_0 is wavelength of the SAR, and ϵ' and ϵ'' are obtained from the above formula

(Rott and Davis, 1993).

Penetration depth for wet snow with water content of 2-4% is typically one wavelength (Rott and Mätzler, 1987). Any surface melt on a snow surface results in almost complete specular reflection and lower backscattering values (Jezek et al., 1993; Rott and Mätzler, 1987). Therefore SAR return in wet snow is more dependent on the surface roughness; a smooth melting snow surface yields a dark backscatter (Bindschadler et al., 1987; Bindschadler, 1998; Fahnestock et al., 1993; Forster et al., 1991; Jezek et al., 1993) and a rough wet snow surface is brighter (Smith et al., 1997).

Ice, whether dry or wet, is uniform in its backscatter, specularly reflecting the radar energy away from the sensor (Bindschadler et al., 1987; Bindschadler, 1998; Fahnestock et al., 1993; Forster et al., 1996; Jezek et al., 1993; Partington, 1998; Smith et al., 1997). Only if the surface is very rough, can the beam reflect and yield a bright return (Bindschadler et al., 1987; Bindschadler, 1998; Fahnestock et al., 1993; Forster et al., 1991; Partington, 1998).

Radar Zones.

Carl S. Benson developed a theory of glacier zones during his traverses across the Greenland Ice Sheet 1952-1955 (Benson, 1962). At about the same time Fritz Müller was also developing a similar theory (Müller, 1962). Because of the parallel development, the glacier zone model is known as the “Benson-Müller” facies model. The model treats glaciers and ice sheets as a monomineralic formation, primarily

metamorphic, but with a sedimentary veneer of snow and firn. With this hypothetical model, the lithological term "facies" is used to differentiate zones on ice sheets and glaciers.

The four Benson-Müller facies are: ablation, soaked, percolation, and dry-snow (Figure 3.8). The ablation facies begins at the terminus of the glacier and ascends to the firn line approximately equal to the ELA. The firn line is the highest elevation to which the annual snow cover recedes at the end of the summer. It is an ice surface and is in temperate zones wet in the summer. The soaked facies is firn, which at the end of the melting season is wet throughout. The facie begins at the firn line and rise up glacier to the saturation line. The saturation line is the highest altitude that the 0° isotherm penetrates to the snow surface of the previous summer. The percolation facies is characterized by melting, and percolation of the water into the snow-pack, without becoming wet throughout. The melted water freezes inside the snow-pack forming lenses (lens-shaped inclusions parallel to firn strata), glands (pipe-like vertical ice masses), and ice layers (flat-shaped sheets extending over large areas parallel to the firn strata). This facie begins at the saturation line and terminates at the dry-snow line. The dry-snow facies includes the entire glacier above the dry-snow line in which negligible melting occurs.

The backscatter of radar energy appears to correspond with locations of the Benson-Müller facies (Table 3.5) (Partington, 1998; Fahnestock et al., 1993). An additional radar zone beyond the Benson-Müller facies model is included and called the crevassed zone. Because of the bright returns from crevasses, highly crevassed areas

appear distinctly different.

Table 3.5: The five glacier radar zones. SAR brightness and surface characteristics are described relative to facie.

	Partington, 1998	Fahnestock et al., 1993	Smith et al., 1997
Location	Greenland & Mt. Wrangell, AK	Greenland	Stikine Icefields, B.C.
Type glacier	Polar/winter temperate	Polar	Temperate
Platform	ERS-1	ERS-1	ERS-1
Dry Snow	Very dark-grain size small (<5 mm).	Dark—small grain size and low density.	Bright return -cold winter snow, with no liquid water.
Percolation	Bright—ice pipes and lenses.	Bright—frozen pipes and lenses.	Dark-liquid water present (the 0° C isotherm).
Soaked	Dark.	Dark.	Bright—rough melting snow.
Ablation	Dark—specular reflection from super-imposed ice.	Dark—rough surface texture contributing to reflectance.	Dark—specular reflection from ice.
Crevasse		Bright—heavily crevasse ice providing linear reflectors.	

Consensus on radar signatures of each zone (except for “soaked”) is clear in polar glaciers. The temperate glacier in the Smith et al. (1997) study was conducted in winter when the upper part of the glacier was continuously below freezing. Smith’s dry snow zone melts in the summer and likely contains ice pipes, lenses, and ice layers; which would be more like the percolation zone of the polar glaciers. Smith’s percolation zone may more closely correspond to a soaked facie and the soaked zone of “rough melting snow” a local melt phenomena. If Smith’s zones are indeed displaced and a melt feature of “rough melting snow” is disregarded, the glacier zones theory appears to agree across the studies.

Clearly different melt processes on the glacier control much of the tonal

patterns in C-band radar (Jezek et al., 1993). The ELA corresponds roughly to the boundary between the dark bare ice zone and the brighter snow areas on the SAR image (Bindschadler et al., 1987; Bindschadler, 1998; Jezek et al., 1993; Partington, 1998; Smith et al., 1997). However, “dark” and “light” in a SAR image, are a perception of the 0-255 brightness scale (8-bit) by the viewer. It is difficult to be exact as to where “dark” and “light” lie in this scale because it varies from viewer and image, but in general “dark” refers to 0 to 170, and light is 200 to 255 (Smith et al., 1997).

CHAPTER IV

METHODOLOGY OF THE DATA COLLECTION

Objective.

To determine snowline position by comparing brightness variations in the two SAR images with measured surface features on Commonwealth and Howard Glaciers.

Experimental setup.

Radarsat ScanSAR, and ERS-2 satellites are utilized. The axes of both glaciers are generally parallel to the SAR look direction (Figure 4.1), while the optical depth of the radar beam will vary considerably between the two glaciers (Figure 4.2). It is because these two glaciers have very different incidence angles that they were chosen. The differences in backscatter between the two glaciers may reveal differences in mapping the position of the snowline.

Commonwealth Glacier. The main study site for the SAR investigation was Commonwealth Glacier (Figure 4.3). It is 52 km², faces to the southeast, ranges in elevation from 100-1000 m, and is 3 km from the ocean. Its gentle slope (5°) and broad width (~2 km) provides a large and relatively even surface to compare SAR brightness variations. The glacier slope faces toward the SAR beam and the optical

depth (parallel to the beam direction) of the snow is close to the actual depth (Figure 4.2). Commonwealth Glacier is dotted with a network of 26 stakes across the surface to measure mass balance (Figure 4.3). The ELA is approximately 350 m. In the ablation zone, roughness vary from 1 cm to 5 m with the larger roughness located near the glacier terminus (Fountain et al., 1998). Cryoconite holes are seemingly randomly dispersed (Wharton et al., 1985) and vary in width and depth from three to forty centimeters (Derek Mueller, personal communication). A cryoconite hole is a hole, sometimes with a re-frozen cap, containing a layer of wind-blown sediment and possibly (in the austral summer) water. They form by debris blowing to the glacier ice and subsequently absorbing more solar radiation and forming a depression. The depression collects more wind-blown debris, increasing the solar radiation absorption and (occasionally) producing water. Snow cover in the ablation zone ranges from traces to dune-like formations 4 to 35 cm high and covering areas from less than 1 m² to 20 m². In the accumulation zone, dry snow exists on the surface with thin ice layers and hoar snow at depth. The accumulation zone is generally quite smooth with roughness amplitudes typically less than a few centimeters and wavelength of 10 meters.

Howard Glacier. Howard Glacier (Figure 4.3) is the secondary study glacier, has similarly varying roughness and snow cover as Commonwealth Glacier, but it is steeper; 10° in the ablation area, 10-23° in the upper part of the glacier, and 16° overall

average. It is 8 km², faces to the north, ranges in elevation from 260-1000 m, and is 8 km from the ocean. The glacier faces away from the radar beam and the optical snow depth should be much larger than the actual depth (Figure 4.2). Seventeen mass balance stakes are found on the glacier (Figure 4.3). The ELA crosses the glacier at approximately 500 m.

The Radarsat image was acquired through Dorothy Hall at National Aeronautics and Space Administration (NASA). The ERS-2 image was ordered through the NASA Earth Observation System project science office via the Alaska SAR Facility (ASF). The image data were collected within range of the ground receiving station at McMurdo, Antarctica, to which the data was immediately transmitted. The data was then transferred to high-density digital tape and mailed to ASF at the University of Alaska in Fairbanks, Alaska, where the tapes were processed. SAR processing is complicated and computationally intensive, the following processing summary is a general review.

First the ASF reads the tape for the processing parameters such as: sensor name, wavelength, elevation/azimuth beam width, right or left side looking, nominal look angle, orbit data, chirp data, attitude, and number of samples per range line (Olmsted, 1993). Second, an array is calculated containing the best estimate of the spacecraft's location, orientation, and rotation rates. And finally, the ASF checks the doppler parameters, transmitted chirp (signal pulse), signal to noise ratio, and other parameters with default values to determine if they are within limits (Olmsted, 1993; Raney, 1998). The processing step geolocates the image (assigns geo-coordinates to the image corners and center), computes a slant to ground range conversion vector,

applies radiometric corrections, realigns data along azimuth, and interpolates the data to a ground-based grid. The image is then either sent to the user on a 9 mm tape in the mail or (as I received it) downloaded from the ASF via the Internet.

The Digital Elevation Model.

To terrain correct the images; a Digital Elevation Model (DEM) is used (details of this process are in Chapter 6). The US Geological Survey created the DEM of the Taylor Valley (Figure 4.4). The transformations that evolve to the DEM begin with 1970 aerial photography from which 1:50,000 scale Lambert Conformal Conic maps were produced. The USGS digitized the 50 meter contour lines from this map and created a triangulated irregular network (TIN) using a Geographic Information System (ArcInfo) (Cheryl Hallam, USGS, personal communication). They converted TIN to a DEM consisting of a square grid of points at 30 m intervals and shifted the datum from the Camp Area Datum of 1962 to World Geodetic System 1984.

Surface-Based Measurements.

The mass balance stakes on Commonwealth and Howard Glaciers are measured twice annually to assess the seasonal mass change. The measured variables are: layer thickness, snow density, crystal structure, and depth to last year snow surface. I measured additional surface conditions on a transect on each glacier to provide spatially detailed data to help explain brightness variations on the SAR image.

Commonwealth Glacier. The transect, 3.5 km long, began in the ice-covered

ablation area and extended to the snow covered region just above the snowline (Figure 4.3). To aid in identifying the transect on the SAR image, I placed two reflectors on the ice surface along the transect 2.5 km apart (the lower reflector at the start and the upper near the snowline). These reflectors were triangular trihedral corner reflectors, which are known location bright spots on the SAR image (Rott and Davis, 1993; Trevett, 1986). Reflectors were not placed on Howard Glacier because the effectiveness of the reflectors was unknown and resources for the corner reflectors were limited. To corner reflect; only two surfaces meeting at a 90° angle must be pointed toward a beam (Figure 4.5a). A triangular trihedral corner reflector presents three reflective surfaces arranged at 90-degree angles (Figure 4.5b) and requires less precision in pointing the reflector towards the radar beam (Fuller, 1970). To enhance identification, the reflectors were placed on glacial ice, which commonly appears dark on a SAR image. They crossed diagonally across the ablation area to capture an intervening bright region observed on previous SAR images. The transect then continues beyond the second reflector, into deep, dry snow: a bright SAR region where reflector identification would be difficult.

The reflectors need to be aimed at the location in the sky where the SAR platform will be when it illuminates the ground. The two critical directions from the ground, azimuth and inclination, were supplied by the ASF (Figure 4.6a). I determined the reflector inclination angle by hanging a plumb bob off the back apex, and adjusting the distance from the bottom point of the reflector to the plumb-bob by tilting the reflector. This distance, can be calculated by using the sine of the desired inclination (Figure 4.6b):

$$\sin(i) = x/h \quad (4-1)$$

$$x = h \sin(i) \quad (4-2)$$

where i is the inclination angle, h is the height of the reflector, and x is the measured distance from the plum bob to the bottom point of the reflector.

The Science Construction Unit of Antarctic Support Associates at McMurdo Station built the reflectors according to specifications supplied by the ASF. They consist of three triangular aluminum panels, backed with 1/2" plywood, and bolted to a steel frame (Figure 4.7). At the opening of the reflectors forms an equal lateral triangle with 8' per side; the minimum depth to the bottom point is 4'. The three corners anchor to 2' long steel poles drilled into the ice. The anchors are covered with snow to block the solar radiation from heating the metal and melting them out of the ice. The bottom point of the reflector is set in a corner-shaped hole in a wooden beam, which is chiseled into the ice to prevent it from shifting. Surveyors determined the exact positions of the reflectors using a Global Positioning System (GPS) with post-processing to achieve centimeter accuracy.

Along the transect, sample sites are located every 250 m yielding 11 sites over the 2.5 km transect. Judging from previous SAR images of the area, this ensures that sample sites will closely bracket significant brightness changes on the SAR image. I sampled the snow conditions along the transect twice, the first time the distances between sample sites was "chained out" by stretching out a 50 m climbing rope between two people and repeating this five times for each sample distance (250 m). The second sample, I used a hand-held global positioning system (GPS) and followed the footprints from the previous transect to keep on track. The second sampling was

completed a week after the first because some measurements were not taken at each site on the first pass. The transect continued one kilometer beyond the upper reflector into the accumulation zone. The total transect length is 3.5 km.

Howard Glacier. On Howard Glacier I established an 850 m transect with five sample sites and no corner reflectors (Figure 4.3). It begins in the ablation zone and rises into deep snow. The first sample site was at stake 31 and the second was at stake 30. The other three sites were selected along the bearing lining up stake 31 and 30 and were located using GPS. The measurements on this transect give an opportunity to compare backscatter of opposite slopes: Commonwealth Glacier faces the SAR, while Howard Glacier faces away (Figure 4.2). On Howard Glacier it is likely to have higher degrees of specular reflection and different locations of the glacier radar zones due to the different aspect affecting the SAR incidence angle.

The Measured Surface Variables.

The variables measured at each site included: snow temperature, ice roughness, slope/aspect, snow depth, snow density, and snow grain size. Temperature affects liquid water content, which increases specular reflection off snow (Avery and Berlin, 1992; Hall, 1998; Jezek and Carsey, 1993; Mätzler, 1987). The temperatures on the glaciers in Taylor Valley in recent years have not often reached the melting point (Nylen, personal communication 2000). Ice and snow roughness increases radar backscatter. Snow and ice surfaces on the study glaciers are typically smooth (< 50 cm), except near the terminus where the amplitudes reach 10 m (Fountain et al., 1998). Surface orientation to an incident radar beam affects how the beam will reflect

and the depth of its penetration. Shallow dry snow is transparent to radar, while deeper snow will display volume reflection (Bindschadler, 1987; Hall, 1998; Jezek and Carsey, 1993). Internal density changes of the snow layers increase volume reflection (Rott and Mätzler, 1987; Shi and Doizer, 1993). Larger snow grains scatter radar more than small grains (Hall, 1998; Rott and Mätzler, 1987; Shi and Doizer, 1993). The snow grains on the study glaciers are typically small (<3 mm) (Fountain et al., 1998). In addition to measuring surface characteristics, a general description of each site includes: ratios of snow and ice cover, percentage coverage of cryoconite holes, percentage coverage of snow dunes, and crevasses.

I measured surface temperatures using a digital thermometer (accuracy within 0.1° C). For ice surfaces temperature was recorded by placing the thermometer in a small (1 - 5 mm) hole, shielding the area from the sun, and allowing the reading to stabilize within 0.5° C. By pushing the thermometer 1 - 5 mm into the snow, temporarily shielding the area from the sun, and allowing the reading to stabilize within 0.5° C an accurate snow temperature was recorded.

I measured ice surface roughness by laying a 2 m pole (the fiberglass snow depth probe was used) on the glacier surface and measuring the vertical distance from the pole to the ice surface. A folding ruler with millimeter increments was used to measure the vertical height at 5 cm intervals along the pole (Figure 4.8). On snow-covered ice, I tapped the folding ruler through the snow layers to the ice surface to obtain depth snow depth. The roughness is given as the standard deviation of values. Two sets of roughness measurements were collected at each site, one with the bar parallel to the SAR beam direction and the other with the bar perpendicular. I sighted

over a reflector and selected a landmark on the horizon of the Kurki Hills across the valley; this gave me an approximate SAR beam direction on Commonwealth Glacier. This landmark was then used to orient the pole. On Howard Glacier I used the centerline axis of the glacier as the approximate SAR beam direction.

I determined the slope, relative to the SAR beam, by using the inclinometer on a Brunton compass and an ice axe. The ice axe was laid on its side in a region that best represents the average slope and its length (75 cm long) averages the high points of the sample surface. I oriented the long axis of the ice axe parallel to the SAR beam direction, and placed the Brunton compass on the shaft to measure the slope. Facing the general fall line and comparing it to a landmark that was to the north determined aspect. This method determined directions to only the eight cardinal directions (or about $\pm 22.5^\circ$).

I measured snow depth using a chimney sweep pole with centimeter intervals marked along the shaft. The tip of the pole was a machined steel point that aided in breaking through thin ice-crusts. Four snow depth readings were taken at each snow site. A snow pit was dug at both reflectors, mid-way between the reflectors, and 500 m above the upper reflector. Snow stratigraphy was determined and three variables were measured in each snow layer: density, grain size, and layer thickness. I calculated snow density by weighing 100 cm³ of snow; density measurements were done for every layer thicker than 3.5 cm (due to the height of snow sample scoop). Grain size was determined by sprinkling snow on graph paper and estimating the average diameter. I measured layer thickness from the surface, to each layer using a folding ruler. The area around each site, within a 50 m radius was characterized as to

relative aerial fractions of type of surface (snow, ice) and any notable features (e.g. crevasse, cryoconite holes). The fractional area of cover (e.g. snow, ice, cryoconite holes) was established by a consensus of estimates between Andrew Fountain (my thesis advisor) and myself.

I brought a calorimeter method of measuring water content of the snow to the field (Akitaya, 1985) but the snow was very dry and the error of the method high enough that reliable measurements of low moisture content were not possible.

CHAPTER V

RESULTS OF THE FIELD MEASUREMENTS

The field campaign on Commonwealth Glacier lasted from January 19 to 26 and on Howard Glacier on January 27, 1999. Two SAR images were acquired: an ERS-2 on January 15 (Figure 5.1), and a Radarsat on January 19, 1999 (Figure 5.2). During this time the weather and the surface conditions of the glaciers did not vary. Along with the data collected specifically for this investigation, the LTER data collection of snow pit and stake measurements is also utilized (Appendix A). During the 1999 field season Paul Langevin made the mass balance measurements at the stakes. These data include snow layer thickness, mass, density and crystal structure.

Imagery.

The ERS-2 image is a high-resolution image with 12.5 m pixel spacing, and with VV polarization (Figure 5.1). The average incidence angle of the SAR beam was 23.1° , pixel spacing was 12.5 m, yielding 30 m resolution, and covering a

108 km² area. The image covers a small slice of Taylor Valley fortunately including all of Commonwealth Glacier. Unfortunately, almost all of Taylor Valley including Howard Glacier is off the image (Figure 5.3). The glaciers are identified on the SAR image by the shape, darker ablation area, and bright accumulation area. Lake Vanda is the only ice covered lake visible and is a middle-gray surrounded by dark bare earth (Figure 5.1).

Radarsat. The Radarsat image is a ScanSAR image with 50 m pixel spacing, and HH polarization (Figure 5.2). The average incidence angle of the SAR beam was 35°, pixel spacing was 50 m, yielding 75 m resolution, and covering a 512 km square area. The image includes the East Antarctic Ice Sheet, Ross Island, the McMurdo Dry Valleys including Taylor Valley, and Drygalski Ice Tongue. Glaciers are identifiable on the image, but because of the large pixel size, smaller glaciers like Howard require familiarity of the area to identify. Like the ERS-2 image, the (large) glaciers show flow lines (Drygalski Glacier), darker ablation areas, and bright accumulation areas. The Ross Sea is the darkest area of the image and bare earth a dark gray.

Transects.

Commonwealth Glacier. The ice roughness between the measurements perpendicular and parallel to the SAR beam is very similar and they correlate at

$R^2 = 0.8$ because of this, the orientation of the measurements are disregarded and the roughness measurements pooled. Standard deviation of roughness ranged from 0.7 to about 3 cm (Figure 5.4).

On both glaciers, I observed dune-like formations of snow that ranged from 0.10 to 100 m² in area and 4-48 cm deep. Because of their frequent flat-topped and steep sided edges, I called them called “snow tables” (Figure 5.5). Areal coverage of snow tables ranged from 10 to 50% (Figure 5.4), and the snow depths averaged 12 cm. Ice roughness and snow table coverage generally followed a similar pattern of roughness (Figure 5.4).

Areal coverage (density) of cryoconite holes (Figure 5.6) varied 0-10% (Figure 5.4), with depths to the exposed ice bottom averaging 14.4 cm deep with a maximum of 28 cm (Appendix B). The bottoms of the holes frequently contained a layer of sediment. The sediment, absorbing sufficient solar heat to melt ice, forms pools of water (Wharton et al., 1985). Many cryoconite holes had re-frozen caps, and because of this, I could not measure these depths (Appendix B). The cryoconite holes were difficult to spot because some were covered with snow and some of the ice caps were difficult to distinguish from the surrounding glacier ice.

Near-surface snow temperature measured as low as -3.7° , averaging -2.1° , and ice temperature as low as -3.5° , averaging -1.6° C (Appendix B). Air temperature was measured at the beginning of each day and ranged from -2.2 to -1.3° C.

The snowline on the transect began just below transect site #12 (T12) with an average snow depth of 15.3 cm and the maximum average depth on the transect measured at T16 of 67.6 cm (Figure 5.7). The snowline is an ambiguous demarcation: ascending the glacier snow patches become more-and-more frequent until the ice surface is completely ice covered. The snowline is defined in this study where the fraction of the ice surface is at least 90% covered by snow. Ascending the glacier, snow patches on the ice become more frequent, until they begin to merge, isolating ice patches until the surface is completely snow-covered. The transition at the snowline is much like M. C. Escher's "Sky and Water" woodblock print, where a black sea of fish (ice) transforms into a white sky of geese (snow) (Figure 5.8).

I dug snow pits at T12, and T9 (Figure 5.9). Depth of the layers, snow crystal descriptions, and hardness were recorded (Appendix B). Snow grains were separated into six categories: facets, rounds, wind crust, honeycomb, broken stellar, and hoar. Densities of the layers were not determined. At sites T13, T15, and T16 hard layers were noted as the rod was pushed through the snow to glacier ice and these depths recorded as layers (Figure 5.10). The snow was dry and ranged from fluffy and loose to a consistency of Styrofoam. I judged the snow to be dry by the look and feel and the fact that no melt on the snow, or the ice (which has a higher albedo and should melt first) was observed. The hard layers were wind-compacted snow or thin (1-2 cm) ice crusts.

Howard Glacier. My data collection was less extensive on Howard Glacier. Percent coverage (of ice, snow, snow tables, and cryoconite holes), snow depth, and

roughness were recorded (Figure 5.5f, Table 5.1). I only collected five sample sites because the transect quickly entered deep snow (Figure 5.11). Site 1 and 2 are in the ablation zone, site 3 is just above the snowline, site 4, and 5 were in the accumulation zone. Ice roughness averaged 2.0-4.5 cm and ice temperatures were not recorded.

Table 5.1: Cover and snow depth at sites near the snowline.

Site	Distance (m)	Percent cover of snow	Percent cover cryoconite holes	Snow depth (cm)
1 (Stake 31)	0	5	15	0
2 (Stake 30)	800	75	2	4.5
3	1200	100	—	10
4	1300	100	—	24.8
5	1600	100	—	40.7

CHAPTER VI

IMAGE PROCESSING

The two SAR images are “processed” but not terrain corrected: they are not projected in a standard coordinate system, and not corrected for brightness variations due to SAR peculiarities. The images are referenced in a time domain from the perspective of the satellite and only the image corners are geo-located. Because of the side-looking nature of SAR, substantial distortions in mountainous terrain exist in the image. Rectifying the images to a geo-referenced projection allows detailed comparison of SAR images with other images and maps (Domik et al., 1986; Partington, 1998; Naraghi et al., 1983), and in addition it allows detailed comparison of image brightness to specific locations on the earth. Significant changes in glacier slope and aspect, typical of alpine glaciers (in contrast to ice sheets), can affect the brightness variation of the SAR image and potentially mask the variations caused by changes in surface character. The ERS-2 image was processed using the ASF "Terrcorr" program (ASF website, 2000). Terrcorr corrects for radiometric variation, radiometric normalization, foreshortening, and geocodes the image. Terrcorr, like all terrain correction programs cannot correct

brightness variations for shadowing or layover. Their main disadvantage of terrain correction is that the image is resampled to the Digital Elevation Model (DEM) resolution, which may reduce the resolution of the final image. I found that setting up the software and running it is very time consuming.

Radiometric Calibration.

Radiometric calibration removes variations in the image caused by spatial and temporal SAR data acquisition characteristics. It consists of the computation of the difference between real radar brightness and those of a simulation (Domik et al., 1986). The real brightnesses are scaled by differences between actual and simulated values are redistributed to account for variations in surface terrain.

Terrcorr corrects the following three radiometric distortions:

Removal of Center-Bias. Like a flashlight beam, when a radar pulse contacts the ground, it contains more energy at the center than at the sides, causing the backscatter to be center-biased (ASF website, 2000). A portion of this bias is corrected at the processing facility and the remainder is completed by Terrcorr. At the processing facility, the antenna gain pattern is removed from the data (removing the center-bias) and the cross-track attenuations on the signal are removed (Tom Logan, ASF, personal communication). All of the corrections in the removal of center-bias are based on a geoid model of the earth. Terrcorr completes the subsequent radiometric corrections. The theorized center bias is mathematically inverted and the result is multiplied by each range line. Using an inverted antenna

gain pattern restores the noise to a flat pattern (called noise floor), which is then removed. This correction is called sigma-naught.

Range Backscatter Correction. Backscatter varies along the range due to changing incidence angle. At the far range, where the incidence angle is large, more specular reflection away from the satellite occurs (Figure 6.1). Making the uncorrected SAR image generally darker at the far range (Tom Logan, personal communication). At the ASF processing facility, the look angles are calculated across the span in range based on a geoid of the earth. These data are compared to the actual SAR signal return relative to look angle data, which are used to create a range correction vector. This vector is used to correct each line in range.

Radiometric Normalization. The incidence angle also varies with the slope of the terrain. Slopes facing the SAR beam will reflect much more energy back toward the sensor than slopes facing away (Figure 6.1). To normalize this effect, the ratio of the tangent of the local topographic incidence angle, derived for each pixel from the DEM, to the “global incidence angle,” (the tangent of the center of the SAR scene to the geoid incidence angle) is applied to the data (ASF website, 2000).

Foreshortening and Geocoding.

In the process of rectifying the image to a DEM, SAR image pixels are adjusted to a DEM, which is geocoded, thus acquiring the DEM’s positional

coordinates. The same rectification also corrects for foreshortening by stretching pixels on foreshortened slopes facing the SAR beam and compressing the pixels on the back faces to fit the DEM.

The Digital Elevation Model.

To use the USGS DEM of the Taylor Valley in Terrcorr, it had to be converted to Universal Transverse Mercator projection in a Land Analysis System (LAS) format and an ASF metadata file created (details of all the transformations and the Internet location of LAS programs in Appendix C). The projection change was accomplished using a Geographic Information System (ArcInfo). In the same program, the DEM was then converted to an American Standard Code for Information Interchange (ASCII) format. This format allowed the header to be easily removed and the “no data” values changed from -9999 to 0 (zero). These two changes formatted the DEM to be accepted into a LAS program and converted into a LAS format. A companion file containing the metadata was created using the ASF “makeddr” program. The LAS DEM and the ASF metadata file now comprise what is hereafter called the DEM.

Terrcorr Steps.

Terrcorr is a UNIX shell program, which runs a series of subroutines that radiometrically calibrate the image and geocodes it according to the general steps described earlier. Intermediate images and temporary files are made, compared to

one another, and deleted. The final result is a terrain-corrected image. Terrcorr runs through the following steps (ASF website, 2000):

1. The data are radiometrically calibrated.
2. The calibrated SAR image data are resampled to the resolution of the DEM. These data are called the preprocessed SAR image (Figure 6.2a).
3. The SAR image is truncated to the borders of the DEM.
4. The simulated SAR image is created by calculating the cosine of the angle between the local surface normal and the ray from the nominal sensor location and assigning theoretical brightness values to each pixel of the DEM. This gives the simulated SAR image the general appearance of the DEM surface illuminated from the sensor position (Figure 6.2b) (Naraghi et al., 1983).
5. Recognizable features that can be related geographically between the simulated SAR image (step 4) and the preprocessed SAR image (step 2) are correlated. The pixel offsets are calculated between the two images.
6. From the pixel offsets, a polynomial function is calculated to spatially transform (warp) the image to the simulated SAR image (Domik et al., 1986), creating the terrain corrected image (Figure 6.3a).

Details in installing and running Terrcorr are described in Appendix C.

Radarsat Terrain Correction.

Terrain-correcting ScanSAR images are difficult because the location data for individual pixels are incomplete (Ron Kwok, personal communication). The

pixel size also varies in range considerably more than ERS-2 data. Because of these differences, ScanSAR could not be corrected using Terrcorr. Dr. R. Kwok at the Jet Propulsion Laboratory (JPL) in Pasadena, California corrected the Radarsat image in this thesis. The JPL terrain correction routines and Terrcorr are virtually identical in their basic operation, as JPL developed both programs. Using a template of ScanSAR pixel sizes on a geode, and the location data provided, Dr. Kwok was able to assign the pixel location data for the entire image. With this location data, the preprocessed SAR image was created, and the terrain correction was run as described above (Figure 6.4).

Peculiar Characteristics of the Corrected SAR Images.

The corrected SAR images display visual characteristics that are different from uncorrected radar and other remote sensed imagery. The outline is irregular along some edges. In mountainous areas the border irregularity is very rough. Also in mountainous terrain, the slopes facing the SAR are “smearly.”

Rough Edges. The near-range edge of the ERS-2 corrected image (southwest side) has a rough edge due to steep topography (Figure 6.5). Layover would be present in this area, but because the edge of the radar scene runs parallel to a very steep ridgeline, the top of the ridge received backscatter and the base was not illuminated. In the terrain correction this ridge was shifted northwest to its proper location, leaving a rough edge where no information was collected. In the uncorrected image this edge is a straight line and shows significant layover. In the

southwest side of the ERS-2 image, next to Canada Glacier, is a black irregular region of radar shadowing from a mountaintop. The east edge of the corrected ERS-2 and Radarsat images is irregular because the DEM ends at the coastline and is removed during the "DEM clip" step of the terrain correction. On the Radarsat image (Figure 6.6) similar rough edges are present on the southern edge (near range) of the corrected image.

Smearyness on Steep Slopes. The corrected images contain parallel lines, which soften and smear the image near steep slopes. A terrain corrected image of a steep slope that has foreshortening or layover will have streaks on the slope facing the SAR (Domik et al., 1986). Slopes steeper than the SAR incidence angle (23° for these data), exhibit this smearyness error. The pixels on slopes facing the SAR must be spread to fit the simulated SAR image (*ibid*). The spreading is in the range direction. In the same way a silly-putty image of a newspaper comic strip will turn into lines when stretched too far, as SAR data is stretched it creates similar lines. Compacting the pixels into the slopes facing away from the SAR improves the image. Some streaks appear on the lee slope around Commonwealth Glacier on both the Radarsat corrected image (Figure 6.4a) and the auto-corrected ERS-2 image (Figure 6.3a). This error is probably due to DEM inaccuracies first causing poor correlation (between the simulated SAR and preprocessed SAR images) and ultimately streaking on the wrong side of the mountain in the terrain correction.

Reflector Backscatter Shape of the ERS-2 Image.

In the uncorrected ERS-2 image (Figure 6.3a), reflectors are oblong in the look direction by five pixels. The satellite-borne precision processor resolves azimuthal position better than in the range direction (Wade Albright, Quality Assurance Engineer, ASF, personal communication). At the time of image acquisition, range resolution was 19.8 m and azimuth resolution 26.6 m, with a maximum allowed deviation in range and azimuth of 30 m (ASF website, 2000). This resolution is the smallest discernable feature that can be identified by the strength of the signal. However, the pixels that are in the image are smaller than this number. Pixel spacing is just used to measure distances within an image. This image, which is referred to as a “full resolution” product, has been multi-looked (averaged) so that the pixels become square (12.5m x 12.5m). This is done because it is much easier to work with square pixels than using the resolution numbers (Wade Albright, personal communication). This is why the pixel size of the uncorrected image is 12.5 m (as indicated in the image metadata), and the resolution is 30 m (as indicated at the ASF website). This is also why there will never be a feature in an image that is represented only in one pixel. In the terrain corrected image, the oblong shape is removed because the data were resampled to the DEM resolution of 30 m (Figure 6.3). The oblong shape changed only two pixels in length because of the loss in resolution (when the data was resampled to the DEM resolution) and the pixels being averaged and generalized.

Comparison of ERS-2 Images Between Manually Correlated, and Auto-Correlated.

The auto-correlated (Terrcorr) image exhibited "smeariness" on the mountainsides sloping away from the SAR beam. Normally this correction artifact is on the slopes facing the SAR beam. This raised concern about the accuracy of the correlation, a concern shared by Tom Logan from ASF, who speculated that the DEM might contain some inaccuracies. Because of this, the terrain correction process was run twice, once allowing Terrcorr to auto-correlate, and a second time, which was manually correlated (Figure 6.7). I manually adjusted the offset to match the edges of Commonwealth Glacier between the simulated SAR image and the preprocessed SAR image. The pixel displacement from the simulated image to the preprocessed SAR image was placed in a temporary file and the program re-run with the manually calculated displacement figures (Appendix C). The manually correlated image displays the "smeariness" on the facing slopes as expected.

To quantify the differences between the auto- and manually correlated images, the distances between the reflectors was used to determine which image was most accurate (Table 6.1). From the GPS measurements on the ground, the distance between them is 2417 m (with an error in location within 1.0 cm). Because the survey error is much smaller than the resolution of the imagery, this survey distance is used without consideration of error. Measuring the distances on the SAR images was done using ENVI 3.2 computer software (Environment for Visualizing Images Program Research Systems, Boulder, Colorado).

Table 6.1: The distance between reflectors on the ERS-2 image (m).

Survey	2417 ¹	Difference
ERS auto-correlated	2431±33 ²	14
ERS manually correlated	2368±33 ²	-49
ERS uncorrected	2128±33 ²	-289

¹ this distance is accurate to within a centimeter.

$$^2 \text{ error} = \sqrt{(\text{range_resolution})^2 + (\text{azimuth_resolution})^2}$$

The auto-correlated image is the closest to the survey distance, and is within the estimated error. The manually correlated image is outside the estimated error.

Because Commonwealth Glacier slopes towards the SAR position, the (uncorrected) slope is slightly foreshortened reducing the distance measured on the image. Both the terrain corrections, however, adjust the distance between the reflectors to a distance within 49 m of the true distance.

To further quantify the differences between the uncorrected, auto-, and manually correlated images, the azimuth of the transect line between reflectors was examined (Table 6.2). The azimuth from the lower to upper reflector was 303.55° using precise GPS data. North was determined on the uncorrected images from the “scene center heading” azimuth in the image metadata, which gives the azimuth of the centerline (from bottom to top) of the uncorrected image. On the corrected image north points to the top of the image since the SAR image was rectified to the DEM, which is oriented. The reflector azimuth on the image was determined from paper copies of the image using a protractor and pencil. The terrain correction process (manual or auto) appears to work very well in azimuth accuracy (Table

6.2). The uncorrected azimuth is 12.5° off and is likely an error of estimating the image orientation.

Table 6.2: Azimuth of the reflectors on the ERS-2 image.

	Azimuth	Error	Difference
Survey	303.55°	“precise”	
ERS-2 auto-corrected	302°	$\pm 1^\circ$	1.55
ERS-2 manually corrected	303°	$\pm 1^\circ$	0.55
ERS-2 uncorrected	291°	$\pm 1^\circ$	12.55

Although the distance between reflectors (Table 6.1) is less accurate in the manually corrected image, it is only off by 1.5 pixels (45 m). The image also *looks* better in the steep ridges to either side of the Glacier (Figure 6.7). The difference in azimuth is negligible. When I calculated the pixel offset between the simulated SAR and the preprocessed SAR image, I could *see* that I was lining up the images to within a pixel. Because of this, I have more confidence in the manually corrected image to for the Commonwealth Glacier. However, the correlation outside Commonwealth area is likely to be more accurate with the auto-correlation because that correction adjusted the offset using the data across the entire image. By manually-correlated the image using data limited to the terminus of Commonwealth Glacier and the ridgelines to either side, increased the error in other parts of the image.

A third measure of error is comparing the surveyed locations of the reflectors to the locations on the image. Using this method on the SAR images, the upper reflectors are located exactly. The lower reflectors are off by 168 m (manual) and 156 m (auto) both to the north. Using this method on the DEM and comparing

the estimated location of the reflectors and the plotted location yielded an error of 400 m to the south on both reflector locations. The errors in the auto correlation are very likely due to inaccuracies in the DEM and location errors in the spacecraft position (Dr. Ron Kwok, personal communication).

Five areas are noted that indicate the terrain correction is more accurate in the manually corrected image for analysis of the Commonwealth Glacier. First, on the manually correlated image there are two bright bands that make up the slope of Mt. Falconer ridge (Figure 6.8). The lower band is not a steep slope of the ridge (Figure 6.9), but is surprisingly bright. A formal ground-truth of that area was not conducted but, from helicopter flights, the area was observed to be scattered with large boulders, which may have created a strong SAR return due to roughness. Where the slope increases over 24° , the layover (and second bright band) begins (Figure 6.9, 6.10). The auto-correlation algorithms negligibly correct this band (Figure 6.7a), smeary lines of data are in this location on the Mt. Falconer ridge, but the process is not as complete as in the manually correlated version (Figure 6.7b). Second, the bright spot from the upper reflector is smaller in the manually correlated image by one pixel. Third "King Pin" nunatak, "unnamed nunatak", and Hjorth Hill (Figure 6.8) correspond to the shape of the DEM in the manually correlated image (Figure 6.10). Fourth, the steep cliff face at the north edge of Commonwealth Glacier mimics the shape of the DEM more accurately in the manually correlated image (Figure 6.10). Fifth, on the auto-correlated image, if the Mt. Falconer ridgeline to the west of Commonwealth Glacier is extended onto the

glacier, it intercepts near the lower reflector position. Comparing to a USGS Quadrangle map this line is intercepting 1000 m too far down glacier. The mismatch is due to layover remaining in the auto-correlated image of the ridgeline. The same intercept point on the manually correlation image is 1187 m up glacier from the lower reflector, which is exactly where it should be when compared to the map.

A general comparison of the ERS-2 SAR image of Commonwealth Glacier between the manually correlated and uncorrected image (Figure 6.11) indicates that the terrain correction significantly alters the orientation, shape, and contrast on Commonwealth Glacier. The reflectors are clearly visible on both images, but the uncorrected image they stand out sharply due to the higher contrast. General features like ridgelines, nunataks, and the outline of glaciers compare easily between images. The most significant differences are the spatial adjustments of the image to fit a projection and the stretching of foreshortened slopes. There is also a brightness difference between the auto and manually corrected images.

Radarsat Image Evaluation.

The Radarsat image is a coarse image compared to the ERS-2, due to the ScanSAR mode and pixel size of 50 m, which makes analysis more difficult for small areas. The terrain corrected image contains correlation errors in steep terrain, which is shown by smeariness on the slopes facing away from the SAR beam

whereas the smearyness should be on the facing slopes (Figure 6.4). Like the ERS auto-correlation, a polynomial warp function was applied to conflate the preprocessed SAR image to the simulated SAR image, creating the terrain-corrected output image. Because of the way data are collected and recorded in the Radarsat ScanSAR (as previously described), the ERS-2 data contains much more data of pixel location and is much more suitable for detailed analysis (Ron Kwok, JPL, personal communication).

Comparison of Radarsat Images Between Corrected and Un-Corrected.

The distance between the reflectors on the corrected Radarsat image is close to the surveyed distance, 15 m. The uncorrected distance is much shorter, by 207 m (Table 6.3), than the survey distance due to radar foreshortening. Because of the similar incomplete terrain correction as seen in the ERS auto-correlation image (layover still present, data correction smears on the mountain sides sloping away from the SAR beam) the same correlation errors that are likely caused by the DEM are creating similar incomplete terrain correction artifacts in the Radarsat image. Unlike the ERS-2 data, the Radarsat data is uncalibrated for error in range and azimuth. The error assigned for the corrected image was taking into account errors in distance measurements.

Table 6.3: The distance between reflectors on the Radarsat image (m).

Survey	2417±.001 ¹	Difference
Radarsat corrected	2402±50 ²	-15
Radarsat uncorrected	2210 ³	-207

¹ this distance is accurate to within a centimeter.

² 1/2 pixel error on each reflector.

³ errors undetermined.

The azimuth of the reflectors is compared to assess the differences between the uncorrected and corrected images (Table 6.4). Unlike the ERS-2 azimuths, the uncorrected is more accurate and the corrected image is different by 5.5°. The uncorrected azimuth may be more accurate than the ERS-2 azimuth because, Commonwealth Glacier where the deflection was measured is closer to the center of the scene where the base azimuth is known from the metadata (Figures 5.1, 5.2). The corrected azimuth may exhibit a larger error because of the difficulties in assigning location data for individual pixels with ScanSAR data and running the terrain correction with larger degrees of estimation.

Table 6.4: Azimuth of the reflectors on the ERS-2 image.

	Azimuth	Error	Difference
Survey	303.55°	“precise”	
Radarsat corrected	287°	±1°	16.55
Radarsat uncorrected	304°	±1°	0.45

The Radarsat ScanSAR corrected and uncorrected (Figure 6.4) images also allow general comparison. General features are cross-identifiable on both images such as Mt. Falconer Ridge, the shape and location of the terminus and sides of Commonwealth Glacier, unnamed nunatak, and the ridgeline to the north that demarks the edge of the glacier. Like the comparison between the corrected and uncorrected ERS-2 images, the spatial adjustments of the image to fit a projection

are significant. Unlike the ERS-2 image there is very little brightness difference between the auto and manually corrected images. This is due to the method of radiometric normalization used.

The comparison of corrected and uncorrected Howard Glacier images is difficult. The corrected image (Figure 6.12a) contains a great deal of error due to an obtusely sloping mountainside the relative to the SAR beam (Figure 6.13). The only area that can be positively identified is the terminus and only because of familiarity of the area. Howard Glacier is somewhat easier to identify on the uncorrected image (Figure 6.12b), but the contrast between the terminus and bare earth is very low, once again familiarity of the area is necessary to properly interpret the image.

CHAPTER VII

IMAGE ANALYSIS

This chapter compares the SAR images from Radarsat and ERS-2 to each other, and to glacier surface measurements. Glaciers, other than the primary study glaciers, and ice-covered lakes in the valley are also examined using SAR imagery. At ASF, the SAR data were converted from decibels to an 8-bit digital number (DN) grayscale so that it can be viewed as an image; pure black is 0 and pure white is 255. Interpretations of the SAR brightness variations to surface characteristics are hypothesized. I anticipated that significant penetration of the radar energy into dry snow would result in an offset of the SAR detected snowline relative to the true snowline. The field measurements collected on Commonwealth and Howard Glaciers are included in Appendixes A and B. Appendix A summarizes the data from the network of stakes measured twice annually to assess the glacier mass balance. The specific data include only those measurements taken in January 1999, close to the date of SAR image acquisition. Appendix B summarizes the data collected along the transect set up between the two reflectors on Commonwealth Glacier.

Surface Brightness Variation.

The standard deviation of surface roughness along the transect on Commonwealth Glacier never exceeded 3.1 cm (Figure 7.1a). The only ablation region that imaged bright (rough) was off the transect, near the terminus, where large melt channels (1-15 m deep) exist and are rougher than the calculated radiometric roughness. No correlation emerged between cover of snow tables or cryoconite holes and SAR brightness (Figure 7.1b,c).

Glacier ice surfaces have less backscatter (darker) than snow surfaces (Figure 7.2). The SAR brightness of four pixels around each sample site (stakes and transect) (Figure 7.3) are averaged, to take into account for errors in geo-location, and compared to SAR brightness. In the ice (ablation) zone, the brightness ranges from DN 141 to 187. The snow (accumulation) zone is brighter, ranging from DN 189 to 249.

As snow depth over ice increases, SAR backscatter increases (Figure 7.4). The linear regression values for both graphs is high $R^2 = 0.75$ and 0.77 . The snow depths in ablation zone are average snow-table or snow patch depths. No linear relationship of brightness to snow depth exists for the ablation zone. This may be due to backscatter dominated by ice surface roughness. The roughness along the transect did not differ significantly yielding a cluster in the ablation brightness points in the snow depth weighted average graph. In the ablation zone the SAR beam is probably specularly reflecting off the buried glacier ice and, to an insignificant extent, volume reflecting in the shallow snow. The brightness linearly increases in the

accumulation zone because the deeper the snow gets, the more it has an opportunity to volume reflect, and less specular reflection off the glacier ice is occurring.

As previously mentioned in chapter five, the precise location of the snowline on Commonwealth Glacier is ambiguous because it is a transition rather than a sharp line. For this analysis, the snowline is where the cover is a minimum of 90%. At T12 and T13, the transition from ice to snow-cover occurs over 100 m; around stake 12 the transition is much longer enlarging the width to 100-250 m. As the snow patches converge, the snow depth increases. At T13, the snow cover was 100% and the average depth 15.3 cm. Along the mass balance stakes the snowline is interpolated to be 485 m below stake 12 (between stakes 11 and 12) ranging from 235-735 m (± 250 m) below stake 12.

Location of the Snowline using SAR. Because T13 is bright in the SAR image and it was just above the actual snowline, it appears that a snow thickness of 15.3 cm can be observed. Both snow tables and snow patches over the ice are likely transparent to the SAR beam. The depths infrequently exceeded 15 cm, averaging 12 cm for snow tables and never exceeding 12 cm on snow patches.

I ran a supervised classification using ENVI to define the SAR snowline (Figure 7.5). The training areas were located on the “dark” ice and “bright” snow zones. Each zone used one training area, consisting of 25-30 pixels each. The snow training area included a four-pixel average of the SAR brightness at T13 (189) to make sure this location was included in the snow class. The snow pixels were assigned the color white, and the dark ice pixels were assigned gray. The SAR

snowline is indicated on the map where the boundary between white and gray occurs and: it is on the glacier, and it is in the approximate location of the snowline (there is a white-gray border at the terminus).

I also ran a second “isodata” unsupervised classification (Duda and Hart, 1973) using ENVI with two classes across the Commonwealth Glacier area (Figure 7.5) (including some non-glacier areas). In an isodata classification technique, initial class means are calculated in each training area and then the pixels are clustered into the nearest class using the minimum distance. The result is similar to the supervised classification (Table 7.1). The unsupervised classification snowline is 0-60 m higher than the supervised classification.

Table 7.1: Supervised and unsupervised SAR classification categories.

Color	Category	Supervised classification (DN)	Unsupervised classification (DN)
Gray	Ice	0-188	0-198
White	Snow	189-255	199-255

Although done quite differently, the two classifications yielded results quite similar. This is part because the analysis was binary. If only the glacier surfaces were used, the similarity would not be too surprising; the rapid change of brightness would separate out in the middle. However, the fact that the unsupervised classification, including substantial areas outside Commonwealth Glacier, closely mapped the snowline is surprising. This fact that an unsupervised (isodata) binary classification

determined the snowline to within 60 m indicates that large areas could be snowline mapped with some accuracy without surface verification.

The SAR snowlines determined by the classification routines compare well with the snowline seen on oblique photographs taken from a helicopter (300-500' above ground level) at the same time as the data collection (Figure 5.5). Only the upper reflector and the meteorological station (near stake 11) are identifiable for ground reference location (the original photographs are slides and these features are difficult to pick out in the reproductions in this thesis). The general shape of the west-side snowline matches the shape and location in the SAR image. On the east side the approximate position and shape of the snowlines in the photograph and the SAR image appear to correspond. Because of the difficulties of comparing a georectified overhead view to a low-altitude oblique photo, the comparisons are only estimated to be good within 200 m. Comparisons between the apparent shapes of the snowlines are within 50 m.

A Landsat 6 image (band 4, near infrared, 0.76-0.90 μm) acquired from United States Geological Survey (USGS) and taken on January 6, 1993 (Figure 7.6a) was utilized to further define the snowline. Although the image was acquired six years prior to the SAR imagery, the shape and location of the snowline, including the ice patch correspond. This suggests some stability in the year-to-year snowline in this region. The SAR snowline also compares well with overhead aerial photographs (INSTAAR MCM LTER website, 2000) taken six years previously (November 1993) (Figure 7.6c). Again, the shape and location of the snowlines, including the ice patch

correspond closely. Both of these images are out of date with the field measurements and SAR images, however, since they both appear to correspond to each other and to the SAR image, the snowline in 1993 was likely vary near to its 1999 shape and location. As mentioned in Chapter III, maximum estimated penetration of SAR into dry snow is 21.7 m (Rott et al., 1993). On Figure 7.6c is a best estimate of where the SAR snowline would be if 10 m of snow were transparent (ten meters was used to include the round-trip path). The location of the estimated SAR penetrated snowline (Figure 7.6c) and the SAR snowline (Figure 7.6b) shows a significant theoretical displacement.

The measured snow data from the transect and stake data is used to compare the accuracy of the two classification snowline results. The supervised classification accurately crossed just below T13, where the snow cover was 100% and the depth was 15 cm, and just above stake 12, where the snowline was patchier and measured 27 cm deep. T13 maps just above the snowline in the supervised classification, since it was used as the lowest brightness for the snow class. The SAR snowline surrounds stake 12 on three sides, forming a cul-de-sac of ice. Using the range of the actual snowline estimated for this region (235 to 735 m below stake 12), the SAR snowline matches the actual snowline. The unsupervised classification snowline crosses T13, 60 m too high and stake 12, 335-585 m too high. The snowline for T13 is within the 100 m transition zone for this area and stake 12 has an arm of the snowline below it that falls within the range of the snowline estimate for the area. Although both

classification schemes identify similar SAR snowlines, the supervised classification seems more accurate.

A problem with the classifications is the misclassification of a dark region near in the upper accumulation zone where no exposed or near-surface ice exists (this region is discussed in more detail later). Anomalies such as this, and areas outside the glacier (which are undefined in this analysis) all require an operator to supervise the classification. The SAR determined snowline in the rest of this analysis will be that resulting from the supervised classification and referred to as the “SAR snowline” (Figure 7.7).

Why Did the SAR Snowline Match the Actual Snowline?

One unexpected result was the match between the SAR snowline and actual snowline. The SAR snowline was anticipated to be displaced up-glacier due to radar penetration through the thin snow layer to glacier ice and reflect away from the sensor. The SAR snowline would be displaced up glacier to a point where the volume reflection of the snow would be sufficient to scatter energy back to the sensor. For example, with a small mass balance gradient with altitude (typical of polar glaciers), and 10 m penetration (10 m in and 10 m out adding to 20 m, the distance that was estimated for full penetration in homogeneous snow by Rott and Mätzler (1987), and Ulaby, et al. (1981)), roughly a 2 km shift would occur in the apparent snowline for a glacier with a 5° slope. This did not occur: the SAR snowline matched the actual

snowline. Three factors are offered to explain this: temperature, sub-surface roughness, and enhanced volume backscattering.

Temperature. Ulaby et al. (1981), pointed out the moisture content of snow greatly affects its reflectivity and small changes in temperature near 0° C have the greatest effect on how the snow scatters. The ice surface might have slightly greater moisture content than the snow because of the albedo differences between the two. Air temperatures during the fieldwork and image acquisition averaged -3° to -4° C (Table 7.2) with a good wind. High sublimation rates are common in the valley, cooling and drying the surface significantly (Lewis et al., 1995). If the ice surface was wetter than the snow, the image should exhibit a broad transition zone between the ice and snow because the patchy snow and ice would present a mixture for the SAR pixels, changing in tone with the changing snow cover. This was not apparent in the image.

Table 7.2: Temperatures at the Commonwealth Meteorological Station.

Date	Average Temperature (° C)	High temp. (° C)	Low temp. (° C)
1/15/1999	-3.41	0.31	-7.86
1/19/1999	-4.51	-2.22	-4.51

Subsurface Roughness. The standard deviation of the subsurface roughness along the transect never exceeded 3.1 cm. The only ablation region that imaged bright due to roughness is near the terminus, where large melt channels (1-5 m deep) exist. It was not noted in any snow pits, nor is it likely that processes are operating on the

smooth snow surface that would cause differential melting and re-freezing of layers that would surpass the wavelength of the SAR (5.66 cm), which is the minimum radiometric roughness.

Enhanced Volume Backscatter. Layers of different density in snow act as a specular reflective surface (Mätzler and Schanda, 1984; Tsang et al. 1985; Ulaby et al., 1981) in which part of the beam is reflected and part transmitted (Figure 7.8). I hypothesize that in thin, dry snowpacks, reflection off multiple internal layers increases the total path length of the beam and enhances the opportunity for volume scattering. Most of the energy would be scattered by the near surface layers because the deeper layers receive less energy and contribute a diminishing portion to volume scattering (Forster et al., 1991; Ulaby et al., 1981).

The snow pits dug on Commonwealth Glacier display multiple snow layers (Figure 7.9). As mentioned previously, the snowline was located only 5 m down glacier from site T13 and 235-745 m below stake 12. The depth of snow at T13 was 15.3 cm, with a brightness of DN 191, and the depth at stake 12 was 27 cm with a brightness of 192. One snow layer was identified at T13 and 5 layers were identified at stake 12. Probing of the snow at T13 revealed at least one layer and perhaps a snow pit would have revealed more.

For enhanced volume backscatter to exist, layers must reflect the radar, causing the beam to volume-interact with the snow at a shallow depth. The volume reflection is then able to escape the snowpack with little attenuation of radar strength. The propagation of radar energy through snow is governed by the snow's relative

dielectric constant (Glen and Paren, 1975; Hall, 1998; Ulaby et al., 1981). For SAR frequencies, the dielectric constant for dry snow is directly related to density (Glen and Paren, 1975),

$$\epsilon = (1 + 0.51\rho_s)^3 \quad (7-1)$$

where ϵ is the relative dielectric constant of dry snow, and ρ_s is the density of snow in g cm^{-3} . An electromagnetic wave passing from a medium with one dielectric to a medium with a different dielectric is reflected and/or refracted. The magnitude of the reflection coefficient is given by

$$\Gamma = \frac{\frac{1}{\epsilon_2^2} - \frac{1}{\epsilon_1^2}}{\frac{1}{\epsilon_2^2} + \frac{1}{\epsilon_1^2}} \quad (7-2)$$

where Γ is the reflection coefficient, ϵ_1 is the dielectric of the first layer, and ϵ_2 is the dielectric of the second layer (Forster et al., 1991).

Using equation 7-2 and snow density data, the reflective behavior of the SAR beam for each layer can be estimated. Density profiles exist for only two pits on Commonwealth Glacier, dug to glacier ice at stakes 12 and 14. The dielectric of air is 1.00, ice is 3.17 for frequencies from 1 MHz to well above the microwave region (Lide, 1999), and the dielectric for snow was calculated using equation (1) and reflection coefficients calculated using equation (2). The densities and reflection coefficients for the layers are shown in Table 7.3. Absolute values were used because the sign of the reflection coefficient only indicates whether the reflected wave is in phase with the incident wave (Alonso and Finn, 1967) and is not important in this

study. Surface layers of snow were too thin (~ 1 cm) to measure at stakes 11 and 12 and densities were inferred from surface layers at the nearest stakes (10 and 14, respectively).

Table 7.3: Reflection coefficients for the layers at Stakes 12 and 14.

Thickness (cm)	Density (g cm^{-3})	Dielectric	Reflection Coefficient for boundary layer below
Stake 12			
surface		1.00	0.06
2	0.15	1.25	0.03
8	0.23	1.39	0.04
5	0.36	1.66	0.04
8	0.24	1.41	0.02
6	0.31	1.55	0.18
glacier ice	0.89	3.17	
Stake 14			
surface		1.00	0.09
1	0.25	1.43	0.01
8	0.29	1.51	0.05
7	0.45	1.86	0.05
26	0.30	1.53	0.04
24	0.19	1.32	0.21
glacier ice	0.89	3.17	

Figure 7.10 shows a hypothetical radar beam path for stake 12. The magnitude of the reflection coefficient was used to scale the width of the radar beam to show relative magnitudes of transmission and reflection. In comparison to the total path length of a snowpack without layers, the five layers in at stake 12 increase the path length by a factor of 1.8. Because the coefficient of reflection is low, only one reflection per layer is shown and the attenuation of the refraction is negligible. Based

on this first order analysis, the 29 cm snow thickness has an effective thickness of 52.2 cm.

Down-glacier from the actual snowline, the snow patches seem to be transparent to the SAR beam, yet their depth, roughly 12 cm, is close to the 15 cm depth of the SAR snowline. Stratigraphic observations indicate that these patches did not contain layers and therefore enhanced volume reflection is minimal. In addition, the patchiness itself reduces the backscatter because of the intervening areas of clear ice. The speckle observed in the ablation zone may be due to large but infrequent patches of snow, although other explanations (e.g. roughness) exist. Resolution of this question requires more field data.

Results from snowline mapping using SAR on Howard Glacier are inconsistent with the results from Commonwealth Glacier. The glacier only appeared on the Radarsat image because the ERS-2 scene did not cover that part of the valley. The aspect and slope of Howard Glacier faced away from the SAR beam at a sharp incident angle of about 10-23°. The entire glacier imaged dark with some tonal variation to indicate the transition from the snow to ice surfaces. However, the terrain correction degraded the resolution of the image sufficiently that it was nearly impossible to use. Because of this, the unprocessed image was used. These poor characteristics are probably attributed to the high incidence angle of the beam.

Enhanced Volume Backscatter is the best hypothesis explaining the shallow volume reflection seen on Commonwealth Glacier. More field data is required to specifically tie SAR brightness to snow depth, layering and density. Also needed is a

range of incidence angles that work for the Taylor Valley snow type, as noted on Howard Glacier the snowline was not accurately mapped, most likely due to excessive incidence angle.

Comparison Between Radarsat and ERS-2.

Figure 7.11 shows that the brightness variations along the transect for each satellite correspond closely with a correlation coefficient of 0.76. The SAR transect was taken from the cliff-edge of the glacier, through the reflectors, to the steep slope on the far edge of the glacier (Figure 7.12). Surface measurements were only collected from the lower reflector to 1 km up glacier from the upper reflector. The glacier margin faced the SAR platform and due to its steep slope was very bright and easily identified on all SAR images. The ridgeline to the north of the glacier, where the SAR transect terminates is mostly bare rock with thin snow at the base.

The ERS-2 image, the lines are offset from each other but exhibit similar patterns (Figure 7.13). This is due to the radiometric correction used in Terrcorr. The difference in magnitude between the two sensors is largest in the ablation zone and smallest in the accumulation zone of the glacier. In the ablation zone, the brightness (except for the reflectors) is rather flat. Farther away from the reflectors the correlation is less because of differences due to projection. The difference between the corrected distance and the uncorrected is almost 1000 m, this occurs because the corrected image is rectified to a DEM and the uncorrected image is still in a reference plane relative to the satellite and not georeferenced. The geometric differences

between these two images effects varying distance measurements. Some of these differences can be seen when comparing the corrected and uncorrected shape of Commonwealth Glacier in Figure 6.11.

The Radarsat corrected and uncorrected brightness values are similar (Figure 7.13) with a correlation coefficient of 0.64. Between the reflectors, they are extremely close with a correlation coefficient 0.91. In the lower half of the snow zone, the values are similar, but in the upper half the reflector brightness comparisons become more ambiguous. Once again, because of projection differences, the uncorrected line terminates 500 m shorter than the corrected line.

The comparison between the two corrected images (Figure 7.14) show that the brightness generally parallels one another ($R^2 = 0.84$). The Radarsat image has two spikes in the brightest part of the snow zone that is absent in the ERS data. The cause of the two spikes is unknown, but the main difference between the SARs is polarization. HH polarization (Radarsat) is sensitive to horizontal features; perhaps there is a buried layer feature the horizontal polarization is efficiently backscattering. The difference in magnitudes between the two transects is that different radiometric corrections were used; however the patterns of brightness (as indicated in the high correlation) is very similar.

The transect crosses the snowline soon after passing the upper reflector and the brightness values gradually increase to the maximum data value (255) and subsequently decreases. The area in the upper snow zone near stake 19, 21, 22, 23 (Figure 7.3) are darker than the surrounding snow areas. The aspect of the stakes is

flat (stakes 20, 21) and northeast (stakes 19, 22, 23). The slope for the whole area is mostly flat with a few areas reaching 11° . Nearby at stakes 17, and 18 the backscatter is very bright and has a northeast (stake 18) or southeast (stake 17) slope. It seems unlikely that orientation to the SAR beam is causing the darker areas; a more likely cause is that there are snow conditions that are reducing the backscatter. Thomas Nylen investigated the area for hard layers around the area of stakes 19 and 21 in November of 2000. The snow surface of the area is covered patches of hard, 3 cm thick wind crust with snow in between (Appendix D). Most of the buried hard layers were fairly thin, some of the ones that could not be punched through, the layer sounded hollow. The snow between the hard layers was soft and easy to pass the probe rod through. The average depth the probe rod could be passed to was 165 cm (35-290 cm). Layers were encountered between 25-180 cm deep. The area is in a gully running from the west-northwest to east-southeast. The region is a depression likely formed by winds draining from higher elevations (Nylen, personal communication). The mass balance at stake 21 is frequently a lower positive balance (hence less snow at the surface) than the neighboring stake 20. Although this observation is made a year and a half after the SAR images were taken, the processes and surface conditions could very well be similar. If this is true, the SAR might be specular reflecting off the hard crusty layer on the surface, or near surface, and not allowing penetration and volume reflection.

The lengths of the corrected SAR transects differ by 300 m (Figure 7.14). This difference could be due to errors in plotting the ends of the transect on the SAR

images, differences in SAR look angle, and random errors unique to each sensor (i.e. accuracy of the precision processor, and spacecraft location error). Were it not for the two spike anomalies and the differences in the overall distances, the two curves would be very close in pattern.

Howard Glacier.

Howard Glacier is only visible on the Radarsat image because the ERS-2 image does not include that part of Taylor Valley. As described in Chapter VI, Howard Glacier slopes to the north at slopes ranging from 10° to 23° creating a local incidence angle of the Radarsat beam of 34° - 47° . Given these geometric characteristics, severe distortions were created in the corrected image and I found the uncorrected image easier to interpret.

Examination of the spatial pattern of tonal differences on Howard Glacier reveals veins running down the axis of the glacier with some dark lines far up into the accumulation zone. The ablation zone is characteristically dark. I determined the SAR snowline on the glacier using the same unsupervised isodata classification procedures previously described. The unsupervised classification was used because the uncorrected image was used for analysis and exact location of snow sample sites cannot be accurately located. Comparing the SAR snow line with observations in the field (Figure 7.15) indicate that that there is uphill displacement of the SAR snowline relative to the snow line, however the locations of the snow survey and transect sample sites is extremely difficult to plot. Examining the snowline from the January

6, 1993 Landsat 6 image shows a snowline that is lower on the glacier than the SAR snowline. The Landsat image is six years out of date, however, the Landsat snowline crosses the mass balance stakes just above stake 30, which corresponds with the field observations. At stake 30, the SAR snowline is displaced up-glacier from the actual (and Landsat) snowline (Figure 7.16). The displacement is caused by the local incidence angle of the beam being large. This causes more specular reflection off all density interfaces than was occurring on Commonwealth Glacier. Volume reflection is occurring within the snow mass, however the snow/air and buried density interfaces specularly reflect higher percentages of the total SAR energy than was occurring on Commonwealth Glacier. The increase in specular reflection off the air/snow surface and shallow snow density interfaces sends more of the SAR energy out of the snowpack leaving little to interact with the snow mass and result in a significant reduction in volume reflection.

Analysis of Other Features of the Valley.

This section compares glaciological features that are identified on SAR images from 1996 and 1999. Four persistent features are noted: “veins, hook, and channeling” on Canada Glacier, and “ripples” near the top of the ablation area on Taylor Glacier. A SAR transect up the centerline on Taylor Glacier is compared to a Landsat 6 image. Finally a comparison between two Taylor Valley lakes shows a dramatic change in backscatter by season.

Persistent Features. Several persistent features are noted on Canada Glacier (veins, hook and channeling) and one on Taylor Glacier (ripples). There are veins of brighter backscatter extending along the axis of the glacier on the east side of Commonwealth Glacier (Table 7.4, Figure 7.17). Judging from other satellite-visible imagery, it appears that more snow has been blown onto the east side of the glacier (Figure 7.6), and indeed, helicopter over flights over the east neck corroborate this observation. The veins were not measured for depth or layering but like T13 and T14, they are likely at least 15 cm deep and have different density layers yielding enhanced volume backscatter.

Table 7.4: Comparison of SAR features.

	Veins (Figure 7.17)	Hook (Figure 7.17)	Channel (Figure 7.18)	Ripples (Figure 7.21)
2/1/1996 Radarsat	Three.	Faint.	Dense and very distinct.	Bright.
3/5/1996 ERS-1	One.	Faint.	Channeling not as apparent as 2/1/1996.	
10/23/1996 Radarsat	Three.	Visible.	Channeling is distinct.	Bright.
10/30/1996 ERS-2	Three.	Visible.	Dense and very distinct.	One ripple.
1/15/1999 ERS-2	Three.	Faint.		
1/19/1999 Radarsat ScanSAR	Indistinct.	Very faint.	Indistinct.	Bright.

The hook on Commonwealth Glacier is a radar feature that appears brighter in the early spring (October), and is barely visible in late summer and fall (January-March) (Table 7.4, Figure 7.17). Air photos taken November 1993 and Landsat in January 1993 show no visible signs of the hook (Figure 7.6). Three mass balance

stakes are within the hook area and data is available for 11/1993 and 1/1996. For 1/12/1996 snow depths range up to 8.5 cm, and 11/11/1996 a snow depths up to 4.0 cm (2/3 of the stakes without snow). Because the depths are so shallow, it is unlikely the hook has anything to do with a thin surface snow layer.

Canada Glacier has deep surface channels near its terminus that are radiometrically rough (Table 7.4, Figure 7.18). No channels are seen on the (c) and the (d) images. The 1/15/1999 image (c) is on the edge of the SAR scene. Because the incidence angle at the near edge is small (16-20°), both sides of the channel are close to being uniformly illuminated and are returning similar backscatter. When the incidence angle is larger, there is more differential SAR illumination of the sides of the channels (and perhaps some shadowing) and the backscatter difference effects a linear channel on the SAR image. A similar effect is happening with the channel in (d). This time the image is not near the edge of the image but the look direction is more perpendicular to the axis of the channels. The difference of illumination of the sides of the channels is small and they do not stand out in the image. Because of the look direction, the shadowing is also greater on the terminus cliff face to the northeast.

A very shallow but long flow-line depression is visible on the (b), (d) and (e) images. This depression does not show on the graphic representations of the DEM (probably due to its 30 m resolution), but the November 1993 air photo confirms its existence (Figure 7.19). On the (f) image this feature is not visible because of the

large pixel size. The fact that it is visible on three out of four of the (non-ScanSAR) images, testifies to the high vertical resolution of the SAR sensors.

The ripples on the upper Taylor Glacier (Figure 7.20) are persistent and are very similar year-to-year (Table 7.4, Figure 7.21). The original hypothesis was that the bright areas were snow accumulations drifted in persistent topographical patterns. Comparing the ripples to the Landsat image reveals only vague similarities to surface snow on the glacier. The lower, right side of the second, and middle of the third ripple corresponds with lines going across the glacier. The lines may be an abrupt slope change, but they do not appear in the contour lines derived from the DEM. The exact nature of what causes these ripples is unknown.

The terminus of Taylor Glacier is consistent in all the SAR images (Figure 7.22). The smooth ice surface specularly reflects the radar yielding a dark gray to black backscatter. The radiometrically rough terminus channels are visible in all the images.

Taylor Glacier Transect. I plotted a transect on the SAR image from the terminus of the Taylor Glacier following the centerline and into the East Antarctic Ice Sheet at the edge of the SAR image. The uncorrected Radarsat image was used because the corrected image did not include much of the upper Taylor due to the border being clipped to the DEM. Four regions are noted: the first three with flat linear trend lines (Figure 7.23). Comparing the SAR image with a Landsat 6 Satellite image (band 4) (Figure 7.20) reveals areas on the SAR image that are likely channels, and ice. The Landsat ice areas are dark to light gray in tone in the SAR image. Three

very bright (SAR) spikes on the graphed transect correspond to the (SAR) “ripples” mentioned previously. The Landsat image shows these areas to *generally* correspond to snowfields, but as mentioned previously detailed boundaries do not line up. The SAR backscatter in these snowfields (ripples) is much brighter than the snow zone further up the glacier. Because the area all through the snowfields is a very low slope ($<3^\circ$) there is no dominating aspect. The reason for the brighter backscatter in this area is unknown, but may have exceptionally efficient volume backscattering enhancement due to snow layering. The satellite image does not cover beyond 116 km on the transect, so the surface characteristics represented by “light dappled” and “dark dappled” areas are not known. The progressively darker backscatter along this upper transect, is consistent with Partington's (1998) SAR image of the highlands of Greenland. Perhaps the dappled areas are hard-packed sastrugi (sharp, irregular ridges formed on a snow surface by wind erosion and deposition) with specular reflection characteristics. Or they could be areas of exposed ice.

Lakes. A comparison of the lakes (Fryxell, and Bonney) in Taylor Valley showed no correlation with satellite polarization. There was, however, a seasonal change. In the austral spring, the lakes are very bright and even in tone; in the summer and fall they become darker and speckled in tone (Figure 7.24). This is likely due to changing melt water on the surface of the lake ice (Fritsen, 1998). The surface of the lake ice is very rough, reaching 1.5 m in amplitude. By January melt-pools fill the hollows with liquid water, slush, and thinly iced-over ponds. The liquid water on the surface of the lake ice is likely absorbing the radar beam and causing the lower

backscatter. Table 7.5 compares the brightness of Lakes Fryxell and Bonney to the nearest glacier ablation area. There is a small brightness difference in the summer and fall and a large difference in the spring.

$$ratio = \frac{glacier_brightness}{lake_brightness} \quad (7-3)$$

The numbers are ratios of an average of 10 random pixels of a lake and an average of 10 random pixels of a nearby glacier (Lake Fryxell used Commonwealth Glacier, and Lake Bonney used Taylor Glacier). Bold indicates data from austral spring.

Table 7.5: Brightness comparison of lake ice and nearby glacier ice.

	Lake Fryxell	Lake Bonney
10/23/1996	0.29	0.34
10/30/1996	0.32	0.22
2/1/1996	1.06	0.62
3/5/1996	0.71	0.80
1/19/1999	0.95	0.72

A comparison between average weekly (the week prior to the SAR image) air temperatures between the lakes and the nearest glacier metrological station strengthens the melt-pool hypothesis (Table 7.5). The air over the lakes is warmer than over the nearest glacier. In the austral fall there would be no liquid water on the glaciers or lakes. In the austral summer and fall, however, the temperatures indicate that lake surface ice melt is probable, and less likely on the glaciers. On both glaciers, the melt water is confined to the bottoms of some cryoconite holes and the bottoms of some large channels, both of which do not cover a large surface area. The temperatures for 3/5/1996 are low enough that any liquid water is unlikely, and the

Lake Fryxell image shows a medium backscatter (Figure 7.24). Perhaps there is still pooled water under a thin cap of ice on the lake ice surface and part of the SAR is penetrating the thin ice cap and being absorbed in the liquid water. Later in the year when this pooled water freezes, the backscatter maximizes reacting to the very rough lake ice surface.

Table 7.5: Average weekly temperature comparison between lake and glacier (°C).

	Austral spring		Austral summer and fall		
	10/23/1996	10/30/1996	1/19/1999	2/1/1996	3/5/1996
Lake Bonney	-22.3	-17.2	-1.9	1.0	-10.7
Taylor Glacier	-22.0	-19.0	-4.2	-1.6	-13.0
Lake Fryxell	-24.5	-19.6	-2.3	0.0	-12.1
Commonwealth Glacier	-23.1	-20.5	-5.2	-2.1	-11.7

Summary.

Glacier surfaces in Taylor Valley are generally radiometrically smooth and appear dark in the SAR image over most of the ablation zone. The snow zone images brighter because of the volume reflection from the entire depth of snow penetrated by the SAR beam. Because of the known penetration characteristics of SAR in dry snow, I expected a displacement of the SAR inferred snowline. In contrast, the SAR inferred and actual snowlines were very close to each other. This correspondence is due to enhanced volume reflection and can reveal the presence of snow depths of only 15 cm deep. Enhanced volume reflection results from layers of different densities acting as a specular reflective surfaces (Mätzler and Schanda, 1984; Tsang

et al., 1985; Ulaby et al., 1981). Reflection off internal layers increases the path length the beam travels (Ulaby et al., 1981), creates more opportunity to scatter in the snow, and increases total reflection. Therefore thin, dry snowpacks with no internal layers will not be visible in SAR imagery.

The corner reflectors worked very well, precisely locating the transect, adding scale, and two known points to the SAR image. The reflectors were placed on smooth glacial ice and the contrast of the dark backscatter of the ice to the brilliant reflection of the reflectors left no doubt to their locations on the image.

SAR can map snowlines in dry snow and be a useful instrument for tracking snowline changes over broad regions. Problems were encountered with a glacier sloping steeply away from the SAR platform, but that condition is readily visible on the image.

Curious and persistent features are compared in 1996 and 1999 SAR images. The Commonwealth Glacier “hook” (Figure 7.17) may be seasonal feature or fading from 1996, but is not visible in any other (non SAR) imagery. SAR imaging of the channeling at the terminus of Canada Glacier is not visible on one image because it is on the near edge of the SAR scene and the incidence angle is very high. This fact illustrates how detailed analysis must take into consideration the location of the SAR when the image is captured.

The time of year is another important consideration to interpreting SAR images. For instance the backscatter of lake surfaces varies dramatically by season. The lake surfaces are three times the minimum radiometric roughness determined in

equation 3-1. In the spring, when no liquid water exists on the lake ice, the rough surface backscatters brightly (Figure 7.24). Later in the year, melt on the surface of the lake ice and pools of liquid water develop on the lake surface (and near-surface). Despite the lake ice rough surfaces, the radar is absorbed and the backscatter is greatly reduced.

CHAPTER VIII

DISCUSSION AND CONCLUSIONS

Glacier surfaces in Taylor Valley are generally radiometrically smooth and appear dark in the SAR image over most of the ablation zone. The snow zone images are brighter because of the volume reflection from the entire depth of snow penetrated by the SAR beam. Researchers theorized that SAR penetrates dry snow to depths of one or more meters (Bindschadler et al., 1987; Bindschadler, 1998; Fahnestock et al., 1993; Forster et al., 1996; Jezek et al., 1993b; Lucchitta et al., 1995; Partington, 1998; Rott et al., 1993; Rott and Davis, 1993). Because of the predicted SAR penetration, the apparent location of the (SAR) snowline would be misplaced upslope compared to the actual position. Because of the spatial scale of the ice sheets, the comparatively small misplacement of the snowline is not considered. On the scale of small alpine glaciers ($\sim 5 \text{ km}^2$), however, misplacement of the snowline could be important. Surprisingly, the SAR inferred and actual snowlines on Commonwealth Glacier are very close to each other. This correspondence is likely due to enhanced volume reflection and can reveal the presence of snow depths of only 15 cm deep. Enhanced volume reflection results from layers of different

densities acting as a specular reflective surfaces (Mätzler and Schanda, 1984; Tsang et al., 1985; Ulaby et al., 1981). Reflection off internal layers increases the path length the beam travels (Ulaby et al., 1981), creates more opportunity to scatter in the snow, and increases total reflection. Therefore thin, dry snowpacks with no internal layers will not be visible in SAR imagery. This result indicates that the snowline may be detected with some certainty around the coastline of Antarctica as long as polar conditions are maintained.

Results from snowline mapping using SAR on Howard Glacier are inconsistent with the results from Commonwealth Glacier. The glacier only appeared on the Radarsat image because the ERS-2 scene did not cover that part of the valley. The aspect and slope of Howard Glacier faces away from the SAR beam at a sharp incident angle of about 10-23°. The entire glacier imaged dark with some tonal variation to indicate the transition from the snow to ice surfaces. The terrain correction degraded the resolution of the image sufficiently that it was nearly impossible to use. The steep slopes facing away from the SAR created both difficulties reassigning pixel locations in the terrain correction, and increased specular reflection on the snow layers limiting penetration, volume reflection, and displacing the snowline up-glacier. The uncorrected image was useful for making general interpretations, but the lack of geocoding makes precise analysis unreliable.

Howard Glacier illustrates the limitation of estimating snowline on steep slopes facing away from the sensor. In this case, imagery from another look direction or uncorrected analysis is required. Taking account of this limitation, SAR can map

snowlines in dry snow and be a useful instrument for tracking snowline changes over broad regions. Problems with glaciers sloping steeply away from the SAR platform are readily visible on the image.

Once an ELA is established using SAR, its variability can be measured over time and interpretations on changes on temperature and snowfall can be made. This information can be used to verify ice sheet models and GCMs as to their validity. Furthermore, the predictive aspects of GCMs would improve with a broader range of data around the entire coastline of Antarctica. Antarctica, because of its large size and low temperatures, it is one of the largest energy sinks on earth (Tzeng et al., 1993) and it plays a critical role in GCMs due to its significant influence on global climate. Questions about global warming and El Niño-Southern Oscillation could well come closer to a resolution with more complete ELA data from the Antarctic coastline.

Ice covered lakes in Taylor Valley early in the year, are radiometrically bright (Figure 7.25). Later in the year, they become difficult to discern (Lake Fryxell) using SAR. The lakes are very rough (>1 m) and well above the wavelength of the SAR (5.66 cm). In the austral spring, there is little or no meltwater in the surface cavities of the lake; however, later in the year substantial pools of water develop both in the cavities and just below thin layers of ice. I fell in one pool on Lake Hoare in January and measured it to be chest deep (1.5 m). This water is the likely cause of the seasonal change in backscatter, absorbing the radar and inhibiting backscatter (Hall, 1998).

The “hook” on Commonwealth Glacier, has only been identified on SAR imagery and is not reported in other investigations. It is brightest in the austral spring 1996 and fades in the fall. The hook is not visible in the January 6, 1993 Landsat 6 image, the November 1993 air photos, was not noted on helicopter over flights, nor noted while walking over the glacier surface. Because of lack of SAR imagery for the austral spring of 1999, it is not known if the hook is a SAR feature that is fading from 1996, or if it is a seasonal (austral spring) SAR feature. Further study of the persistence and causative surface properties of this feature is warranted.

Experiences and Recommendations.

The Terrcorr terrain correction program took months of work. I had problems formatting the DEM, setting the terrain correction program up in the computer, and understanding how to work the esoteric command language. However, once Terrcorr is set up and run once, the time it takes to run other SAR images are on the order of hours. For this study it was a benefit to have the data geolocated allowing detailed image pixel to glacier surface comparisons. The analysis of the SAR brightness with radiometric corrections gave the analysis a basis to the shape of the DEM and not simple radar backscatter from a geoid. Furthermore, for making maps with SAR, terrain correction is necessary to rectify the shape of the glacier to a map projection. For the analysis on Commonwealth Glacier it would have been a much lower detail and more ambiguous without the terrain correction. However, for change detection

analysis, if similar SAR look angles and orientations are used, and the orientation of the glacier is facing the SAR—terrain correction is not necessary.

I found the corner reflectors were very effective, brightly appearing against the dark background of the glacier ice on the SAR images. They provided known points on the SAR image, located the transect, and added scale. Without the corner reflectors, the detailed analysis of SAR brightness to snow measurement locations would have contained so much error to negate any conclusions. Corner reflectors are infrequently used as a ground reference in SAR analysis, however, they are relatively easy to construct and as little as two reflectors add two known points and scale to the SAR image, which was quite useful to this study.

Corner reflectors could be used on snow but they would be much more difficult to identify. If old SAR images are available, the reflectors could be placed where the image shows a dark region. A single reflector randomly placed in the snow zone would be lost in the brightness patterns.

Recommendation for Future Work.

This investigation answered some questions but it has also posed more. There are a number of things that could be further investigated:

- Define the snowline using a GPS and compare its location with a current SAR image.
- Compare the visible snowline from air photos or a Landsat image taken at same time as SAR data.

- Dig snow pits all along the snowline to compare SAR brightness to shallow snow depths.
- Make a seasonal analysis of the Commonwealth Glacier “hook” area to determine the glacier characteristics that create the unusual backscatter.
- Compare SAR imagery with other glaciers in the valley with a GPS snowline positions and snow stake data.
- Compare the SAR snowline on Taylor with a GPS track of the snowline.
- Convert the SAR data to decibels for more precise analysis of backscatter.
- Examine other glaciers along the Antarctic coastline for similar results to verify the practicality for large-scale snowline analysis.

As the dynamics of the interaction of radar with earth materials continues to be investigated, the uses for SAR will continue to expand. Its unique characteristics imaging through inclement weather and in darkness add practicality to this sensor for many locations on the earth. The possibility of mapping the snowline using SAR across large areas of Antarctic coastline offers a great volume of new data that could be used in GCMs. More accurate GCMs could answer the critical question of global warming and its impact on humanity. The future of SAR will undoubtedly bring smaller pixel sizes and multi-polarizations increasing resolution both spatially and in materials differentiation. The science of SAR is rapidly developing, giving cartographers, geographers, environmental scientists, and climatologists new perspectives to model and interpret the earth.

REFERENCES

- Achammer, T., and A. Denoth. "Snow Dielectric Properties: From DC to Microwave X Band." Annals of Glaciology. 19 (1994): 92-96.
- Alonso, Marcelo, and Edward J. Finn. Fundamental University Physics Volume 3: Fields and Waves. Massachusetts: Addison-Wesley Publishing Company, 1967.
- Akitaya, Eizi. "A Calorimeter for Measuring Free Water Content of Wet Snow." Annals of Glaciology. 6 (1985): 246-247.
- Avery, Thomas E., and Graydon L. Berlin. Fundamentals of Remote Sensing and Airphoto Interpretation. 5th ed. New York: Macmillian Publishing Company, 1992, pp 162-190.
- Benson, C. S. "Stratigraphic Studies in the Snow and Firn of the Greenland Ice Sheet." US Army Cold Regions Research and Engineering Laboratory RR 70. 1962.
- Bindschadler, Robert, A., K.C. Jezek, and J. Crawford. "Glaciological Investigations Using the Synthetic Aperture Radar Imaging System." Annals of Glaciology. 9(1987): 11-19.
- Bindschadler, Robert, A. "Monitoring Ice Sheet Behavior From Space." Reviews of Geophysics. 36 (1998): 79-104.
- Blom, R. G., R. E. Crippen, and C. Elachi. "Detection of Subsurface Features in Seasat Radar Images of Means Valley, Mojave Desert, California." Geology. 12(1984): 346-349.
- Budd, W. F., D. Janssen, E. Mavrakakis, and B. Coutts. "Modeling the Antarctic Ice-Sheet Changes Through Time." Annals of Glaciology. 20(1994): 291-297.
- Campbell, James B. Introduction to Remote Sensing. New York, NY: Guilford Press, 1996, pp157-237.
- Clow, Gary, D., C. McKay, G. Simmons, Jr., and R. Wharton, Jr. "Climatological

Observations and Predicted Sublimation Rates at Lake Hoare, Antarctica.”
Journal of Climate. July 1988: 715-728.

Conovitz, Peter A., Diane M. McKnight, Lee H. McDonald, Andrew G. Fountain, and Harold R. House. “Hydrologic Processes Influencing Streamflow Variation in Fryxell Basin, Antarctica.” *In* Prisco, John C., ed., Ecosystem Dynamics in a Polar Desert: The McMurdo Dry Valleys, Antarctica, Vol 72. Washington, D.C.: American Geophysical Union, 1998, pp 93-108.

Crowley, Thomas J. “Causes of Climate Change Over the Past 1000 Years.”
Science. 289(2000): 270-277.

Domik, Gitta, Franz Leberl and JoBea Cimino. "Multiple Incidence Angle SIR-B Experiment over Argentina: Generation of Secondary Image Products." IEEE Transactions on Geoscience and Remote Sensing. GE-24, 4(1986): 492-497.

Doran, Peter T., Gayle L. Dana, Jordan T. Hastings, and Robert A Wharton, Jr. “McMurdo LTER: LTER automatic weather network (LAWN).” Antarctic Journal of the United States. 1995.

Duda, R. O., and P. E. Hart. Pattern Classification and Scene Analysis. New York: Wiley, 1973.

Escher, M. C. Sky and Water 1. Haags Gemeentemuseum, The Hague, Netherlands, 1938.

Fahnestock, Mark, A., Robert A. Bindschadler, Ron Kwok, and Ken Jezek. “Greenland Ice Sheet Surface Properties and Ice Dynamics from ERS-1 SAR Imagery.” Science. 262 (1993): 1530-1534.

Fastook, James, L., and M. Prentice. “A Finite-Element Model of Antarctica: Sensitivity Test for Meteorological Mass-Balance Relationship.” Journal of Glaciology. 40, 134(1994): 167-175.

Forster, Richard, R., Curt H. Davis, Timothy W. Rand, and Richard K. Moore. “Snow-Stratification Investigation on an Antarctic Ice Stream with an X Band Radar System.” Journal of Glaciology. 37, 127(1991): 323-325.

Forster, Richard, R., Bryan L. Isacks, and Sarah B. Das. “Shuttle Imaging Radar (SIRC/X-SAR) Reveals Near-Surface Properties of the South Patagonian Icefield.” Journal of Geophysical Research. 101, E10(1996): 23,169-23,180.

Fountain, Andrew, G., Gayle L. Dana, Karen J. Lewis, Bruce H. Vaughn, and Diane M. McKnight. “Glaciers of the McMurdo Dry Valleys, Southern

- Victoria Land, Antarctica." *In* Priscu, John C., ed., Ecosystem Dynamics in a Polar Desert: The McMurdo Dry Valleys, Antarctica, Vol 72. Washington, D.C.: American Geophysical Union, 1998, pp 65-76.
- Fountain, Andrew, G., Berry Lyons, Melody B. Burkins, Gayle L. Dana, Peter T. Doran, Karen J. Lewis, Diane M. McKnight, Daryl L. Moorhead, Andrew N. Parsons, John C. Priscu, Dana H. Wall, Robert A. Wharton Jr., and Ross A. Virginia. "Physical Controls on the Taylor Valley Ecosystem, Antarctica." Bioscience. Vol. 49, 22(1999): 961-971.
- Fritsen, Christian, H., Edward E. Adams, Christopher P. McKay, and John C. Priscu. "Permanent Ice Covers of the McMurdo Dry Valleys Lakes, Antarctica: Liquid Water Contents." *In* Priscu, John C., ed., Ecosystem Dynamics in a Polar Desert: The McMurdo Dry Valleys, Antarctica, Vol 72. Washington, D.C.: American Geophysical Union, 1998, pp 65-76.
- Fuller, J. E., and E. S. Wampler. "The Lunar Laser Reflector." Scientific American. 222, 3(1970): 42.
- Glen, J. W., and J. G. Paren. "The Electrical Properties of Snow and Ice." Journal of Glaciology. 15, 73(1975): 15-38.
- Hall, Dorothy, K., Richard Williams, Jr., and Oddur Sigurdsson. "Glaciological Observations of Brúarjökull, Iceland, Using Synthetic Aperture Radar and Thematic Mapper Satellite Data." Annals of Glaciology. 21(1995): 271-276.
- Hall, Dorothy, K. "Remote Sensing of Snow and Ice Using Imaging Radar." *In* Floyd M. Henderson, and Anthony J. Lewis, eds., Principles and Applications of Imaging Radar, Manual of Remote Sensing, Vol 2. New York: John Wiley, 1998, pp 677-703.
- Harris, Colin M. "Science and Environmental Management in the McMurdo Dry Valleys, Southern Victoria Land, Antarctica." *In* Priscu, John C., ed., Ecosystem Dynamics in a Polar Desert: The McMurdo Dry Valleys, Antarctica, Vol 72. Washington, D.C.: American Geophysical Union, 1998, pp 337-350.
- Jezek, K. C., M. Drinkwater, J. Crawford, R. Bindschadler, and R. Kwok. "Analysis of Synthetic Aperture Radar Data Collected Over the Southwestern Greenland Ice Sheet." Journal of Glaciology. 39(1993): 119-131.
- Keys, J. R. Air Temperature, Wind, Precipitation and Atmospheric Humidity in the McMurdo Region. Publication 17. Wellington, New Zealand: Victoria

University of Wellington, 1980.

- Krinner, Gerhard, and Christophe Genthon. "The Antarctic Surface Mass Balance in a Stretched Grid General Circulation Model." Annals of Glaciology. 25(1997): 73-78.
- Lewis, K.J., Fountain, A.G., and Dana, G.L. "McMurdo LTER: The surface-energy balance of the Canada Glacier, Taylor Valley." Antarctic Journal of the United States. 1995.
- Lide, David R., ed. CRC Handbook of Chemistry and Physics, 80th ed. Washington D.C.: CRC Press, 1999.
- Lillesand, Thomas M., and Ralph W. Kiefer. Remote Sensing and Image Interpretation. 3rd ed. New York: John Wiley and Sons, Inc., 1994, pp 660-662.
- Liston, Glen, E., Jan-Gunnar Winther, Oddbjørn Bruland, Hallgeir Elvehøy, and Kunt Sand. "Below-Surface Ice Melt on the Costal Antarctic Ice Sheet." Journal of Glaciology. 45(1999): 273-285.
- Lucchitta, B.K., C.E. Rosanova, and K.F. Mullins. "Velocities of Pine Island Glacier, West Antarctica, From ERS-1 SAR Images." Annals of Glaciology. 21(1995): 277-282.
- Marsiat, I. "Ice Sheets' Surface Mass-Balance Evaluation in the UGAMP GCM: the Climate of Antarctica." Annals of Glaciology. 23(1996): 167-173.
- Mätzler, C., and Erwin Schanda. "Snow Mapping with Active Microwave Sensors." International Journal of Remote Sensing. 5, 2(1984): 409-422.
- Mätzler, C. "Applications of the Interaction of Microwaves with the Natural Snow Cover." Remote Sensing Review. 2(1987): 259-387.
- McCauley, J. F., G. G. Schaber, C. S. Breed, M. J. Grolier, C. V. Haynes, B. Issawi, C. Elachi, and R. Blom. "Subsurface Valleys and Geoarchaeology of the Eastern Sahara Revealed by Shuttle Radar." Science. 218(1982): 1004-1019.
- Moorhead, Daryl L., and John C. Prisco. "The McMurdo Dry Valley Ecosystem: Organization, Controls, and Linkages." In Prisco, John C., ed., Ecosystem Dynamics in a Polar Desert: The McMurdo Dry Valleys, Antarctica, Vol 72. Washington, D.C.: American Geophysical Union, 1998, pp 351-364.
- Muhleman, Duane, O., Arie W. Grossman, and Bryan J. Butler. "Radar

- Investigations of Mars, Mercury, and Titan.” *In* Wetherill, George W., Arden L. Albee, and Kevin C. Burke, eds., Annual Review of Earth and Planetary Sciences Volume 23. Palo Alto: Annual Reviews Inc., 1995, pp 337-374.
- Müller, Fritz. “Zonation in the Accumulation Area of the Glaciers of Axel Heiberg Island, N.W.T., Canada.” Journal of Glaciology. 4(1962): 302-313.
- Naraghi, Manouher, William Stromberg, and Mike Daily. "Geometric Rectification of Radar Imagery Using Digital Elevation Models." Photogrammetric Engineering and Remote Sensing. 49,2(1983): 195-199.
- Oerlemans, Johannes, and Alfred Wegener. “A Projection of Future Sea Level.” Climatic Change. 15(1989): 151-174.
- Oerlemans, Johannes, and J. P. F. Fortuin. “Sensitivity of Glaciers and Small Ice Caps to Greenhouse Warming.” Science. 258(1992): 115-117.
- O’Farrell, Siobhan, P., J. McGregor, L. Rotstayn, W. Budd, C. Zweck, and R. Warner. “Impact of Transient Increases in Atmospheric CO₂ on the Accumulation and Mass Balance of the Antarctic Ice Sheet.” Annals of Glaciology. 25(1997): 137-144.
- Ohmura, Atsumu, Martin Wild, and Lennart Bengtsson. “Present and Future Mass Balance of the Ice Sheets Simulated With GCM.” Annals of Glaciology. 23(1996): 187-193.
- Olmsted, Coert. Alaska SAR Facility Scientific SAR User's Guide. Available at: <http://www.alaska.edu> (accessed 2/1/00). ASF-SD-003(1993).
- Patterson, W. S. B. The Physics of Glaciers. 3rd ed. Trowbridge, Great Britain: Redwood Books, 1994.
- Parish, Thomas R., and David H. Bromwich. “The Surface Windfields Over the Antarctic Ice Sheets.” Nature. 328(1987) 51-54.
- Partington, K. C. “Discrimination of glacier facies using multi-temporal SAR data.” Journal of Glaciology. 44(1998): 42-53.
- Raney, Keith R. “Radar Fundamentals: Technical Perspective.” *In* Henderson, Floyd M., and Anthony J. Lewis, ed., Manual of Remote Sensing 3rd Edition: Principles and Applications of Imaging Radar, Vol 2. New York: American Society for Photogrammetry and Remote Sensing, 1998, pp 9-130.

- Rott, Helmut, and C. Mätzler. "Possibilities and Limits of Synthetic Aperture Radar for Snow and Glacier Surveying." Annals of Glaciology. 9 (1987): 195-199.
- Rott, Helmut, Klaus Strum, and Heinz Miller. "Active and Passive Microwave Signatures of Antarctic Firn by Means of Field Measurements and Satellite Data." Annals of Glaciology. 17(1993): 337-342.
- Rott, Helmut, and Robert E. Davis. "Multifrequency and Polarimetric SAR Observations on Alpine Glaciers." Annals of Glaciology. 17(1993): 98-104.
- Sarachik, Edward S., McGraw-Hill Encyclopedia of Science and Technology #5 8th Edition. New York: McGraw-Hill, 1997.
- Schlatter, Thomas W. "The local Surface Energy Balance and Subsurface Temperature Regime in Antarctica." Journal of Applied Meteorology. 11 (1972): 1048-1062.
- Short, Nicholas M., and Robert W. Blair, Jr., ed. Geomorphology From Space. Washington: NASA Scientific and Technical Branch, 1986.
- Shi, Jiancheng, and Jeff Dozier. "Measurements of Snow and Glacier-Covered Area With Single Polarization Synthetic Aperture Radar." Annals of Glaciology. 17 (1993): 72-76.
- Smith, Laurence, C., Richard R. Forster, Bryan L. Isacks, and Dorothy K. Hall. "Seasonal Climatic Forcing of Alpine Glaciers Revealed With Orbital Synthetic Aperture Radar." Journal of Glaciology. 43(1997): 480-488.
- Trevett, J. W. Imaging Radar for Resource Surveys. Cambridge, Massachusetts: Chapman and Hall, 1986.
- Tsang, Leung, Jin A. Kong, and Robert T. Shin. Theory of Microwave Remote Sensing. New York: John Wiley and Sons, 1985.
- Tzeng, Ren-Yow, David H. Bromwich, and Thomas R. Parish. "Present-Day Antarctic Climatology of the NCAR Community Climate Model Version 1." Journal of Climate 6(1993): 205-226.
- Ulaby, Fawwaz, T., Richard K. Moore, and Adrian K. Fung. Microwave Remote Sensing: Active and Passive Volumes 1-3. Reading, Massachusetts: Addison-Westley Publishing Co., 1981.
- Van De Wal, R. S. W. "Mass-Balance Modelling of the Greenland Ice Sheet: a Comparison of an Energy-Balance and a Degree-Day Model." Annals of Glaciology. 23(1996): 36-45.

- Verbitsky, Mikhail, and Barry Saltzman. "Behavior of the East Antarctic Ice Sheet as Deduced From a Coupled GCM/Ice-Sheet Model." Geophysical Research Letters. 22, 21(1995): 2913-2916.
- Watson, Robert T., M. C. Zinyowera, R. H. Moss, R. A. Moreno, et al. "Technical Summary: Impacts, Adaptations, and Mitigation Options. *In* Watson, Robert T., Marufu C. Zinyowera, Richard H. Moss, David J. Dokken (project administrator), eds., Climate Change, 1995: Impacts, Adaptations and Mitigation of Climate Change: Scientific-Technical Analyses: Contribution of Working Group II to the 2nd Assessment Report of the Intergovernmental Panel on Climate Change. NY: Cambridge University Press, 1996, pp 19-53.
- Wharton, Robert A. Jr., Christopher P. McKay, George M. Simmons Jr., and Bruce C. Parker. "Cryoconite Holes on Glaciers." Bioscience 35,8(1985): 499-503.

Websites

- Canadian Space Agency (RADARSAT), available at <http://radarsat.space.gc.ca/>;
Internet; accessed January 27, 2000.
- European Space Agency (ERS-1 & 2), available at <http://www.esrin.esa.it/>;
Internet; accessed 6 October 1998.
- Japanese Space Agency (JERS-1), http://yyy.tksc.nasda.go.jp/Home/This/This_e/jers_e.html; Internet; accessed 24 October 1998.
- Jet Propulsion Laboratory (JPL) Imaging Radar, <http://southport.jpl.nasa.gov/>;
accessed 30 January 2000.
- Alaska SAR Facility (ASF), <http://www.asf.alaska.edu>; accessed 5 October 2000.
- McMurdo Dry Valleys Long-Term Ecological Research,
<http://www.nsf.gov/od/opp/antarct/ajus/nsf9828/9828html/h1.htm>; accessed
5 October 2000.
- INSTAAR MCM Long-Term Ecological Research
<http://huey.colorado.edu/LTER/>; accessed 10 November 2000.

Appendix A

McMurdo Dry Valley Snow Pit Data for Commonwealth and Howard Glaciers.

Commonwealth Glacier

Stake 11

20-Jan-99

Layer	Thickness cm	Total Mass g	Mass of Bag g	Snow Mass g	Density g/cm ³	Weighted Density g/cm ²	
I	1				0.15		
	Note:	Use stake 13 surface density					

Stake 12

20Jan99

Layer	Thickness cm	Total Mass g	Mass of Bag g	Snow Mass g	Density g/cm ³	Weighted Density g/cm ²
I	2		0			
II	8	23		23	0.23	1.84
III	5	36		36	0.36	1.8
IV	8	24		24	0.24	1.92
V	6	31		31	0.31	1.86
sum	27					7.42
		average snowpack density			0.27	

Layer	hardness	crystal	size
I	1 finger	wind crust	1
II	4 finger	facets	2
III	pencil	rounds	1
IV	4 finger pencil	facets facets/rounds	2-3 3
Below 0: Glacier ice			

Stake 13

19Jan99

Layer	Thickness Cm	Total Mass g	Mass of Bag g	Snow Mass g	Density g/cm ³	Weighted Density g/cm ²
I	3.5	15	0	15	0.15	0.525
II	7	40	0	40	0.4	2.8
III	7.5	36	0	36	0.36	2.7
IV	12	24	0	24	0.24	2.88
sum	30					8.905
		average snowpack density			0.29	

<u>Layer</u>	<u>hardness</u>	<u>crystal</u>	<u>size</u>
I	fist	broken stellars	1
II	1 finger	round	1
III	pencil	rounds	1-1.5
IV	4 finger	facets	2
Below 0: Hard snow			

Stake 14
20Jan99

<u>Layer</u>	<u>Thickness</u>	<u>Total</u>	<u>Mass</u>	<u>Snow</u>	<u>Density</u>	<u>Weighted</u>
	<u>cm</u>	<u>Mass</u>	<u>of Bag</u>	<u>Mass</u>	<u>g/cm3</u>	<u>Density</u>
		<u>g</u>	<u>g</u>	<u>g</u>		<u>g/cm2</u>
I	1					
II	8	29	0	29	0.29	2.32
III	7	45	0	45	0.45	3.15
IV	26	30	0	30	0.3	7.8
V	24	19	0	19	0.19	4.56
Sum	66					17.83
average snowpack density:					0.27	

<u>Layer</u>	<u>hardness</u>	<u>crystal</u>	<u>size</u>
I	wind crust		1
II	1 finger	rounds	1.5
III	knife	rounds	1
IV	pencil	facets/rounds	3
V	1 finger	honeycomb	3-10
--ice--	Below 0: Glacier ice		

Stake 15
20Jan99

<u>Layer</u>	<u>Thickness</u>	<u>Total</u>	<u>Mass</u>	<u>Snow</u>	<u>Density</u>	<u>Weighted</u>
	<u>cm</u>	<u>Mass</u>	<u>of Bag</u>	<u>Mass</u>	<u>g/cm3</u>	<u>Density</u>
		<u>g</u>	<u>g</u>	<u>g</u>		<u>g/cm2</u>
I	33.5	25	0	25	0.25	8.375
II	10.5	33		33	0.33	3.465
III	9	25		25	0.25	2.25
IV	1					
V	10	19		19	0.19	1.9
sum	63					15.99
average snowpack density:					0.25	

<u>Layer</u>	<u>hardness</u>	<u>crystal</u>	<u>size</u>
I	4 finger	rounds	1
II	1 finger	rounds	1
III	4 finger	facets/rounds	2
IV		wind crust/ facets	
V	4 finger	facets	2
Below 0: Hard dirty snow			

Stake 16
20Jan99

Layer	Thickness cm	Total Mass g	Mass of Bag g	Snow Mass g	Density g/cm ³	Weighted Density g/cm ²	
I	3	22	0	22	0.22	0.66	
II	9	44		44	0.44	3.96	
III	2	22		22	0.22	0.44	
IV	8	42		42	0.42	3.36	
V	12	27		27	0.27	3.24	
VI	16	32		32	0.32	5.12	
Sum	50					16.78	
		average snowpack density:			0.33		

Layer	hardness	crystal	size
I	fist	broken stellar	1.5
II	pencil	rounds	1
III	1 finger	facets/rounds	2
IV	1 finger	rounds	1
V	fist	facets/rounds	2.5
VI	4 finger	rounds	2

Below 0: Hard layer

Stake 17
20Jan99

Layer	Thickness cm	Total Mass g	Mass of Bag g	Snow Mass g	Density g/cm ³	Weighted Density g/cm ²	
I	4	25		25	0.25	1	
II	8	24		24	0.24	1.92	
III	1				0.22	0.22	
IV	3	19		19	0.19	0.57	
V	7	20		20	0.2	1.4	
VI	19	35		35	0.35	6.65	
VII							
VIII	11	16		16	0.16	1.76	
Sum	53					13.52	
		average snowpack density:			0.25		

Layer	hardness	crystal	size
I	fist	rounds/facets	2
II		crust/rounds	1
III	fist	facets/rounds	2
IV	4 finger	facets/rounds	2
V	1 finger	honeycomb	2-3
VI	1 mm ice lens		
VII	1 finger	honeycomb	3-6

Below 0: Hard dirty layer

Stake 18
19Jan99

Layer	Thickness cm	Total Mass g	Mass of Bag g	Snow Mass g	Density g/cm ³	Weighted Density g/cm ²	
I	3.4	19	0	19	0.19	0.64	
II	18.2	50		50	0.5	9.1	
III	18	33		33	0.33	5.94	
IV	1	33		33	0.33	0.33	
V	15	29		29	0.29	4.35	
sum	55.6					20.36	
		average snowpack density:			0.36		

Layer	hardness	crystal	size
I	fist	broken stellars	1
II	knife	rounds	0.5
III	4 finger	rounds and facets	2
IV	1 finger	rounds	1
V	4 finger	rounds and facets	1-2

Below 0: Hard layer

Stake 19
19Jan99

Layer	Thickness cm	Total Mass g	Mass of Bag g	Snow Mass g	Density g/cm ³	Weighted Density g/cm ²	
I	4.6	15	0	15	0.15	0.69	
II	7	34		34	0.34	2.38	
III	29.8	29		29	0.29	8.642	
IV	1	33		33	0.33	0.33	
V	16	26		26	0.26	4.16	
VI	10	32		32	0.32	3.2	
Sum	68.4					19.40	
		average snowpack density:			0.28		

Layer	hardness	crystal	size
I	fist	broken stellars	.5-1.0
II	1 finger	rounds	1
III	fist	facets	2
IV	1 finger	rounds	0.5-1
V	4 finger	facets - rounds	2
VI	1 finger	rounds	1

Below 0: Hard layer

Stake 20
36161

Layer	Thickness cm	Total Mass g	Mass of Bag g	Snow Mass g	Density g/cm ³	Weighted Density g/cm ²	
I	7.8	18	0	18	0.18	1.404	
II	8.5	35		35	0.35	2.975	
III	4.5	22		22	0.22	0.99	
IV	10	31		31	0.31	3.1	
V	4.5	20		20	0.2	0.9	
VI	2	29		29	0.29	0.58	
VII	3	26		26	0.26	0.78	
VIII	7	27		27	0.27	1.89	
sum	47.3					12.61	
		average snowpack density			0.26		

Layer	hardness	crystal	size
I	fist	broken stellars	0.5-1
II	1 finger	rounds	1.5
III	fist	facets	2-3
IV	1 finger	rounds	1
V	fist	facets-rounds	2-3
VI	1 finger	rounds	1
VII	4 finger	rounds-facets	2
VIII	1 finger	rounds	1-2

Below 0: Hard Layer

Stake 21
19Jan99

Layer	Thickness cm	Total Mass g	Mass of Bag g	Snow Mass g	Density g/cm ³	Weighted Density g/cm ²	
I	3.6	14	0	14	0.14	0.504	
II	22.6	52		52	0.52	11.752	
III	5	27		27	0.27	1.35	
IV	5.7	34		34	0.34	1.938	
V	4.3	19		19	0.19	0.817	
VI	10	23		23	0.23	2.3	
sum	51.2					18.66	
		average snowpack density			0.36		

Layer	hardness	crystal	size
I	fist	broken stellar	.5-1
II	pencil	rounds	0.5
III	4 finger	facets	1-2
IV	1 finger	rounds	2
V	4 finger	facets - rounds	2-3
VI	1 finger	rounds some facets	1

Below 0: Hard layer

Stake 22
19Jan99

Layer	Thickness cm	Total Mass g	Mass of Bag g	Snow Mass g	Density g/cm ³	Weighted Density g/cm ²
I	9.3	15	0	15	0.15	1.395
II	14.1	32		32	0.32	4.512
III	17.2	27		27	0.27	4.644
sum	40.6					10.55

average snowpack density 0.25

Layer	hardness	crystal	size
I	fist	broken stellars	.5-1
II	1 finger	rounds	1
III	4 finger	facets-rounds	2

Below 0: Hard layer

Stake 23
19Jan99

Layer	Thickness cm	Total Mass g	Mass of Bag g	Snow Mass g	Density g/cm ³	Weighted Density g/cm ²
I	2.5	33	0	33	0.33	0.825
II	3	17		17	0.17	0.51
III	7	30		30	0.3	2.1
IV	11	41		41	0.41	4.51
V	14	26		26	0.26	3.64
sum	37.5					11.58

average snowpack density 0.30

Layer	hardness	crystal	size
I	1 finger	broken stellars.	Light wind crust 0.5-1
II	4 finger	broken stellars.	1
III	1 finger	facets, rounds	1
IV	pencil	rounds	1-2
V	4 finger	facets, rounds	2

Below 0: Hard layer

Howard Glacier
Stake 24
21Jan99

Layer	Thickness cm	Total Mass g	Mass of Bag g	Snow Mass g	Density g/cm ³	Weighted Density g/cm ²
I	1	20	0	20	0.20	0.20
sum	1				0.20	

snowpack density 0.20

Stake 25
21Jan99

Layer	Thickness cm	Total Mass g	Mass of Bag g	Snow Mass g	Density g/cm ³	Weighted Density g/cm ²
I	2	20	0	20	0.20	0.40
II	4.7	56		56	0.56	2.63
III	5.5	30		30	0.30	1.65
IV	12	42		42	0.42	5.04
V	4.9	35		35	0.35	1.72
sum	29.1				11.44	
	average density:		0.39			

Stake 26
21Jan99

Layer	Thickness cm	Total Mass g	Mass of Bag g	Snow Mass g	Density g/cm ³	Weighted Density g/cm ²
I	5	16	0	16	0.16	0.80
II	4.4	40		40	0.40	1.76
sum	9.4				2.56	
	average density:		0.27			

Stake 27
21Jan99

Layer	Thickness cm	Total Mass g	Mass of Bag g	Snow Mass g	Density g/cm ³	Weighted Density g/cm ²
I	4	20	0	20	0.20	

Stake 28
21Jan99

Layer	Thickness cm	Total Mass g	Mass of Bag g	Snow Mass g	Density g/cm ³	Weighted Density g/cm ²
I	4	20	0	20	0.20	

Stake 30
21Jan99

Layer	Thickness cm	Total Mass g	Mass of Bag g	Snow Mass g	Density g/cm ³	Weighted Density g/cm ²
I	4	20	0	20	0.20	

Stake 31
21Jan99

Layer	Thickness cm	Total Mass g	Mass of Bag g	Snow Mass g	Density g/cm ³	Weighted Density g/cm ²
I	4	20	0	20	0.20	

Between Stakes 29,30,66
21Jan99

Layer	Thickness cm	Total Mass g	Mass of Bag g	Snow Mass g	Density g/cm ³	Weighted Density g/cm ²
I	2.5	19	0	19	0.19	0.48
II	7	45		45	0.45	3.15
III	7	32		32	0.32	2.24
sum	16.5				5.87	
		snowpack density		0.36		

Stake 66
1/21/1999

Layer	Thickness cm	Total Mass g	Mass of Bag g	Snow Mass g	Density g/cm ³	Weighted Density g/cm ²
I	2.5	20	0	20	0.20	0.50
sum	2.5				0.5	
		average density:		0.20		

Appendix B

Transect Field Data For Commonwealth and Howard Glacier.

Commonwealth Glacier.

Sample sites marked with a “(C)” are from the first transect run on 1/19&20/99. The distances between each site was "chained out" using a 50 m climbing rope. Sample sites with a “(G)” are from the second transect run on 1/26/99. The distances between each site was determined using hand held GPS. The course of the second transect followed the footprints in snow from earlier transect. The thermometer read +0.4 high (calibrated with slushy water at camp) and the temperatures listed are not adjusted for this error.

T1 (C) Lower Reflector

Bright sun, clear skies

Aspect SE

Slope 2-5 degrees used ice axe and Brunton compass

Snow temp -1.7 C

Ice temp -1.8, -0.5 C

Cryoconite temp +0.8 C (water?)

Air temp -2.6 C

Snow table depth 4, 17, 21, 9 cm

Thin snow over ice 4, 1, 3, 2, 1.5 cm

Ice roughness parallel to beam (cm)

4.5	4.0	2.8	3.0	2.1	2.5	2.9	1.6
2.7	2.5	3.6	3.4	3.8	4.0	1.3	3.0
2.9	5.2	2.8	3.9	4.6	3.0	4.5	3.7
3.3	3.5	4.7	5.0	6.0	6.0	3.0	3.6
3.3	3.3	3.1	1.0	1.8	2.9	4.3	2.9
3.8		Ave 3.4					

Ice roughness perpendicular to the beam (cm)

5.8	2.8	2.9	2.9	1.5	5.4	4.0	7.5
1.7	4.4	2.9	3.4	3.8	3.1	2.7	3.6
3.4	3.6	3.4	3.5	2.5	2.8	4.1	4.3
4.3	3.1	3.1	1.9	2.8	2.0	2.0	3.3
3.5	3.8	3.7	2.5	3.2	3.4	3.4	3.3
3.6		Ave 3.3					

Rough old snow/ice with new snow tables 30 cm high

exposed cryoconite holes 30-90 cm wide

Cryoconite hole depths 21, 26, 12, 18, 18, 28, 7, 12, 12, 12, 7, 17

Snow pit 16 cm deep dug on a snow table

layer	depth (cm)	mass (g)	crystal size (mm)	hardness (measured by inserting an object into the snow layer).
I	12-16	40	1 mm	knife
II	11-12			softer
III	0-11	27	1 facets	four fingers

T1 (G) Lower Reflector "Karl" Jan 26, 1999

According to GPS 2.35 km from MARTHA

The area around each site was characterized: relative aerial fractions of type of surface (snow, ice) and any notable features (e.g. crevasse, cryoconite holes). The fractional area of cover (e.g. snow, ice, cryoconite holes) was established by a consensus of estimates between the field data collectors.

Ice	75%
Snow table	10%
Thin snow	15%
Cryoconite	5-10%

Ice roughness parallel to beam (cm)

2.4	1.4	1.4	1.7	1.2	2.4	1.4	3.0
1.1	2.2	3.4	2.9	4.4	3.8	4.0	3.6
2.3	1.8	4.0	4.0	4.5	5.3	3.8	2.1
2.4	2.3	3.6	10.9	11.2	11.0	9.2	5.6
4.7	3.2	3.3	3.5	0.8	4.7	4.2	4.5
5.3		Ave 3.8					

Ice roughness perpendicular to the beam (cm)

5.2	3.9	2.3	1.8	2.7	1.6	1.5	3.6
4.4	3.7	1.2	2.8	1.8	2.6	5.4	5.5
9.4	9.1	9.7	2.8	2.2	1.7	1.6	1.9
0.5	6.7	4.6	3.6	2.2	1.2	2.1	2.3
1.9	3.0	5.6	8.7	6.7	6.4	5.0	6.4
3.5		Ave 3.8					

T2 (C)

Aspect SE

Slope 0, 3, 3, 2 degrees

Snow temp -1.9, -1.7, -1.3 C

Ice temp +0.5, +0.7, +0.6 C (water?)

Snow table depth 7.4, 14.8, 19 cm

Thin snow over ice 2.5, 4.8, 1.5 cm

Snow tables similar to stratigraphy to site #1

15% exposed ice

Suncups facing north like T1, 4-5 cm deep, fewer open cryoconite holes, small cracks SE-NE, and 8cm deep 20 cm wide max to 0.

T2 (G)

GPS 2.10 km from MARTHA (change=250 m)

Ice 85%

Snow table 10%

Thin snow 5%

Cryoconite 5%

Ice roughness parallel to beam (cm)

1.7	1.9	4.9	2.6	2.5	2.3	1.2	1.5
3.1	2.3	2.5	2.4	2.4	2.6	2.2	4.4
4.8	5.6	3.5	3.5	2.0	2.7	3.4	2.7
1.6	1.2	3.8	2.1	2.0	2.0	1.8	2.3
1.8	3.5	3.9	2.4	2.9	2.6	1.9	1.5
1.8		Ave 2.6					

Ice roughness perpendicular to the beam (cm)

1.7	1.8	1.4	2.6	3.8	2.4	2.2	2.8
2.0	1.7	1.8	1.9	3.0	2.8	3.9	5.3
4.3	3.0	3.4	3.1	2.4	1.5	1.1	1.1
1.5	2.3	7.8	3.0	2.5	2.4	1.4	1.0
2.0	3.6	3.6	4.4	5.5	4.0	3.2	2.3
1.8		Ave 2.7					

T3 (C) about 200 m SSW of Metrological station

Aspect SE

Slope 0, 2, 0 degrees

Snow temp -0.9 (near surface), 3.0 (2 cm deep, water?)

Ice temp -0.6, +0.6 C (water?)

Snow table depth 26, 25, 16, 16

Thin snow over ice 2.2, 2.8, 1.0, 2.5

Ice roughness parallel to beam (cm)

8.5	8.5	5.0	5.0	2.8	2.8	1.7	3.4
3.0	6.2	3.0	3.6	3.1	1.5	3.3	3.8
4.7	2.6	1.7	1.7	4.9	2.8	2.3	5.2
1.9	1.5	2.0	4.0	2.3	4.4	5.4	2.8
6.6	5.3	4.1	5.9	5.9	4.2	2.5	2.6
1.6	2.0		Ave 3.7				

Ice roughness perpendicular to beam (cm)

6.9	6.9	5.9	7.5	7.2	5.0	6.7	4.3
7.4	4.6	3.0	4.2	6.5	6.0	5.4	5.2
7.0	6.0	1.9	1.1	6.2	5.5	15.2	7.3
8.0	8.0	7.1	13.8	5.1	3.0	4.4	2.8
2.8	11.0	3.2	2.6	1.6	1.5	5.6	2.5

1.4 (occasionally in cryoconite hole) Ave 5.5

Some cryoconite holes depth 12, 5, 17, 7 cm, diameter 9-100 cm.

Exposed ice 25%
 Snow tables 50%
 Thin snow over ice 25%

T4 (C)

Aspect SE

Slope 4, 3

Snow temp -0.4, -2.0, -2.3

Ice temp +3.0 (water?), -2.1 (under snow), +0.5 (water?)

Snow table depth 19, 20, 19, 13

Thin snow over ice 2, 1.8, 3.6, 3.8

Snow tables 40%

Exposed ice 25%

Thin snow over ice 35%

Few obvious cryoconite holes, could be snow covered

T4 (G)

GPS 1.67 km from MARTHA (change=500 m)

Across from met station, just a bit downhill

Ice 35%
 Snow table 30%
 Thin snow 35%
 Cryoconite 0%

Ice roughness parallel to beam (cm)

1.0	1.4	1.7	1.4	1.7	2.1	3.4	4.4
4.3	6.0	5.5	6.1	5.9	3.0	4.6	4.3
3.9	4.8	4.2	4.5	4.0	5.2	4.1	5.0
3.4	2.3	1.9	1.2	1.0	1.9	2.9	3.7
5.2	5.5	4.6	4.0	3.9	4.4	4.9	5.9
5.8		Ave	3.7				

Ice roughness perpendicular to beam (cm)

2.6	1.9	1.0	1.5	3.9	3.3	2.5	2.5
3.7	3.1	2.4	2.1	1.5	1.3	1.6	2.4
2.5	2.0	1.1	1.4	1.8	1.4	1.5	2.5
2.4	2.8	2.8	3.0	2.8	3.7	3.0	2.0
2.3	2.7	2.6	1.9	1.5	2.3	2.9	2.6
1.3		Ave	2.2				

T5 (C)

Aspect SE

Slope 5, 3

Snow temp -1.7

Ice temp +0.3 (water?)

Snow table depth 20, 25, 30, 24

Thin snow over ice 6.3, 4.2, 3.8, 5.4

Ice roughness parallel to beam (cm)

2.7	1.3	1.3	1.7	1.9	1.5	1.4	1.1
1.4	1.4	1.5	1.7	2.1	1.9	1.8	2.8
1.6	1.1	1.5	1.8	2.1	3.8	6.5	7.2
7.0	5.8	4.7	5.1	2.4	2.7	2.8	3.2
3.1	2.4	3.2	2.5	1.8	4.1	2.6	2.4
2.4		Ave	2.7				

Ice roughness perpendicular to beam (cm)

1.0	1.8	2.8	2.4	3.7	1.4	1.6	1.9
2.9	3.2	3.2	1.6	3.0	4.8	7.0	8.0
7.9	8.3	7.7	8.2	7.2	5.9	2.9	3.4
4.2	4.0	1.6	1.6	1.3	2.9	3.0	3.6
1.9	2.0	2.7	2.7	2.0	1.6	1.2	2.3
1.2		Ave	3.4				

Snow pit 8 cm deep two layers

layer depth mass crystal size hardness

	(cm)	(g)	(mm)	
I	6-8	27	windblown	knife
II	0-6	37	1.0 hoar	fist

Snow tables 25%
Exposed ice 10%
Thin snow over ice 65%

Some cryoconite holes, crevasses 7cm wide and along transect.

T6 (C)
Aspect WSW
Slope 0, 4
Snow table depth 22, 21, 9, 30
Thin snow over ice 1.8, 6.0, 2.8, 3.0

Snow tables 15%
Exposed ice 10%
Thin snow cover 75%
Hummocky snow, little ice exposed
Cryoconite holes evident

T6 (G)
GPS 1.17 km from MARTHA (change 500 m)
Ice 75%
Snow table 15%
Thin snow 10%
Cryoconite 5-10%

Ice roughness parallel to beam (cm)

1.4	1.0	1.2	1.9	2.7	2.4	3.8	3.3
2.5	1.7	1.0	2.9	3.5	2.7	2.6	2.1
1.7	1.8	1.3	1.1	1.4	2.2	2.4	2.0
1.9	2.3	3.3	2.4	2.7	1.4	2.7	2.7
1.8	2.5	4.4	4.6	3.9	1.7	1.5	1.9
1.3		Ave 2.2					

Ice roughness perpendicular to beam (cm)

1.3	1.8	1.9	1.9	2.1	2.5	3.2	3.1
3.5	2.6	1.6	2.5	3.2	2.8	2.7	2.7
1.9	1.4	2.3	2.9	3.1	2.5	2.9	3.2
3.9	3.5	2.3	2.8	3.6	3.6	2.6	2.3
2.9	3.2	3.0	2.9	3.7	3.0	2.3	2.5
2.3		Ave 2.6					

T6 SECOND DAY, second entry

Jan 20, 1999 10:30

Overcast no new snow since yesterday, surface remains same.

Air temp -0.9

Snow temp -2.8, -2.3, -3.7

Ice temp -3.5

T7 (C)

Aspect S

Slope 4, 1, 1

Snow temp -3.7, -3.7

Snow table depth 35, 30, 33, 33

Thin snow over ice 12, 1, 5, 1

Ice roughness parallel to beam (cm)

11.8 13.4 14.3 16.9 14.2 25.4 13.7 13.8

13.8 13.6 13.4 11.9 8.8 8.8 8.9 9.3

9.1 9.3 8.6 8.4 8.4 8.5 8.4 8.3

8.2 8.2 7.5 7.8 7.4 6.4 6.2 5.7

5.4 5.4 6.5 6.7 6.8 7.2 6.7 7.2

4.5 Ave 9.6

Ice roughness perpendicular to beam (cm)

4.5 5.2 5.3 5.1 4.5 4.4 5.9 5.9

6.2 6.0 6.4 7.7 6.8 6.7 7.8 9.5

7.4 7.9 7.4 7.7 7.9 8.0 9.2 11.7

9.9 9.4 10.0 8.5 7.9 7.9 7.9 8.3

8.3 11.5 8.8 8.8 8.0 8.8 12.5 11.9

13.2 Ave 7.9

Exposed ice 5%

Tables 20% (starting to look like sastrugi)

Snow covered ice 75%

T8 (G)

Aspect SE

Slope 5, 4

Snow temp -1.7, -0.7, ice -1.8

Snow table depth 21, 14, 30, 14

Thin snow over ice 3, 4, 2, 2 snow only collects in shallow depressions.

Exposed ice 50%
 Snow tables 35%
 Snow covered ice 15%

Some cryoconite holes largely hidden by snow
 200 m from T7, surface changes to 50-50 ice snow, snow mounded into flat-topped dune-like features.

T8 (G)

Ice roughness parallel to beam (cm)

1.3	3.4	4.2	4.8	6.0	4.9	7.4	6.9
7.4	11.1	11.4	12.4	6.6	8.2	6.7	5.5
6.3	8.5	5.4	5.5	6.3	6.2	5.3	7.0
5.4	5.5	5.8	5.8	5.5	5.2	4.9	5.4
5.7	5.9	6.2	6.3	6.0	6.9	9.6	7.8
14.0	16.0		Ave 6.8				

Ice roughness perpendicular to beam (cm)

10.4	12.0	13.0	14.0	10.1	10.0	10.0	9.5
9.0	8.5	8.4	8.2	8.1	8.1	9.2	12.4
9.4	7.0	6.7	6.9	6.8	6.5	6.8	9.5
20.6	12.0	9.7	7.3	9.7	7.7	11.3	8.1
7.8	8.5	8.1	8.0	8.3	8.4	3.5	7.8
8.8		Ave 9.1					

T8 (G)

GPS 0.67 km from MARTHA (change 500 m)

Snow table 35%
 Thin snow 65%

T9(C)

Aspect SE

Slope 5 on ice, 2 on snow table.

Snow temp -2.4, ice -0.8

Snow table depth 27, 22, 19, 16

Thin snow over ice 5, 1, 2, 5

Ice roughness parallel to beam (cm)

3.8	4.3	4.4	4.4	4.1	3.0	3.2	3.3
3.2	3.2	3.4	3.3	3.0	3.1	3.2	3.1
2.7	2.6	2.5	2.4	2.3	2.4	2.3	2.0
1.8	1.9	1.7	4.7	5.3	3.9	1.6	1.5
1.4	1.3	1.0	1.4	1.4	1.4	1.5	1.5
2.0		Ave 2.6					

Ice roughness perpendicular to beam (cm)

4.7	5.3	5.4	5.6	5.5	5.4	5.3	5.5
5.5	5.0	4.7	4.7	4.7	4.5	4.5	4.5
4.5	4.3	4.1	3.6	3.5	2.9	2.8	2.8
2.5	2.4	2.4	2.8	4.5	2.6	2.4	2.1
1.9	2.2	2.4	2.1	1.9	1.8	2.0	2.0
1.4		Ave 3.6					

Snow pit 20 cm, bag 0

layer	depth (cm)	mass (g)	crystal size (mm)	hardness
I	17-20	38	0.5 rounds	pencil
II	10-17	20	1 facet/rounds	fist
III	8-10	28	1 rounds	four finger
IV	1-8	24	2 facets	fist

Snow tables	25%
Exposed ice	30%
Thin snow over ice	45%

T10 Upper Reflector

Aspect SSW

Slope 8 on ice, 4 on snow table.

Snow temp -2.4, ice -1.5

Snow table depth 24, 23, 48, 19

Thin snow over ice 2, 1, 2, 3

Ice roughness parallel to beam (cm)

2.2	2.8	1.4	1.9	1.6	1.2	1.4	1.9
3.9	2.8	2.3	2.0	1.4	1.3	1.5	2.0
2.6	2.2	1.7	1.3	1.4	1.4	1.2	2.3
2.4	2.0	2.4	2.5	2.1	1.4	1.2	1.3
2.3	2.6	2.4	2.0	1.3	1.2	2.0	3.7
2.9		Ave 1.9					

Ice roughness perpendicular to beam (cm)

1.5	1.8	2.1	2.4	2.2	1.5	1.1	1.6
2.8	2.9	2.6	2.5	2.4	2.3	2.5	1.8
4.0	4.0	4.0	3.6	3.5	2.8	2.3	1.5
1.4	2.5	2.5	1.8	1.5	1.4	1.4	1.6
1.8	2.3	1.9	1.5	1.0	1.6	4.2	2.5
1.9		Ave 2.2					

Snow pit 39 cm, bag 0

layer	depth (cm)	mass (g)	crystal size (mm)	hardness
I	10-39	43	0.5 rounds	pencil
II	0-10	26	1 stellar	four

Snow tables	15%
Very thin snow	45% snow less than 1 cm deep
Thin snow	40% snow pockets in ice depressions
Cryoconite holes	5%

Cryoconite holes depths

23, 22, 19, 11, 11

T10 (G) Upper Reflector

GPS @ MARTHA

77° 33' 24.3"

163° 12' 49.3"

Ice 85%

Snow table 10%

Thin snow 5%

Cryoconite 5%

Ice roughness parallel to beam (cm)

1.4	1.2	1.2	1.1	0.9	1.4	1.4	1.0
1.4	2.3	3.4	1.9	1.7	2.3	2.6	2.1
1.5	1.4	1.3	2.0	2.8	2.9	2.5	1.4
1.2	1.3	1.0	1.2	1.3	1.8	1.5	1.5
2.3	2.5	3.0	2.8	1.5	1.3	2.0	2.1
3.0		Ave 1.8					

Ice roughness perpendicular to beam (cm)

1.3	1.8	1.5	1.7	1.8	1.7	2.2	2.0
2.1	2.0	2.4	2.5	1.9	1.8	2.0	2.5
4.7	2.7	2.9	2.4	2.3	2.1	2.2	2.0
1.5	1.7	1.5	2.1	2.5	2.7	2.5	3.0
2.8	2.0	1.8	3.0	3.1	1.5	1.0	1.1
1.4		Ave 2.1					

T11

Aspect WSW

Slope 5 on ice, 5 on snow table.

Snow table depth 13, 25, 14, 21

Thin snow over ice 2, 3, 1, 4

Cryoconite depth 8, 9, 13, 15

Snow tables 10%

Exposed ice 40%

Thin snow 30%

Cryoconite 20%

T13 (G) edge of snow/ice

77° 33' 11.5"S

163° 11' 50.2"E

Snow cover 100%

Snow depth

20 15 16 10

Hoar crystals under tables

Snow tables with drifted snow in between

T12 four rope lengths from #11 (200 meters)

Aspect S

Slope 4

Snow depth 21, 54, 63, 65

Surface completely snow covered

Snow pit 49 cm

layer	depth (cm)	crystal size (mm)	hardness
I	29-49	2.0 rounds/stellars	fist
II	25-29	dirty layer	one finger
III	22-25	ice layer	
IV	0-22	3.0 hoar crystals	one finger

T14 (G)

77° 33' 12.1"S

163° 11' 24.2"E

Snow depth

62 53 61 59 63 62 58

Snow pit depth 59 cm

11 cm to top of ice layer, 4 cm thick

15 cm deep to top of next ice layer, 9 cm thick

Not ice, but melt/refreeze snow-compacted grains, had to chop with axe.

T15 (G)

77° 33' 9.6"S

163° 11' 0.9"E

Snow depth

73 79 57 58 69 70

Hard snow

66 37 26

T16 (G)

77° 33' 06.5" S

163° 10' 49.0"E

Snow depth

66 63 57 60 57

Hard snow

47 40 41

Howard Glacier.

Howard Glacier field data taken on 1/27/99 positions are either at mass-balance stake locations or located by GPS.

Site 1 near Stake 31, Metrological station

Ice	75%						
Snow table	20%						
Snow	5%						
Cryoconite holes	15%						
Cryoconite depth	8	10	15	10	14	8	

Ice roughness parallel to beam (cm)

3.3	1.3	1.8	1.9	1.9	2.0	2.0	2.0
1.9	2.4	2.6	2.2	1.7	1.4	1.5	1.3
1.0	1.3	1.5	1.3	0.9	1.8	2.0	1.9
1.9	2.4	3.2	4.9	3.2	2.8	1.5	3.4
4.5	5.2	1.8	0.9	2.6	2.9	4.0	2.9
4.3		Ave 2.3					

Ice roughness perpendicular to beam (cm)

1.3	1.8	1.2	1.9	2.3	1.9	1.9	1.8
1.9	2.1	2.8	2.8	3.2	2.0	1.8	1.4
1.3	1.5	2.0	2.6	2.8	2.9	3.4	3.3
3.5	1.7	2.0	2.4	1.8	1.4	2.0	2.3
2.1	2.9	0.9	1.9	1.2	2.7	0.9	1.5
2.9		Ave 2.0					

Site 2 near Stake 30

Ice	15%						
Snow table	10%						
Snow	75%	snow depths	3	5	5	5	
Cryoconite	2%						

Ice roughness parallel to beam (cm)

6.0	4.8	4.3	4.0	3.9	3.2	2.5	2.2
1.4	1.9	2.3	2.4	2.3	2.7	3.9	3.0
3.0	2.0	1.9	2.3	2.5	2.5	6.3	5.4
4.7	4.3	4.5	3.6	3.9	2.4	2.1	1.5
1.8	5.0	3.7	4.9	4.7	3.7	3.8	3.9
3.6		Ave 3.3					

Ice roughness perpendicular to beam (cm)

4.3	4.2	4.7	4.0	4.7	4.4	4.5	4.3
4.6	5.8	5.3	5.5	6.7	7.6	7.5	7.9
8.0	8.2	8.5	8.0	6.5	6.5	5.9	4.8
4.7	5.2	3.3	3.0	2.5	2.6	2.5	1.9
2.5	1.4	0.9	1.1	1.6	1.7	2.1	3.5
5.6		Ave 4.5					

Site 3

77° 40' 43.2"

163° 04' 52.6"

100% snow cover approx 10 cm deep

Site 4

77° 40' 35.2" S

163° 04' 50.0" E

(Just a few 10s of meters from last position)

Snow depth	28	18	29	27	22
------------	----	----	----	----	----

Site 5

77° 40' 44.5" S

163° 05' 0.00" E

(Almost level with stake 29, just a bit down glacier from it.)

Snow depth	32	42	42	45	44	39
------------	----	----	----	----	----	----

Appendix C

Full Description of Steps to Acquire Programs, Convert Data, and Run the Terrcorr
Terrain Correction Program.

Terrcorr Steps

1. Download the terrain correction program called "Terrcorr" from the Alaska SAR Facility (ASF). From the ASF main page (<http://www.asf.alaska.edu/step/intro/man/Terrcorr.html>) click on the tools link, terrain correction link, and finally the Terrcorr link to the download page at <http://www.asf.alaska.edu/step/intro/man/Terrcorr.html>. The manual page for Terrcorr is at: <http://www.images.alaska.edu/man/Terrcorr.html>. All the programs from ASF and the LAS (step #5) site require a UNIX computer. (Our computer had problems running Terrcorr using the pre-compiled binaries, but after self-compiling the program ran well.)
 - a. Load the compressed source file into an empty directory. Terrcorr expands into over 350 files in 30 directories.
 - b. In the base directory created by the Terrcorr install, run the script called "config" (type "./config" at the command line). Answer the questions that are issued to allow the software to set itself up correctly for the subject system. Note: For SunOs users the GCC compiler must be used and not the standard compiler installed on the system.
 - c. Type "make" to start compilation. The programs are located in a directory below (not in) the asf_tools directory called "bin."

2. Download and run test data to make sure the program is operating correctly.

Our test data of the Fairbanks, Alaska area came from Dorothy Corbett

(dcorbett@asf.alaska.edu). This data should be available soon as a resource on the

Terrcorr web page.

3. The resolution of the DEM must be less than or equal to the resolution of the

SAR data. The metadata reader available at ASF displays the SAR pixel size

(<http://www.asf.alaska.edu/step/intro/metadata/>).

4. The SAR data should already be in UTM (Universal Transverse Mercator), and this is verifiable by the ASF metadata reader program. For this experiment, some data manipulation was required to prepare DEM for conversion into the LAS format.

a. The DEM was converted into UTM using ArcInfo.

The commands used were: `project grid dem50k30 50k30utm # bilinear 30; output; projection utm; zone 58; parameters; end.`

b. The DEM was converted into ASCII format in ArcInfo using the following command: `gridascii 50k30utm 50k30utmascii.`

c. All headers were removed.

d. The "no data" values in the DEM were changed from -9999 to 0 (zero).

5. The DEM must be in LAS format. The Land Analysis System (LAS) is an image analysis system designed to ingest, manipulate, and analyze digital image data and to provide the user with a wide spectrum of functions and statistical tools for image analysis. The website is located at

<http://edcwww.cr.usgs.gov/programs/sddm/lasdist/>.

- a. To access the programs to download, you must first register.

Responses to a registration request take a week or so.

- b. LAS binaries require no recompilation.

- c. Make a directory for the LAS and TAE software in the home directory (mkdir las72), and gunzip the tar/gzip compressed LAS and TAE packages.

```
gunzip -c ../las_72_sun_tar.gz|tar -xof -
gunzip -c ../taesun.tar.gz|tar -xof -
```

- d. Set up the environment variables needed by the software and run the lasinit routine.

```
setenv EDCSOFT $HOME/las72
setenv TAE $EDCSOFT/tae
set reponse=las72
source $EDCSOFT/env/las/assign/lasinit
```

- e. Convert the DEM file with: makeimg outfile.img 50k30demlas.img 4875 4244 (makeimg, name_of_output_image, name_of_DEM, number_of_rows_in_DEM, number_of_columns_in_DEM).

6. A *.ddr file is the metadata companion to the LAS DEM. The LAS conversion program made a *.ddr file, but all the fields were zero. The ASF makeddr

program was used to make a useful metadata *.ddr file. The command used was:
makeddr 50k30demlas 4875 4244 2 UTM 58 -8572783.9698809 376926.96591685 -
8719033.9698809 503246.96591685 30. The corners were calculated by multiplying
the DEM cell size (30) to the total number of rows and columns and adding the
results to the x and y of the lower left point of the DEM. The ASF program dspddr
displays all the information in the *.ddr file.

7. In this experiment, Terrcorr was run with the following commands: Terrcorr -
cf1 E219549658G1S005 [the SAR image] 50k30demlas2 [the DEM].

8. The final corrected image had "smeariness" on the mountain sides sloping
away from the SAR beam. Normally this correction artifact is on the slopes facing the
SAR beam. This raised concern about the accuracy of the correlation, a concern
shared by Tom Logan from ASF, who speculated that the DEM might contain some
inaccuracies. Terrcorr was re-run using the -l flag in order to save intermediate files.
For unknown reasons some of the needed files were still being deleted. Terrcorr was
run again both with the "-l" flag and using the UNIX "link" command saving copies
of the intermediate files into another directory (In pE219549658G1S005 pE2.save).

The fsE219549658G1S005 (filtered simulated image) and the
pE219549658G1S005 (preprocessed SAR image) images (which are created in an
intermediate Terrcorr step) were compared in ENVI (a remote sensing image analysis
program) using the offsets found in the coef.ppf file.

```

AZ1COEF   R 1 0.0
AZ2COEF   R 1 0.0
AZ3COEF   R 1 -59.782897 [the line offset]
GR1COEF   R 1 0.0
GR2COEF   R 1 0.0
GR3COEF   R 1 3.758089 [the sample offset]

```

The two images were still considerably offset from one another. The displacement from the fsE219549658G1S005 (filtered simulated image) to the pE219549658G1S005 (preprocessed SAR image) was calculated, and the offsets were inserted into the coef.ppf file as follows:

```

AZ1COEF   R 1 0.0
AZ2COEF   R 1 0.0
AZ3COEF   R 1 -140.0 [line offset]
GR1COEF   R 1 0.0
GR2COEF   R 1 0.0
GR3COEF   R 1 6.0 [sample offset]

```

If there are any other numbers where 0.0 is displayed, they should be deleted. These numbers are for the 2-d planar warp map. When Terrcorr successfully correlates, it creates a 2-d planar warp map using many points across the image, fitting a function in range and a function in azimuth. The other numbers (AZ1, AZ2, GR1, and GR2) are no longer valid if the absolute offsets (AZ3, GR3) are changed.

Sargeom (which is one of the final steps in Terrcorr) was then invoked with the command: sargeom pDEM (the clipped DEM file) pE219549658G1S005 (the pre-processed SAR image) coef E21.corr4 (the output terrain corrected file). This step only took a few minutes to run and yielded the final image. Tom Logan (ASF) noted that the image was not a particularly "crisp" terrain correction, but was "fairly good" and much better than what the Terrcorr auto-correlation yielded.

Appendix D

November 2000 Snow Depths Near Sakes 19 and 21.

Commonwealth Glacier transect from Stake 21 to the NNE

Probe 1 GPS Coordinate: S 77 32.323 E 163 02.257

	Depth from Surface to hard layer (cm)	Difficulty of penetrating through hard layer
1	7	hard
2	22	hard
3	50	easy
4	84	hard
5	150	very hard, could not penetrate

Probe 2 GPS Coordinate: S 77 32.271 E 163 02.187

	Depth from Surface to hard layer (cm)	Difficulty of penetrating through hard layer
1	9	easy
2	37	moderate
3	97	moderate
4	150	very hard

Probe 3 GPS Coordinate: S 77 32.177 E 163 02.546

	Depth from Surface to hard layer (cm)	Difficulty of penetrating through hard layer
1	23	easy
2	80	very hard
3	98	hard
4	185	hard

Probe 4 GPS Coordinate: S 77 32.167 E 163 04.317

	Depth from Surface to hard layer (cm)	Difficulty of penetrating through hard layer
1	19	easy
2	49	easy
3	85	easy
4	91	very hard
5	125	very hard

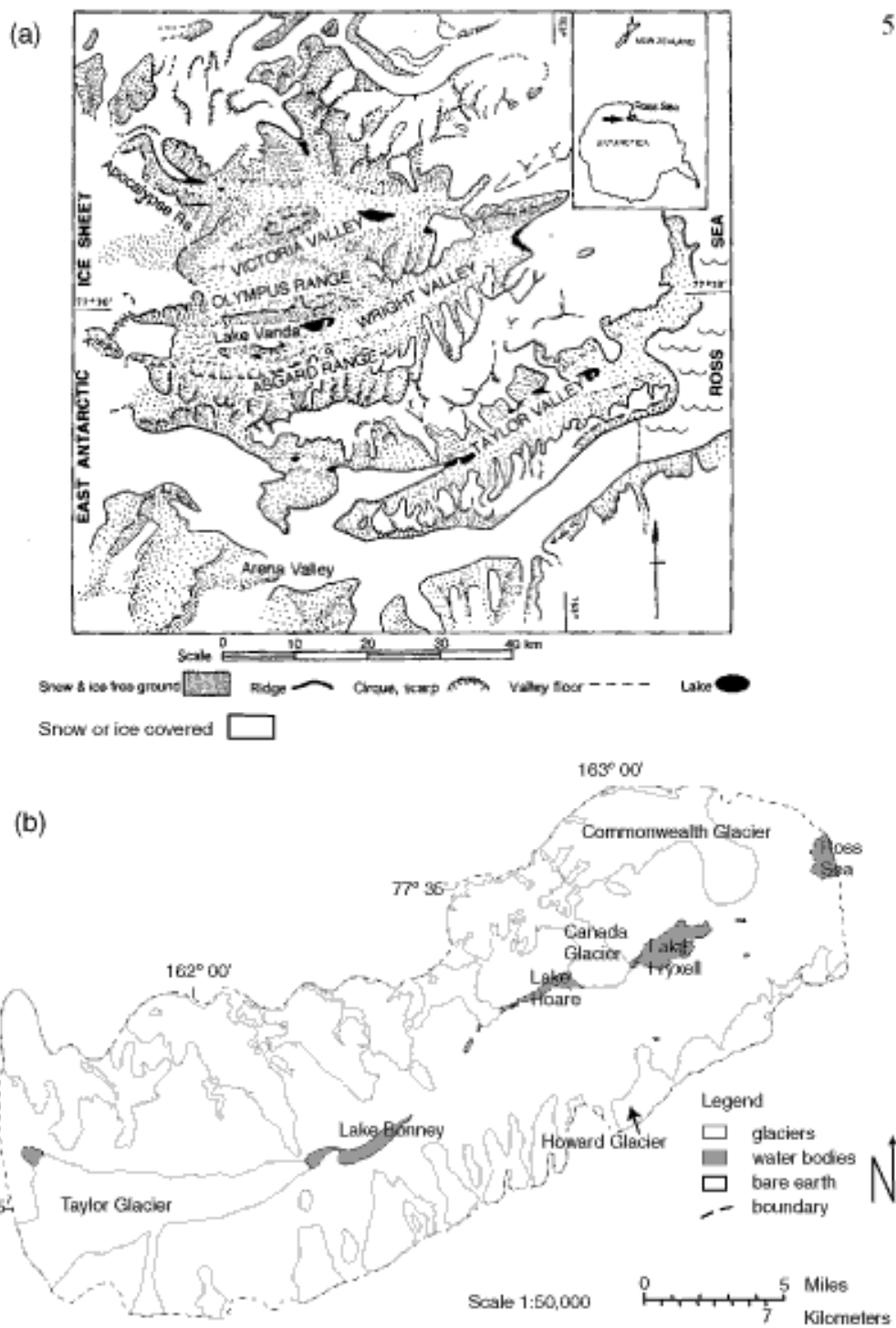


Figure 1.1: site maps. (a) The McMurdo Dry Valleys (Chinn, 1996), (b) Taylor Valley (INSTAAR MCM Long-Term Ecological Research website).

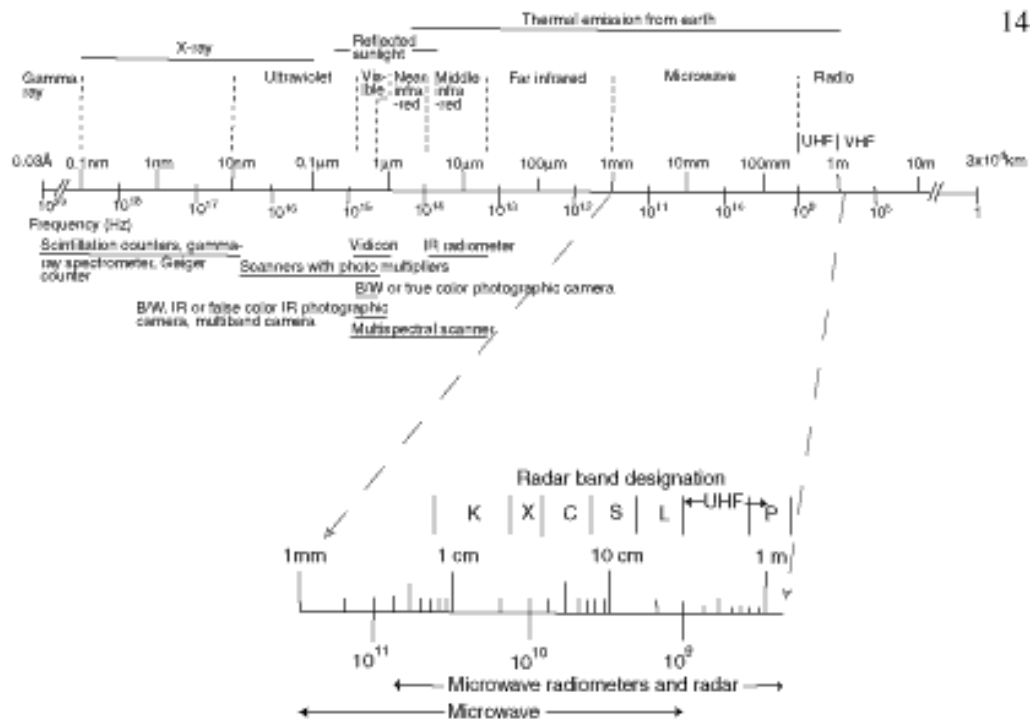


Figure 3.1: The electromagnetic spectrum (Trevett, 1986).

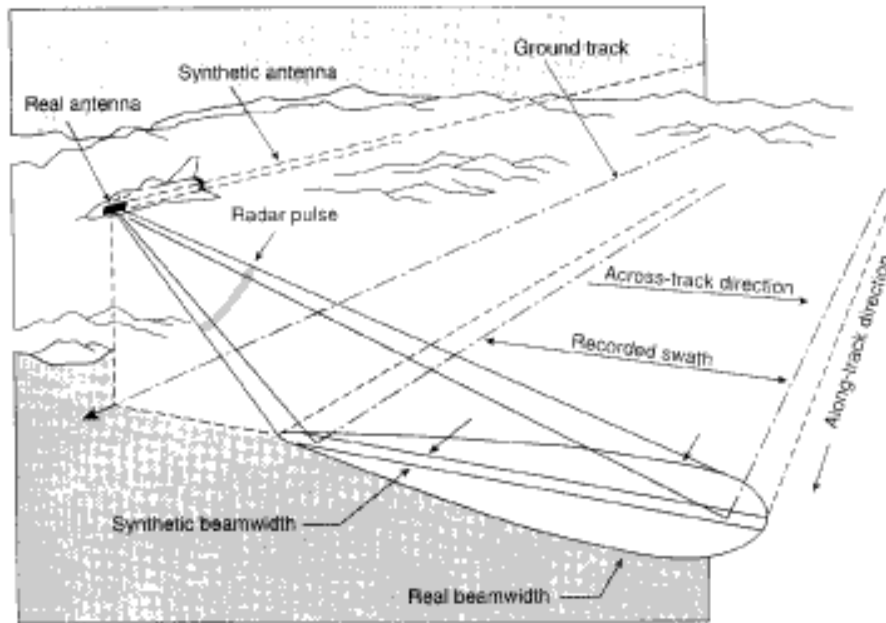


Figure 3.2: Operating principle of a SAR (Avery and Berliir 1992).

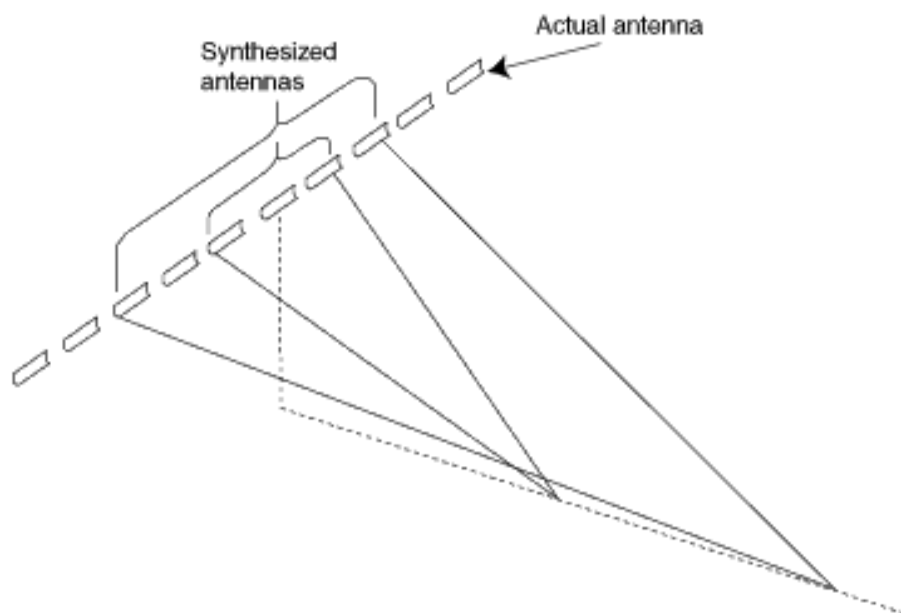


Figure 3.3: Concept of an array of real antenna positions forming a synthetic aperture (Lillesand and Kiefer, 1994).

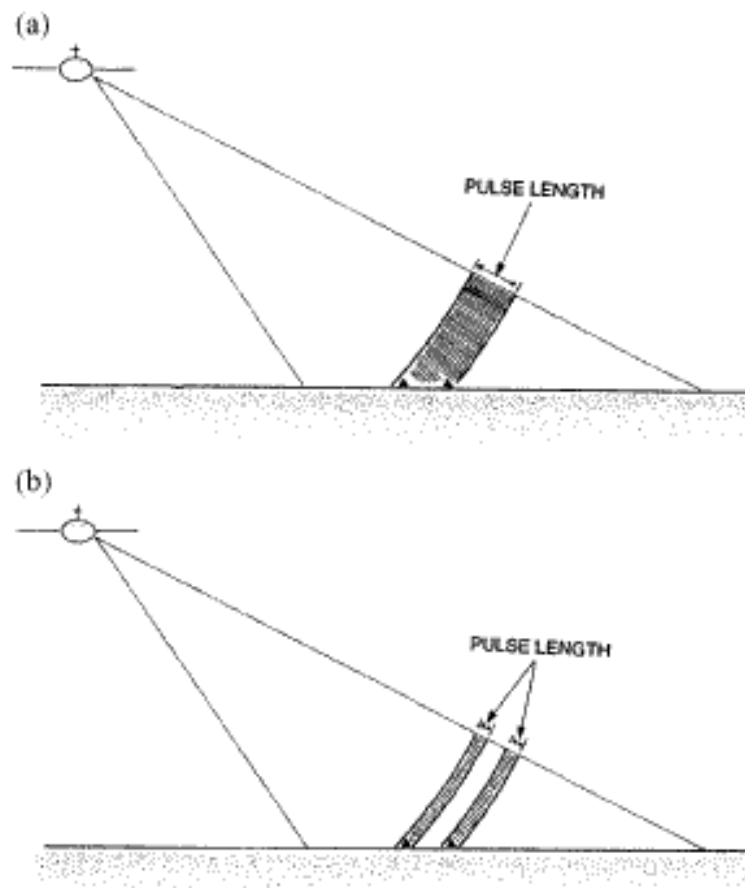


Figure 3.4: Effect of pulse length (Cambell, 1996). Long pulse length (a) causes the two objects to be illuminated by a single radar burst, creating a single return that does not resolve the two objects. Short pulse length (b) illuminates the objects with separate radar bursts, creating separate returns and resolving the two objects.

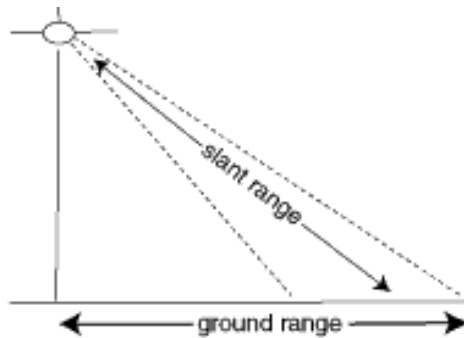


Figure 3.5: Slant and ground range (Campbell, 1996).

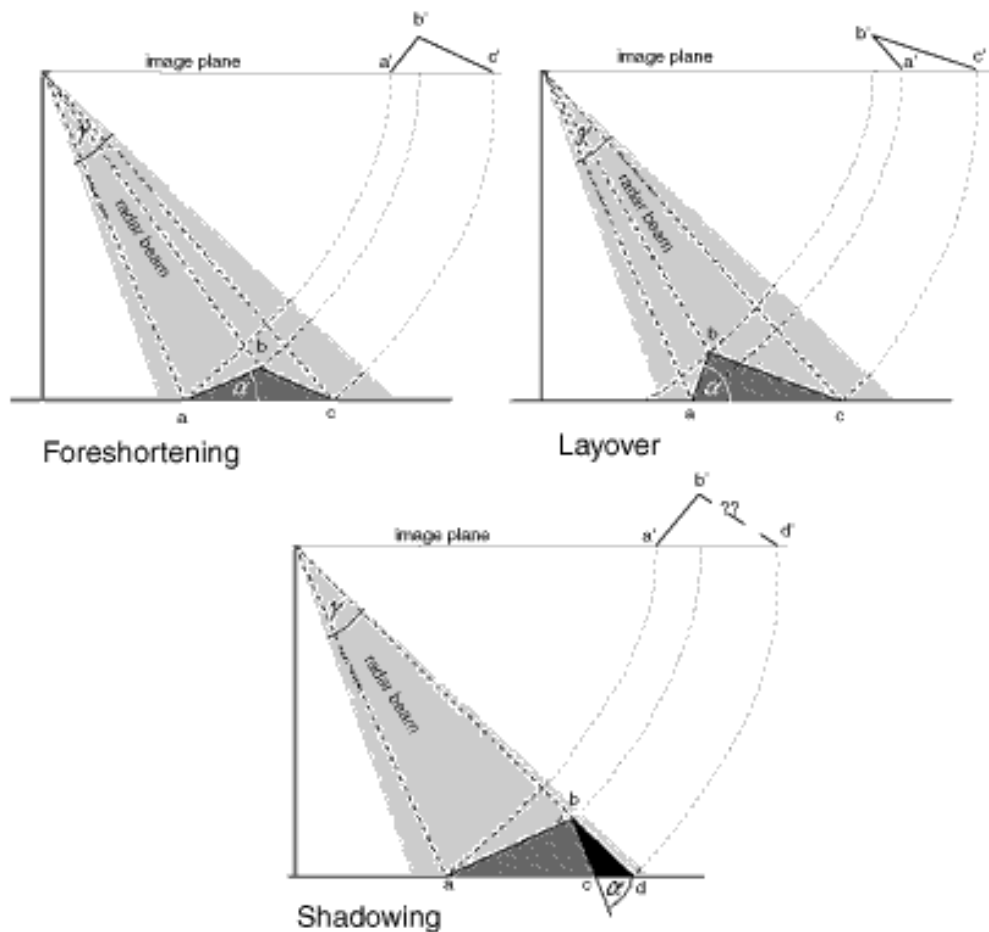


Figure 3.6: SAR geometric distortions (Olmsted, 1993). In foreshortening, point "b" is closer to the SAR than its actual ground distance. In layover, point "b" is closer to the SAR than point "a." In shadowing, a portion of the mountain is not illuminated, no data is received for this area.

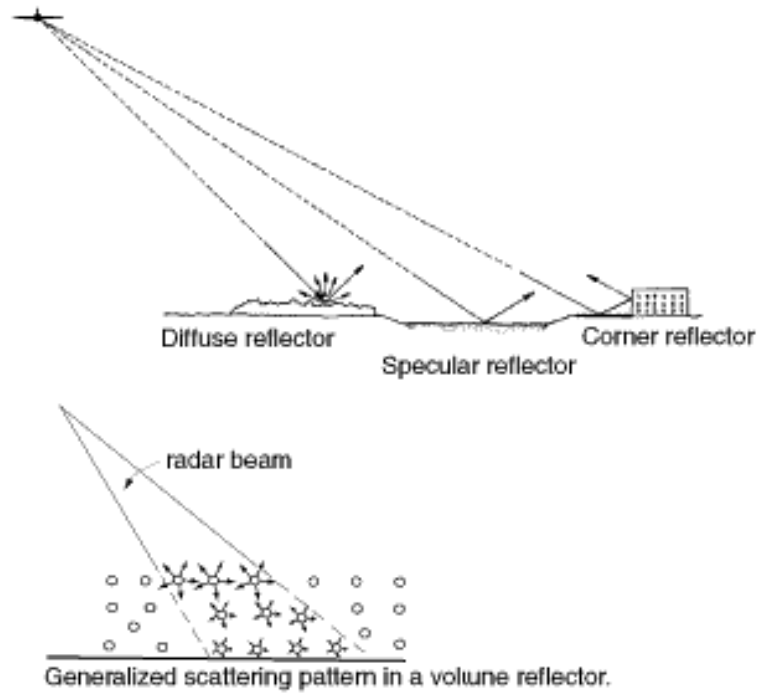


Figure 3.7: Diffuse, specular, corner (Lillesand and Kieffe, 1994), and volume reflection (Ulaby et al., 1981).

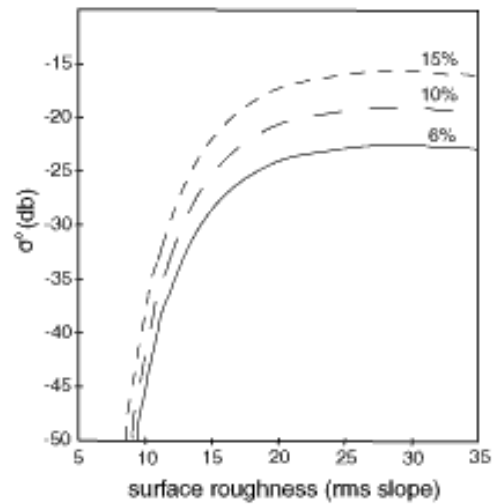


Figure 3.8: Simulated σ^0 curves for three wet snowpacks (liquid water contents: 6, 10, and 15%), using a geometric optics model of radar backscattering (SAR average incidence angle 12°). Increased backscattering is associated with increased surface roughness. Surface roughness is parametrized as the root-means-square slope of the surface (Smith et al., 1997).

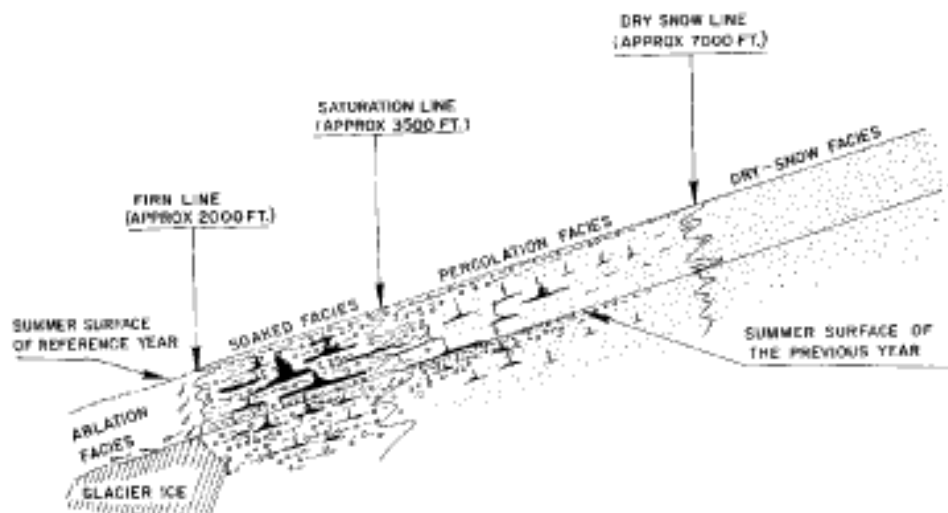


Figure 3.9: Benson's generalized cross-section of glacier facies (Benson, 1962).



40

Figure 4.1: ERS-2 and Radarsat look angles (dashed arrows) relative to Commonwealth and Howard Glaciers. Orientations and scale correct but positions are arbitrary.

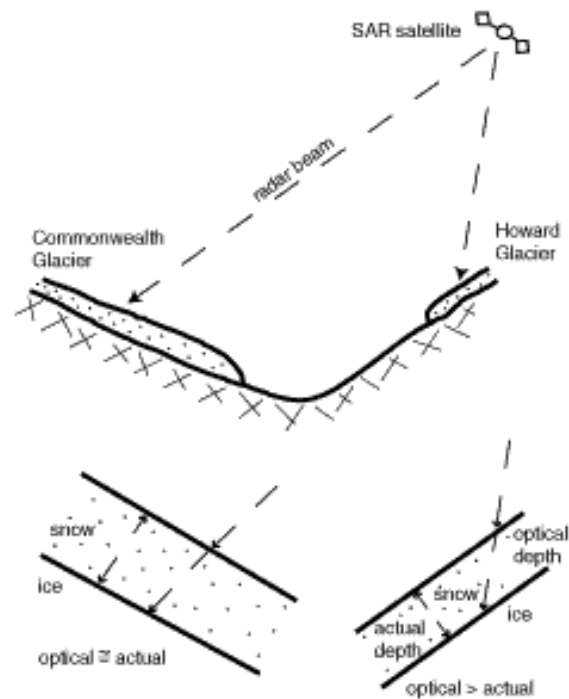


Figure 4.2: Optical depth vs. actual depth.

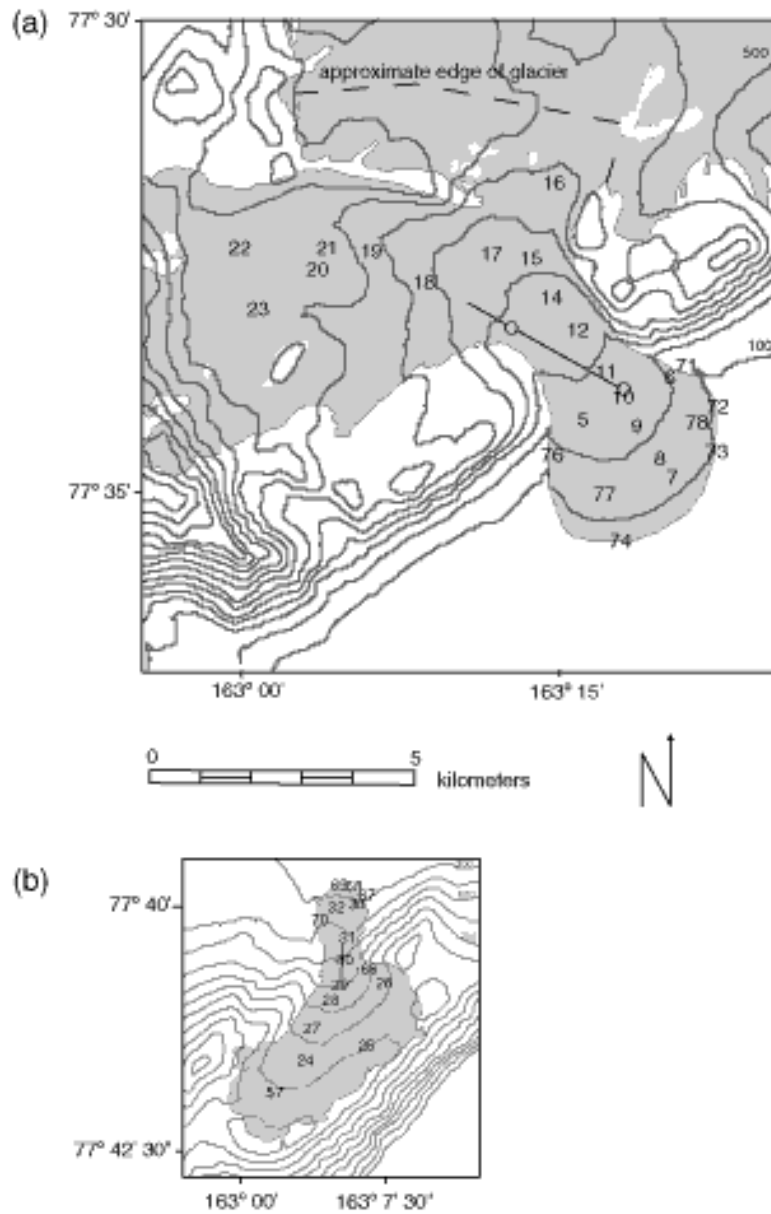


Figure 4.3: Snow stakes on (a) Commonwealth and (b) Howard Glaciers. Numbers indicate snow stake location, lines are transect locations, and contour interval 100 m.

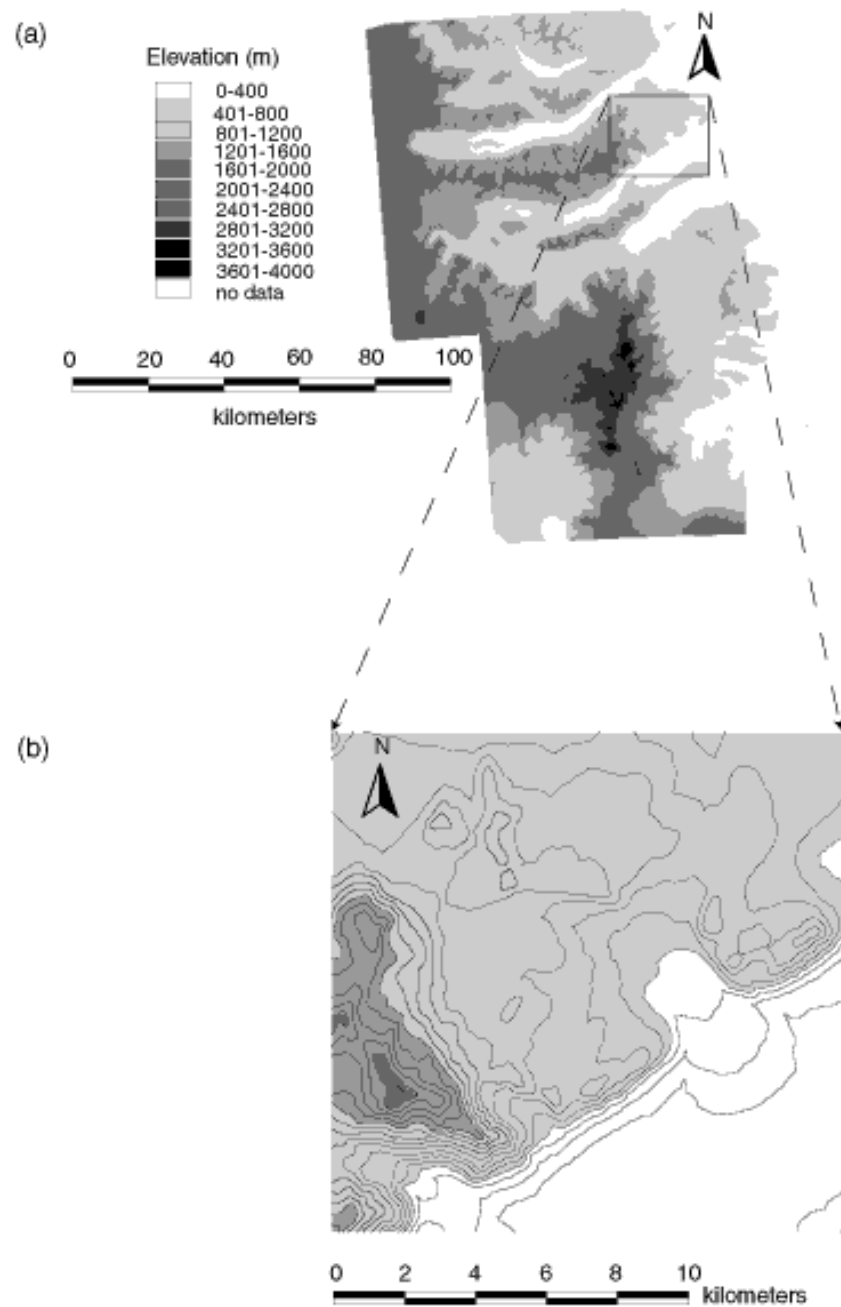


Figure 4.4: A visual representation of the digital elevation model of (a) Southern Victoria Land, Antarctica. (b) Commonwealth Glacier and surrounding area. Contour interval 100 meters.

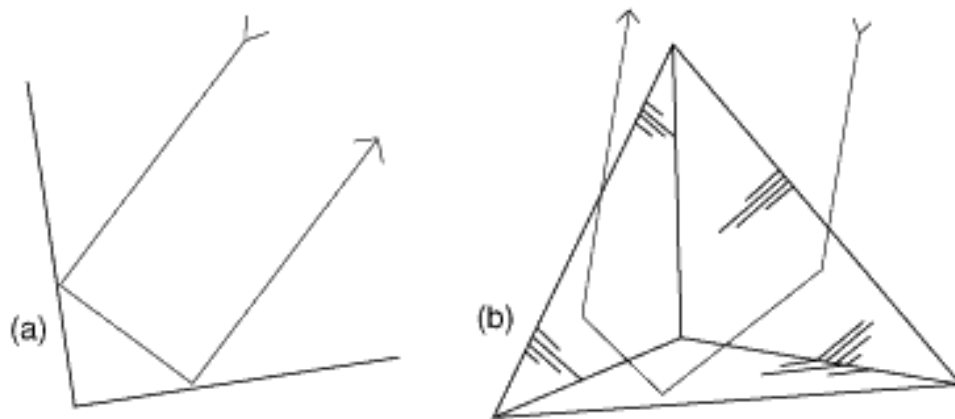


Figure 4.5: (a) A ray diagram of the reflection in a dihedral corner reflector. (b) A ray diagram of the reflection in a triangular trihedral corner reflector (Fuller, 1970).

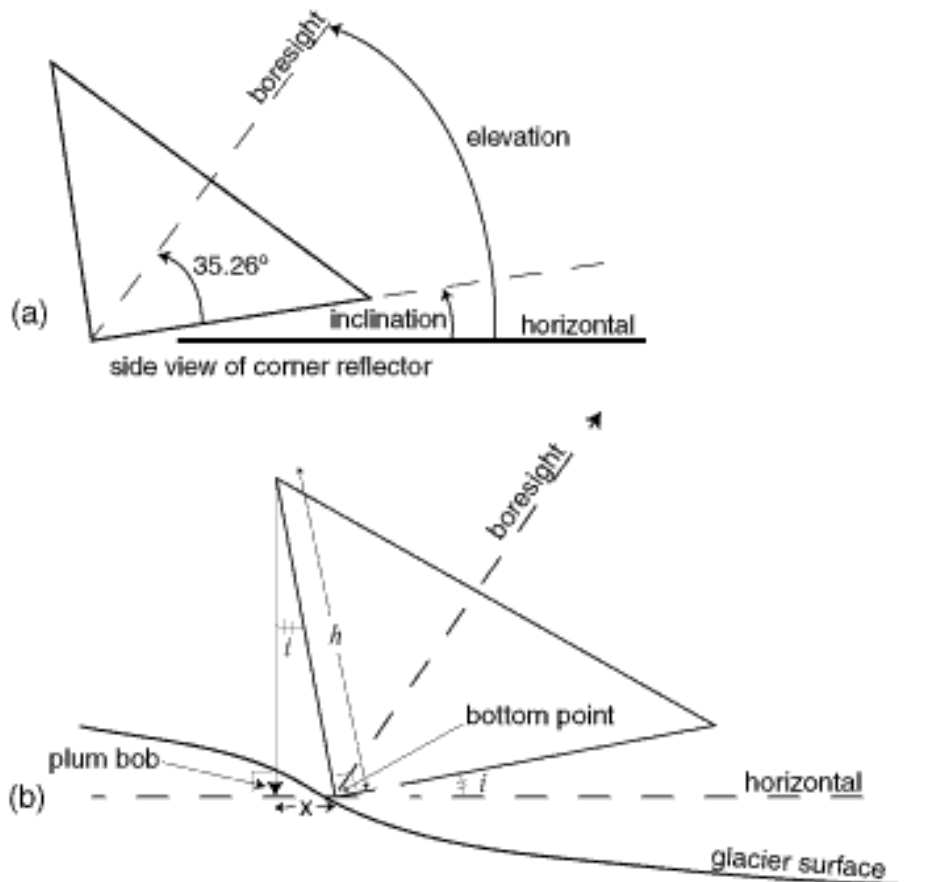
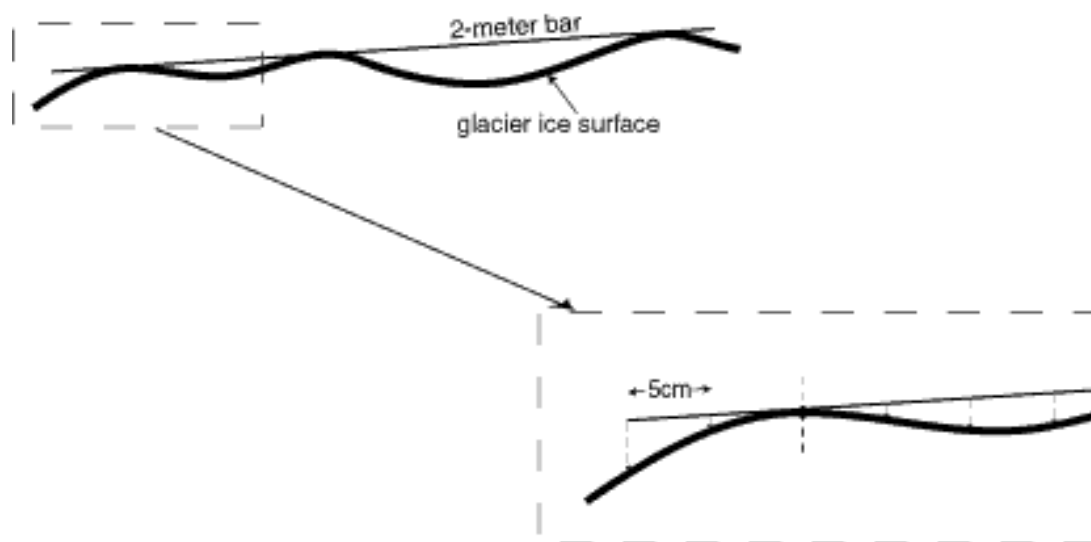


Figure 4.6: (a) Inclination angle (ASF website). (b) Determining the inclination angle.



Figure 4.7: A trihedral corner reflector.



53

Figure 4.8: Ice surface roughness measured from a 2 m bar to ice surface.

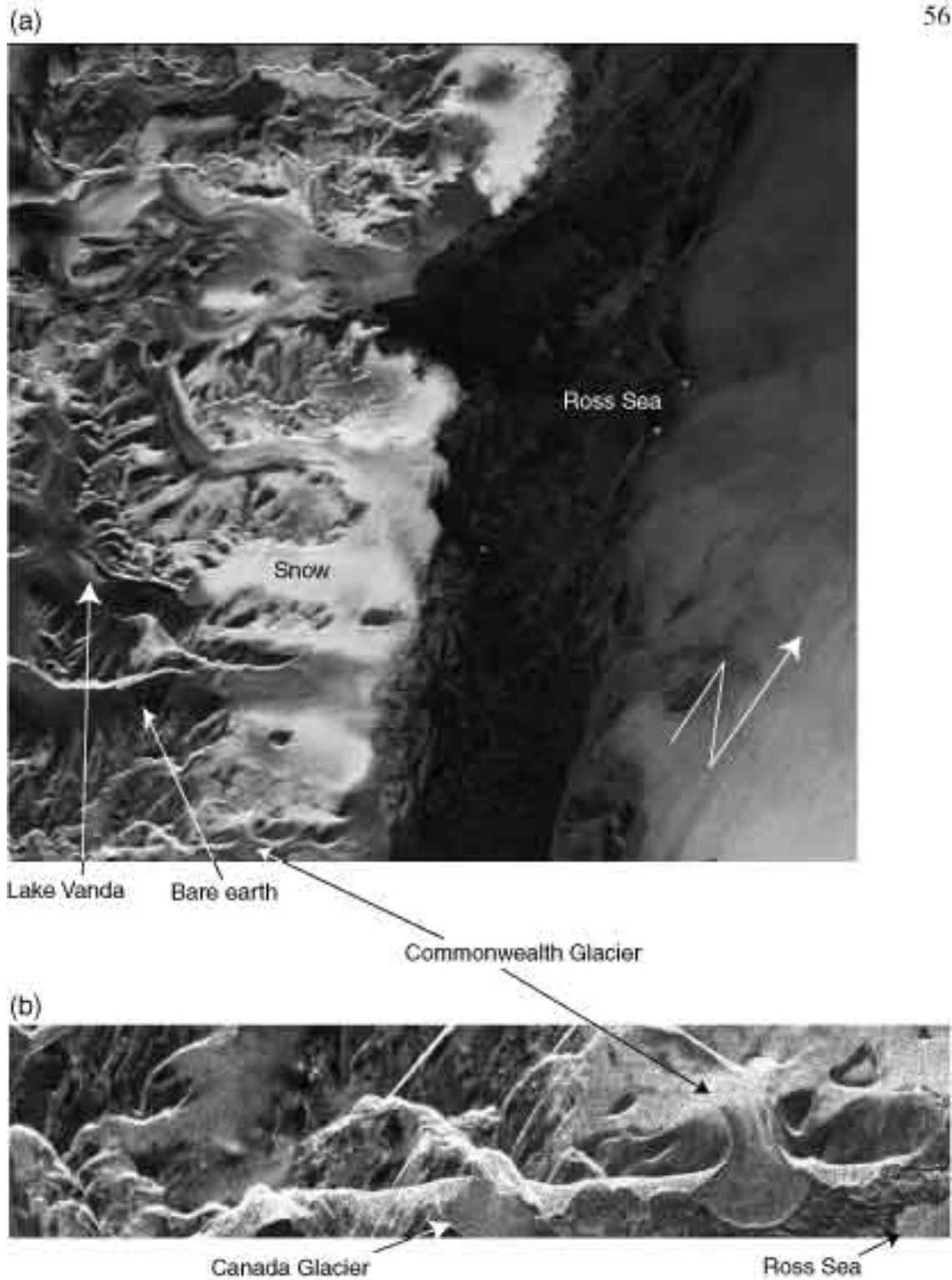


Figure 5.1: ERS-2 uncorrected SAR: (a) full scene, (b) detail of portion of Taylor Valley. Images ©1999 European Space Agency.

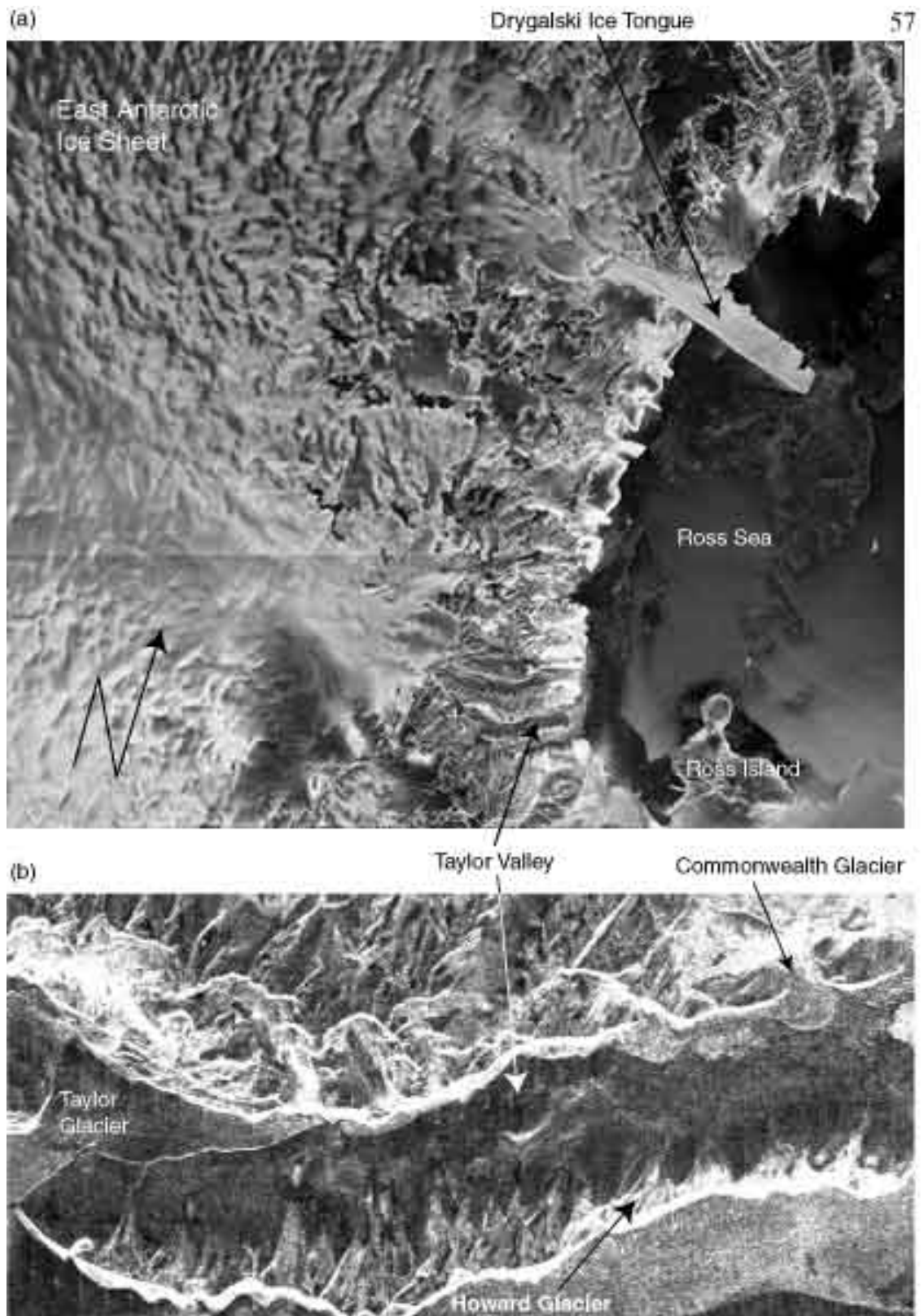


Figure 5.2: Radarsat uncorrected SAR: (a) full scene, (b) detail of Taylor Valley. Image ©1999 Canadian Space Agency.

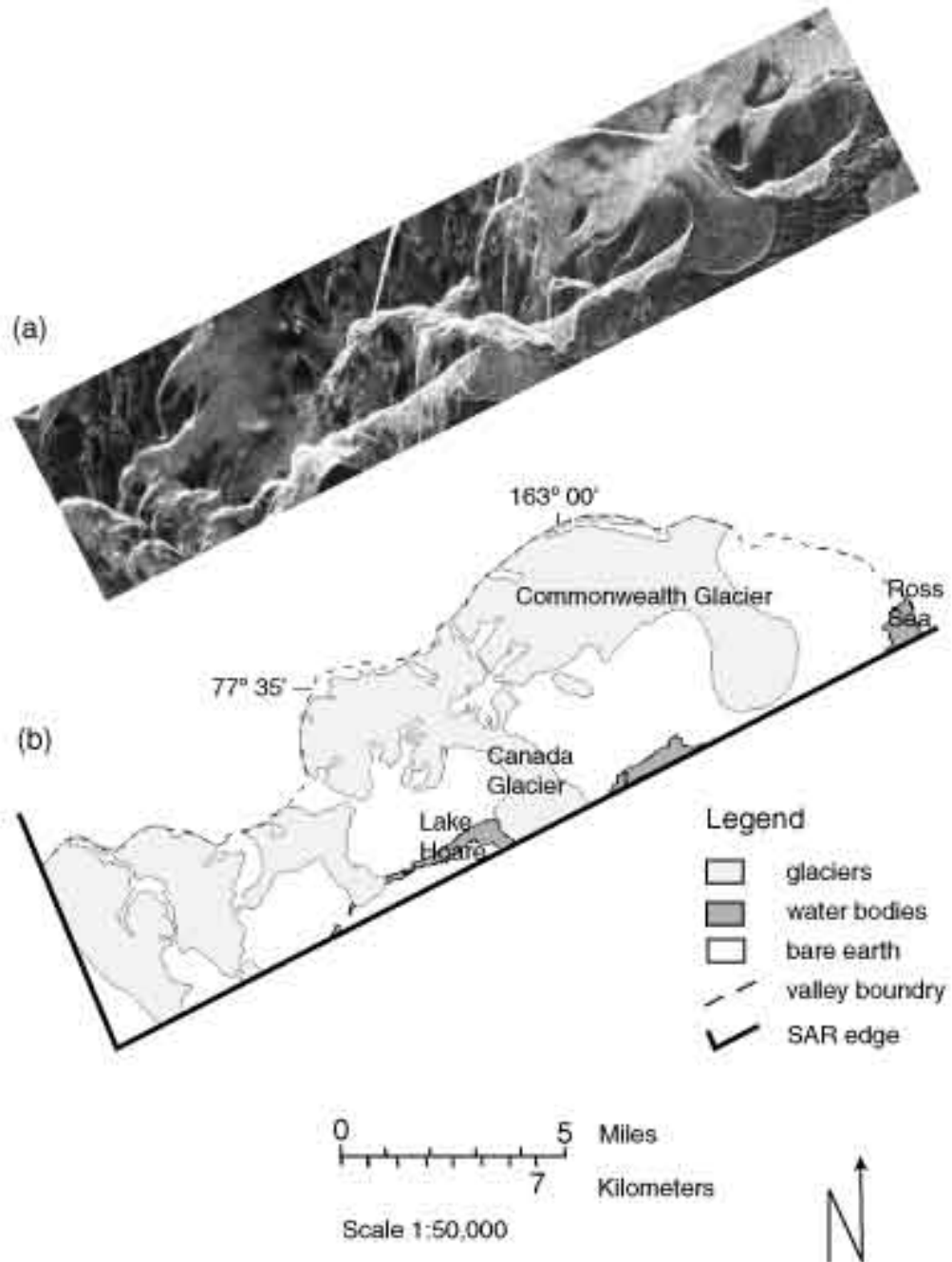


Figure 5.3: The portion of Talor Valley that was imaged by the ERS-2 SAR (a) uncorrected SAR, (b) map.

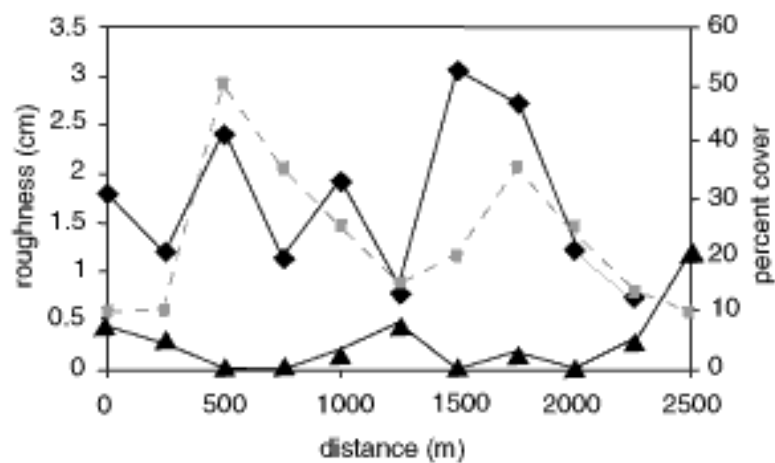


Figure 5.4: Surface characteristics along the transect on Commonwealth Glacier. Standard deviation of roughness is indicated by the black diamonds. Snow tables (given as percentage of area cover) are indicated by gray squares and dashed lines. Cryoconite holes (also presented as percentage of area cover) are indicated by black triangles.

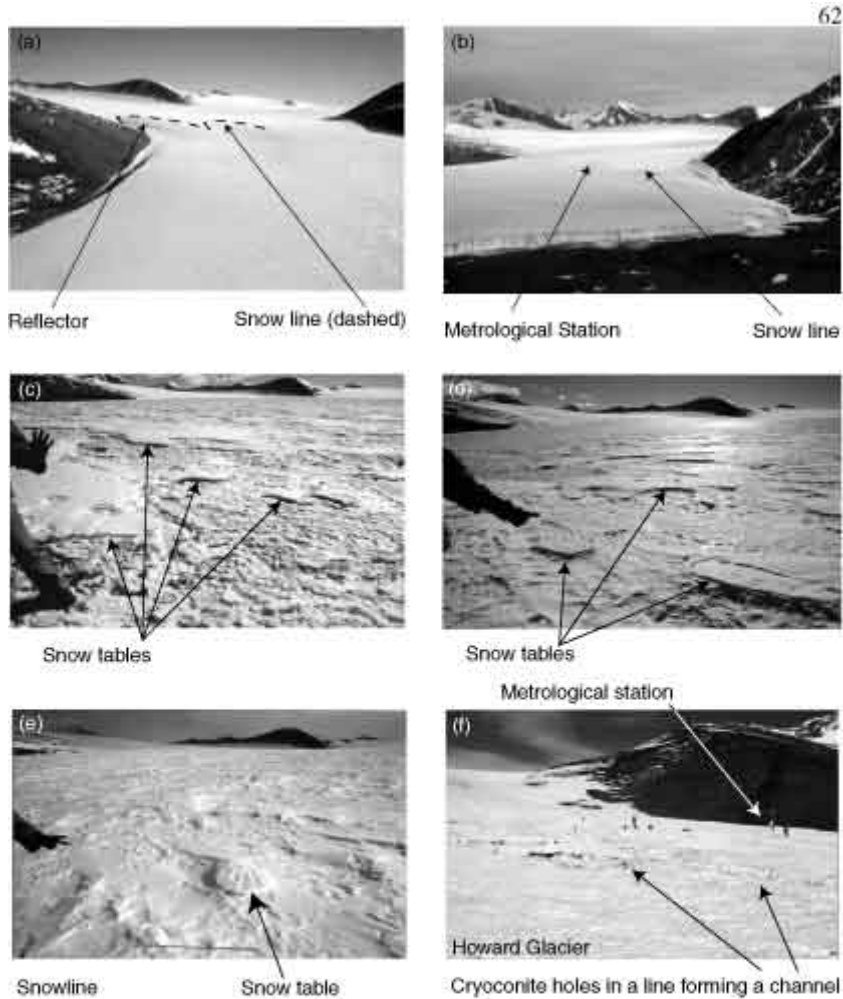


Figure 5.5: Hand-held photographs of Commonwealth (a-e) and Howard (f) Glaciers. (a) West side of snowline from helicopter 300-500' above ground level taken January 20, 1999 looking approximately NNW. (b) East side of snowline from helicopter looking approximately West (same date and flying height as (a)). (c) Site 4 on transect, looking NW. (d) Site 6 on transect, looking NW. (e) Above snowline at site 12 on transect looking NW. (f) Cryoconite hole channel on Howard Glacier in ablation area. Photos a,c,d,e © 1999 Patrick J. Bardel, b,f © 1999 Andrew G. Fountain.

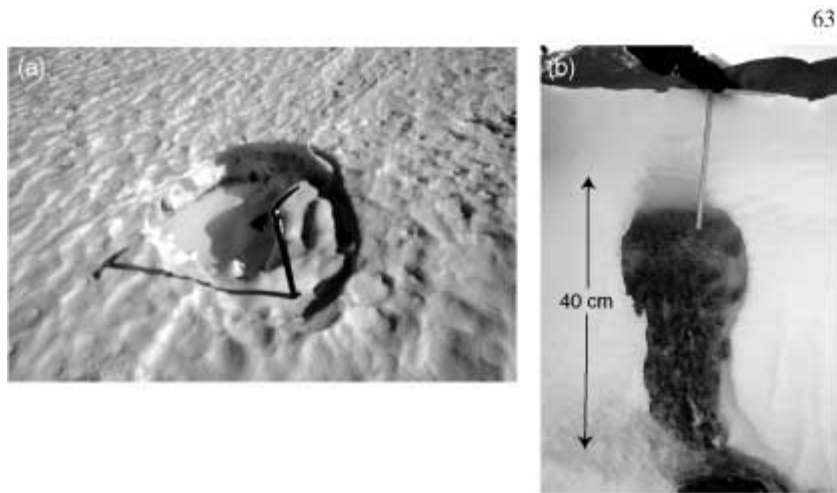


Figure 5.6: Cryoconite hole (a) top view with ice axe for scale, (b) side view of cannibalized hole on side of cliff.

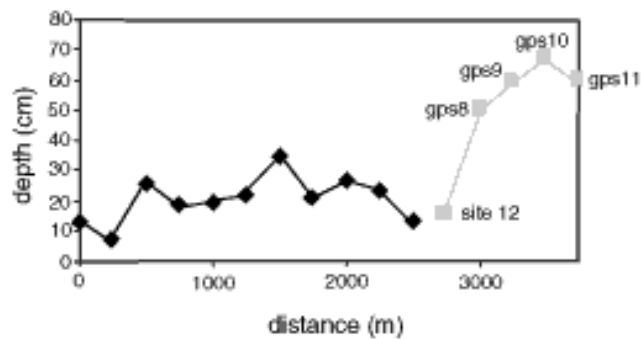


Figure 5.7: Snow depths along the transect on Commonwealth Glacier. Black diamonds are averaged snow depths on snow tables in the ablation area; gray squares are averaged depths in the accumulation area.

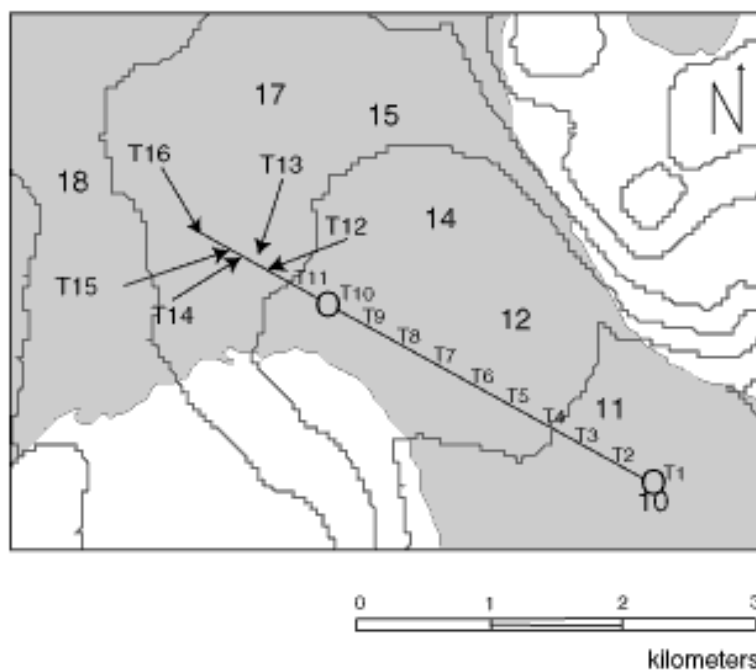


Figure 5.8: Snow stakes (numbers), radar reflectors (circles), transect route (line), and sample sites (T1-T16) on Commonwealth Glacier. Location of sample sites are where label touches transect line, at arrow point, or at center of reflector location circle. Contour interval 100 m.

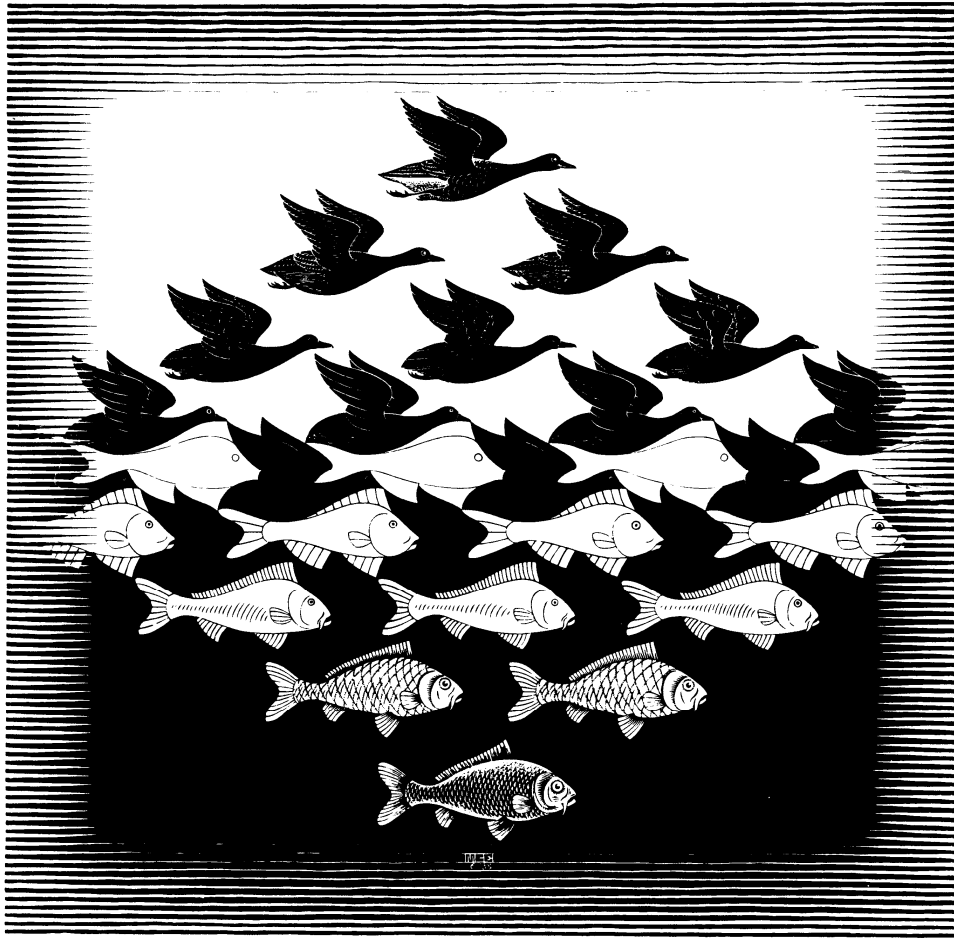


Figure 5.8 Sky and Water I

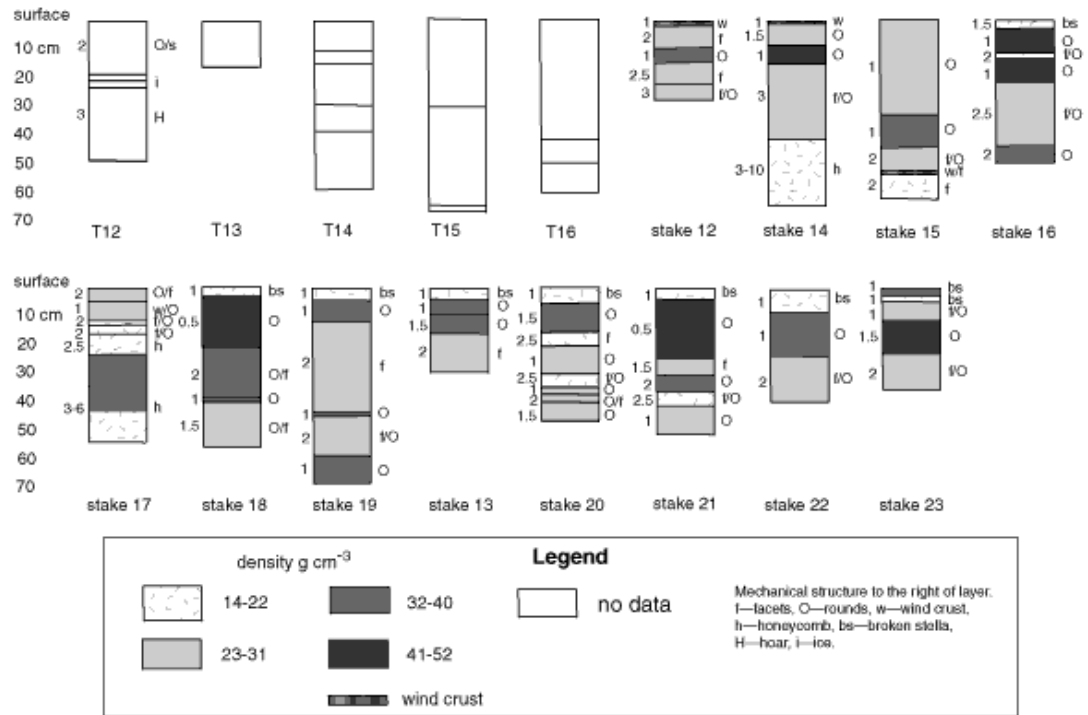


Figure 5.9: Snow layers graph. Grain size (mm) to the left of layer. Numbers to the far left indicate depth of layers.

67

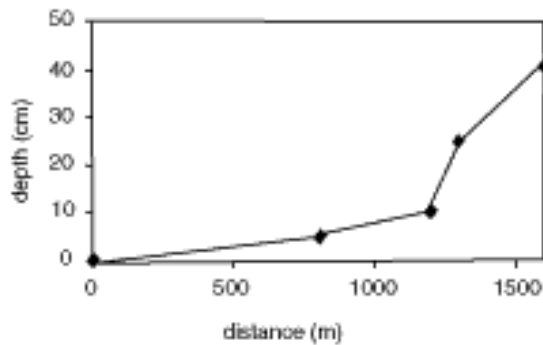


Figure 5.10: Averaged snow depths along the transect onn toward Glacier. Snowline located at third data point at 200 m.



Figure 6.1: Effect of a SAR beam scattering off specular surfaces of different incidence angles (ASF website).

72

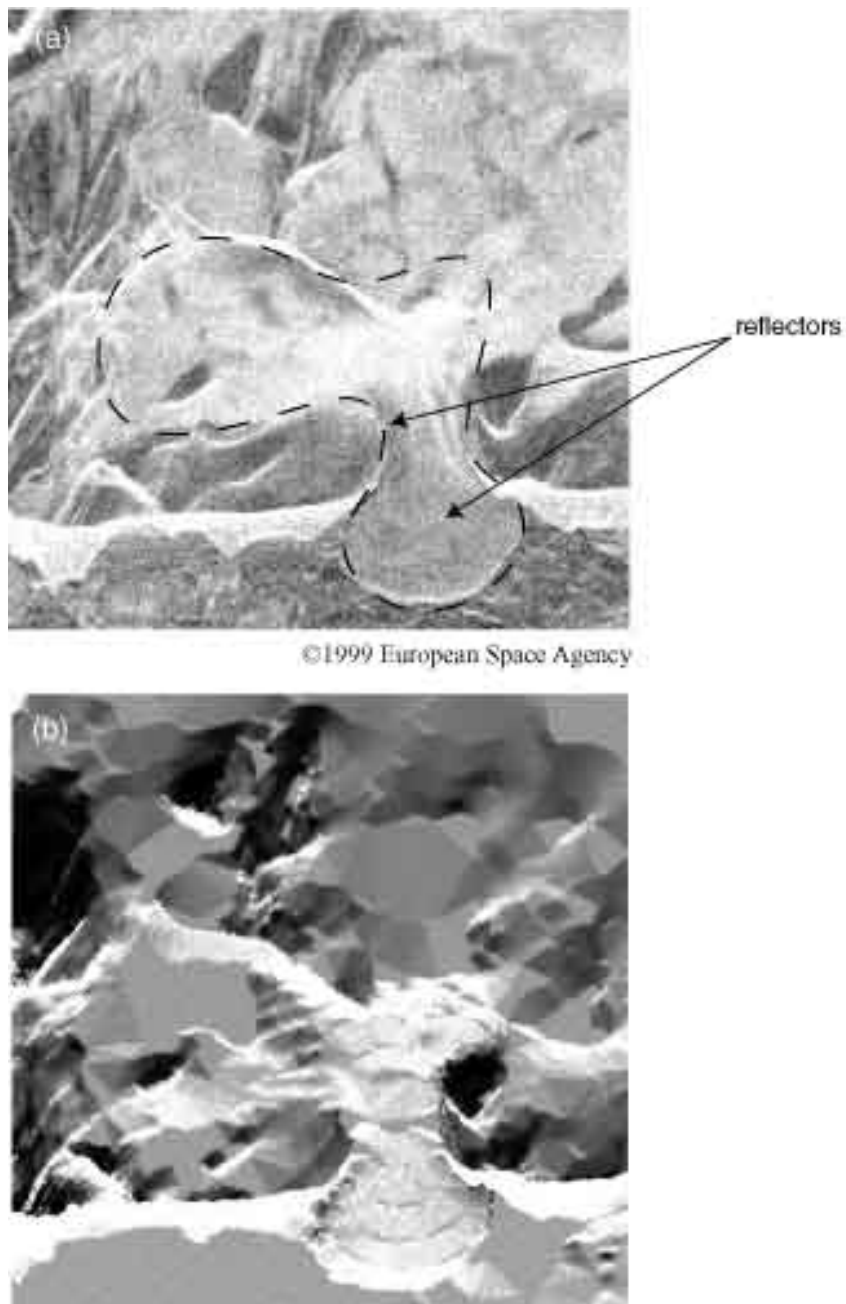


Figure 6.2: Intermediate terrcorr images of Commonwealth Glacier and surrounding area. (a) Preprocessed SAR image. Approximate outline of glacier shown in dashed line. (b) Simulated SAR image. The image is "blocky" because it is created from the 30 m resolution DEM.

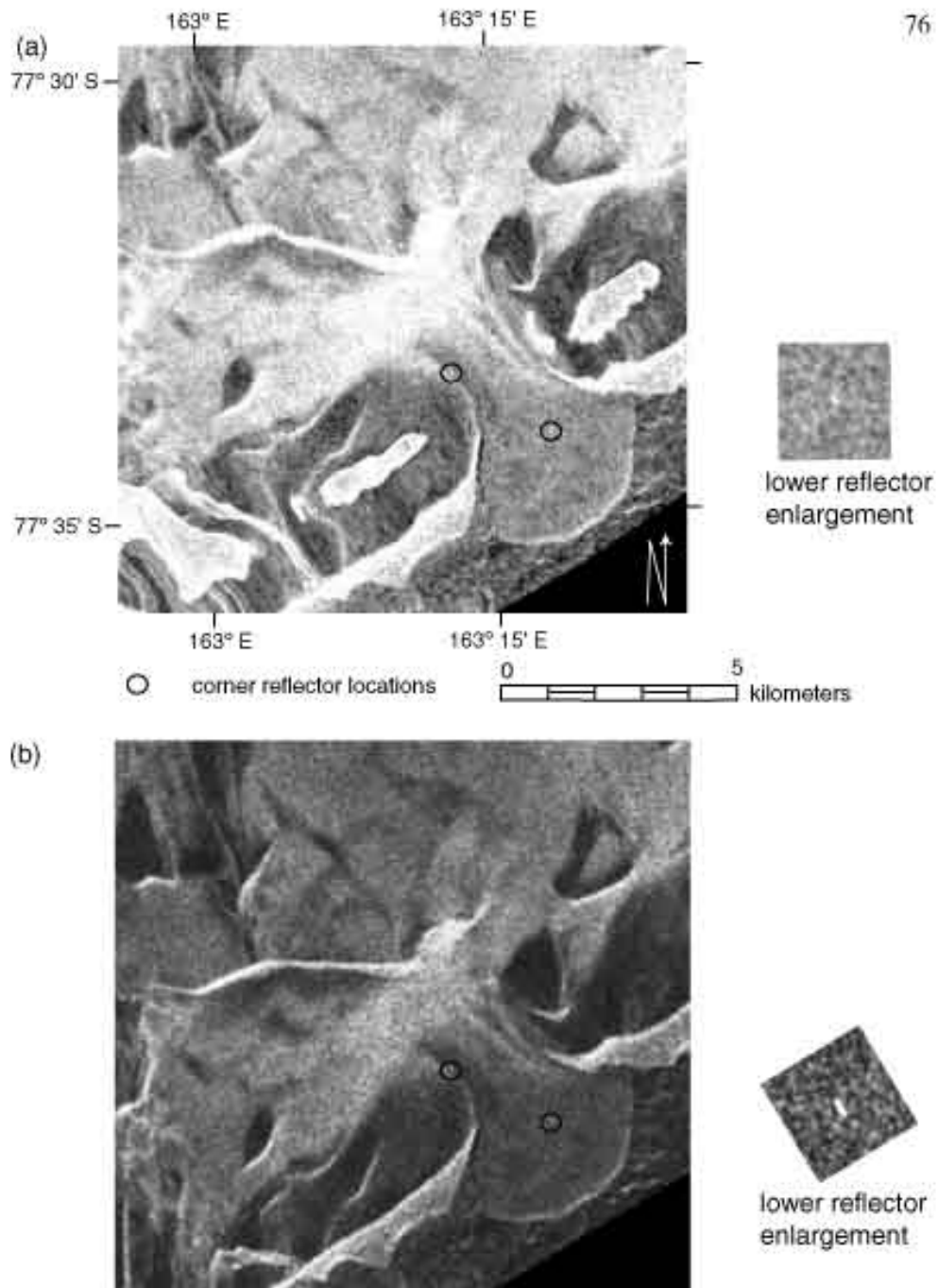


Figure 6.3: Auto terrain corrected (a) and uncorrected image (b) comparison ERS-2 SAR of Commonwealth Glacier and surrounding area. Both images are approximately same scale. Both images ©1999 European Space Agency.

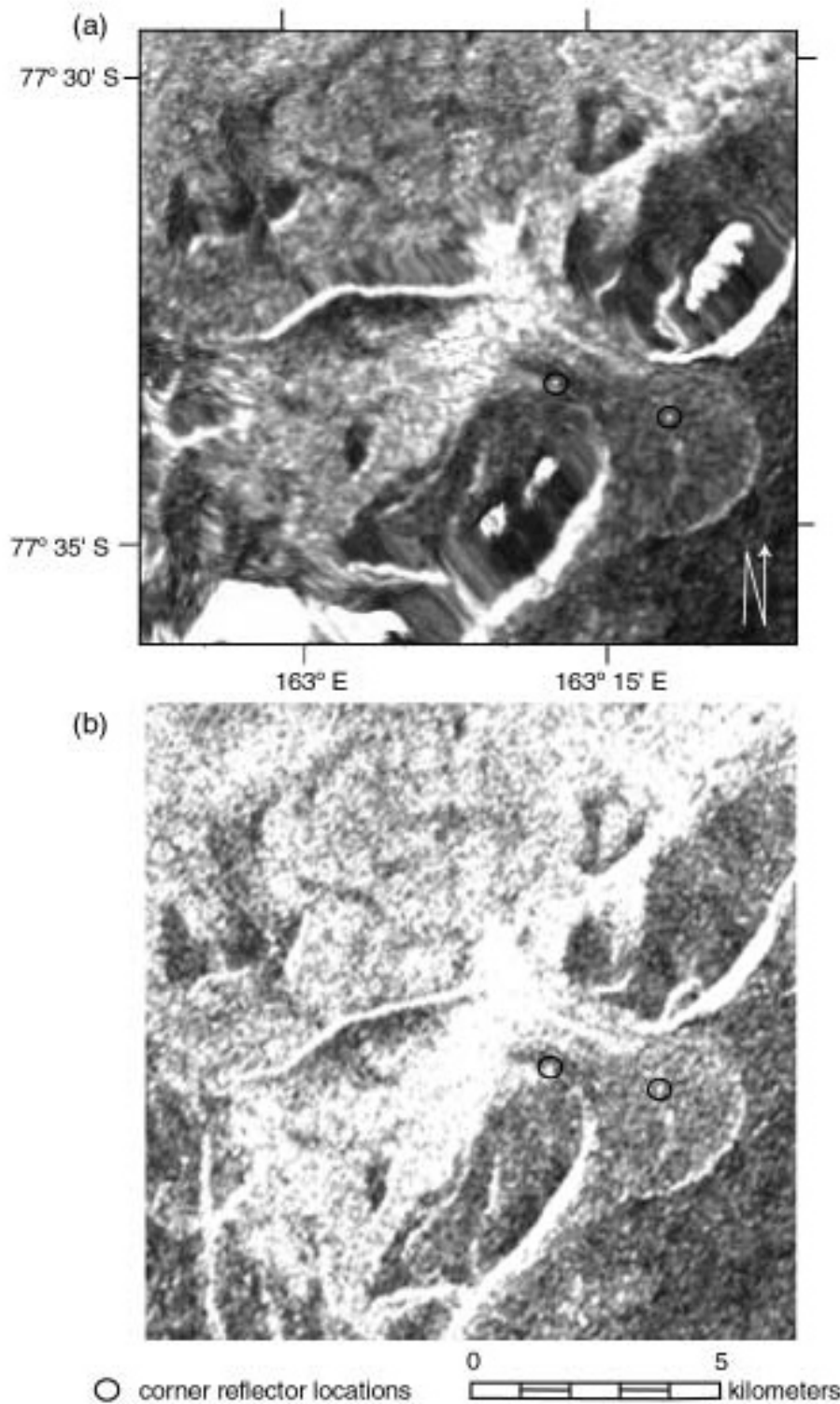


Figure 6.4: (a) Terrain corrected Radarsat ScanSAR of Commonwealth Glacier and surrounding area. (b) Uncorrected Radarsat ScanSAR of approximately same area. Scales are approximately the same. Both images ©1999 Canadian Space Agency.

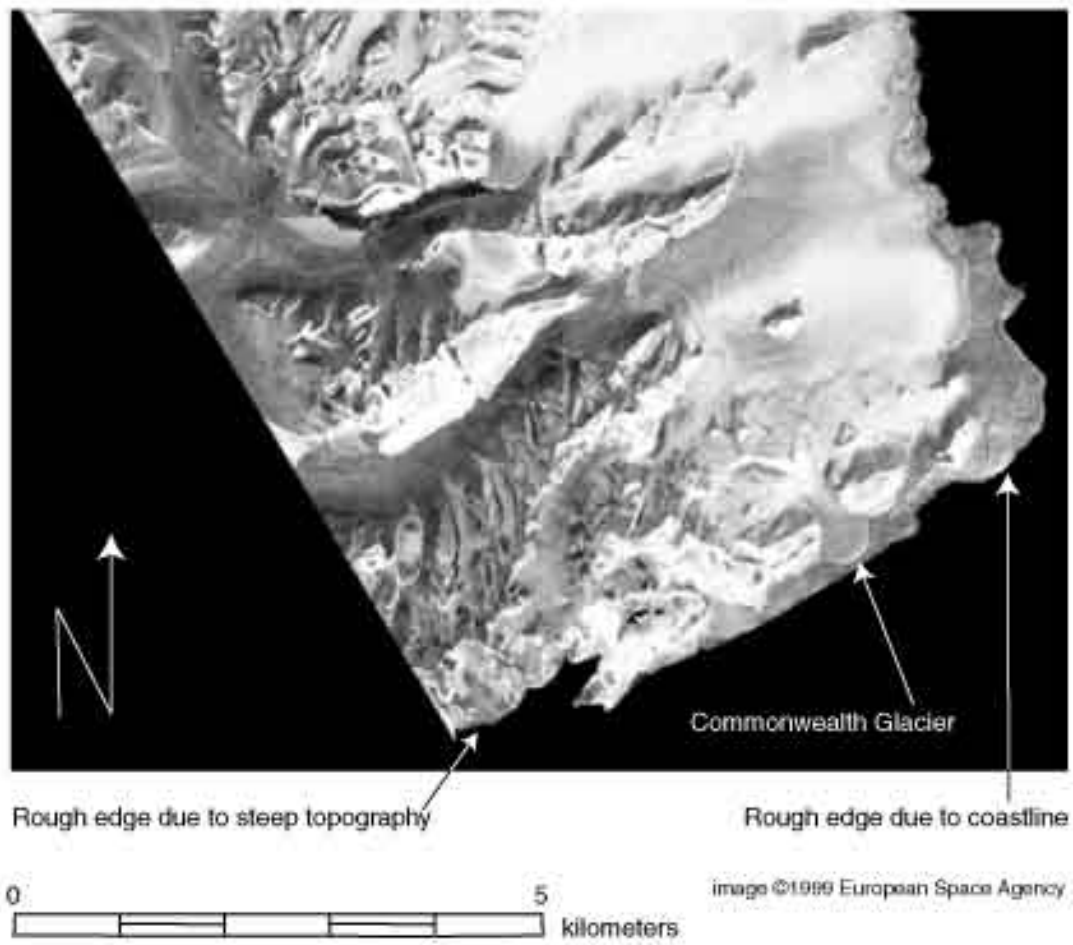


Figure 6.5: ERS-2 terrain corrected SAR.

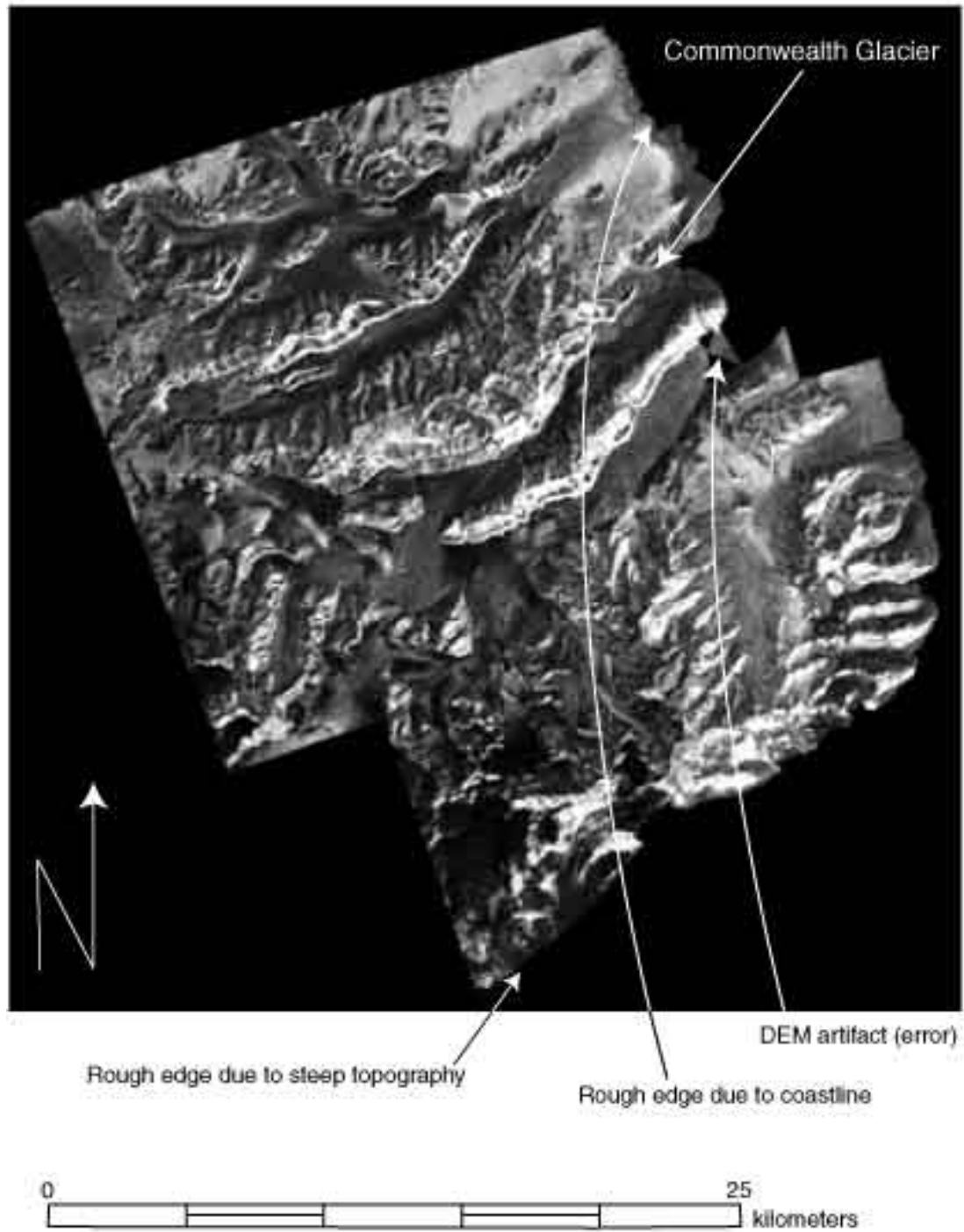


Image ©1999 Canadian Space Agency

Figure 6.6: Radarsat terrain corrected SAR.

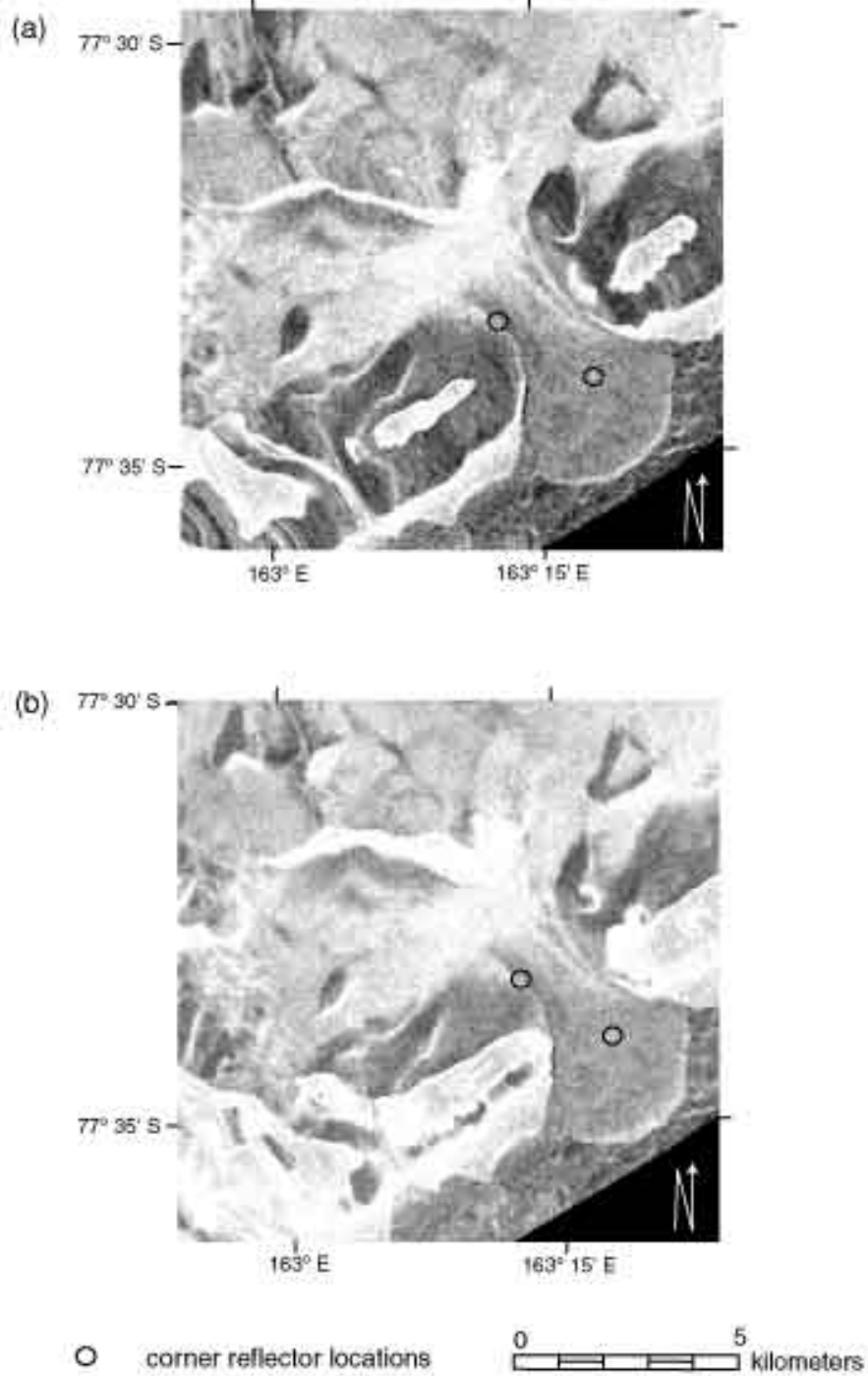


Figure 6.7: (a) Auto-correlation and (b) manual-correlation terrain correction of Commonwealth Glacier and surrounding area. Scales are approximately the same. Both images ©1999 European Space Agency.

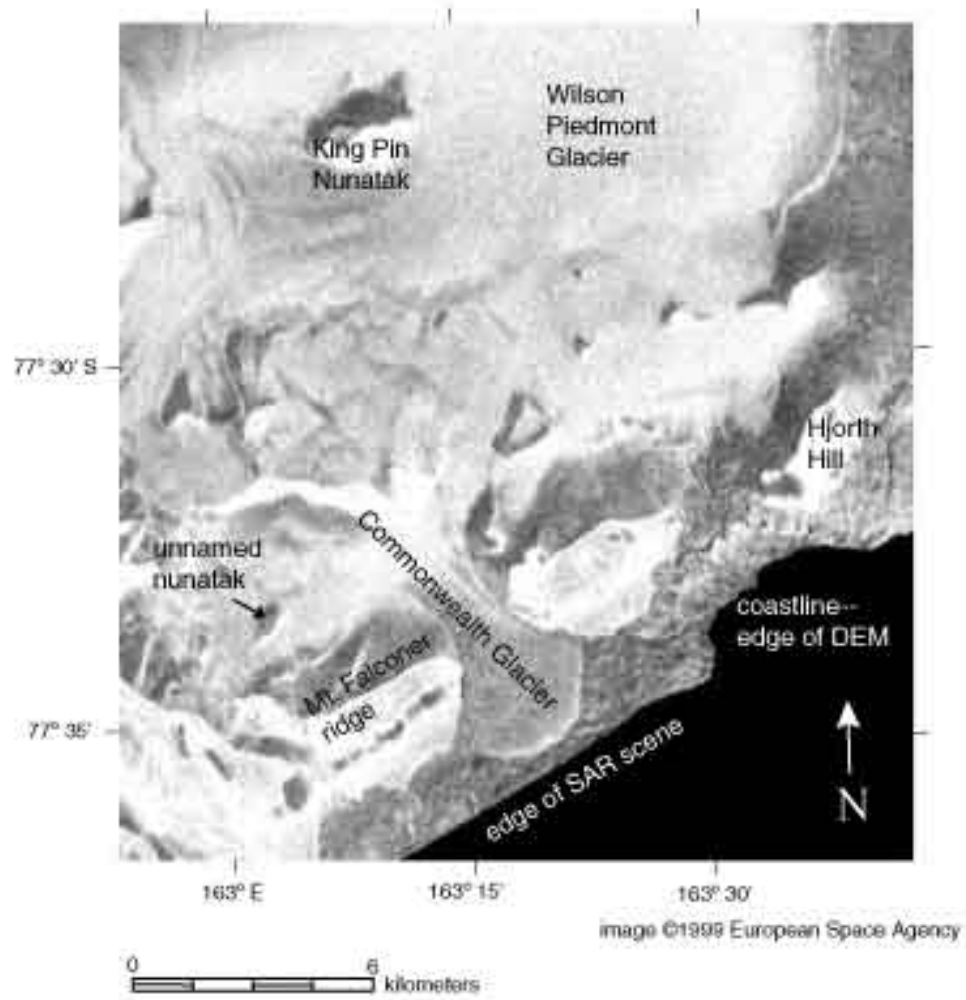


Figure 6.8: ERS-2 SAR of Commonwealth Glacier and surrounding area.

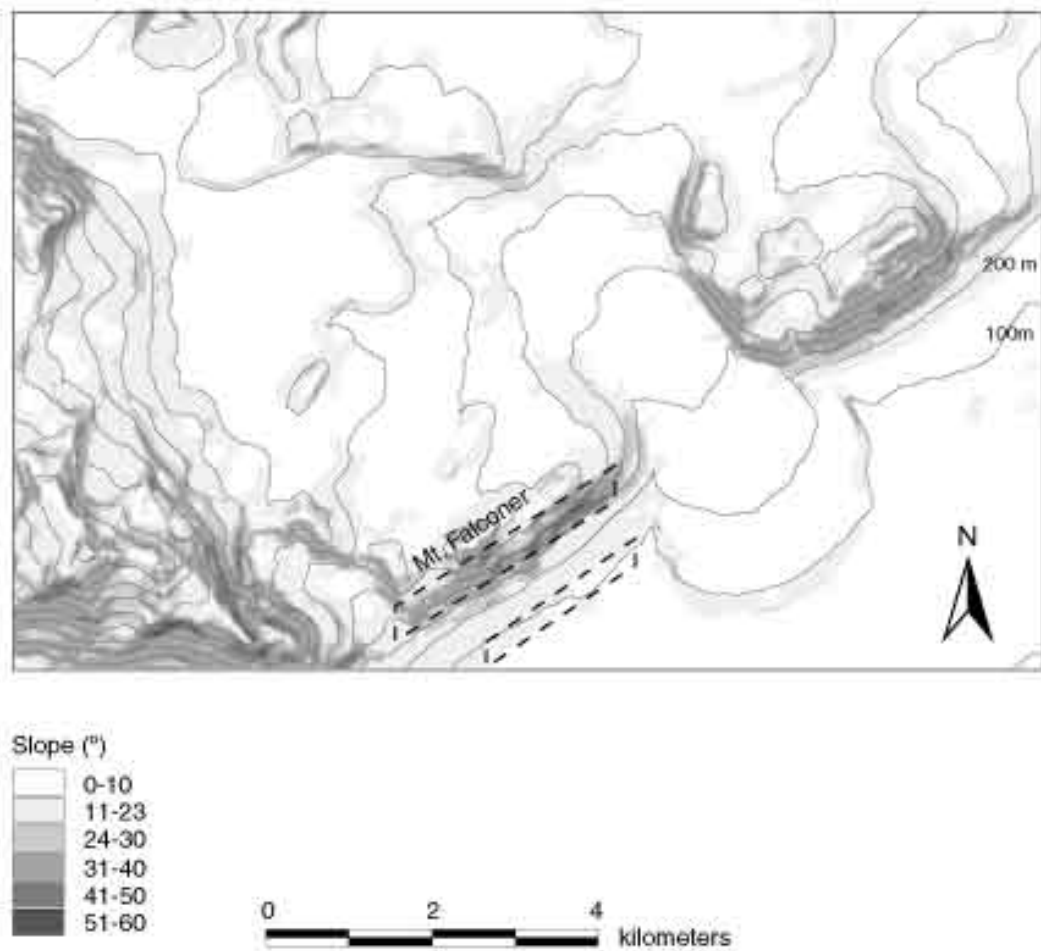


Figure 6.9: Slope and elevations (from DEM) of Commonwealth Glacier. Dashed box indicates the two bright bands on the manually corrected ERS-2 SAR image.

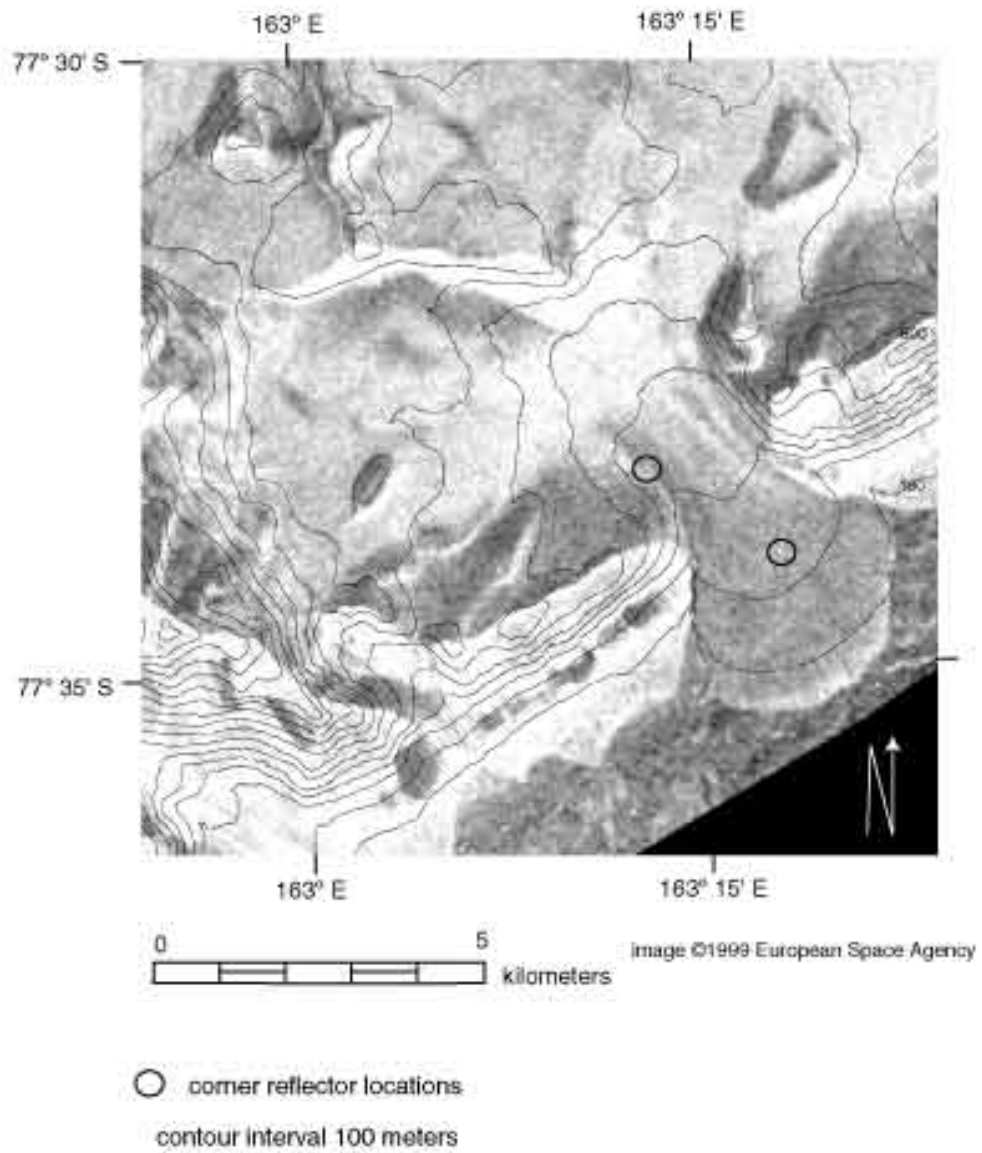


Figure 6.10: ERS-2 manually-correlated SAR image of Commonwealth Glacier with elevation contours.

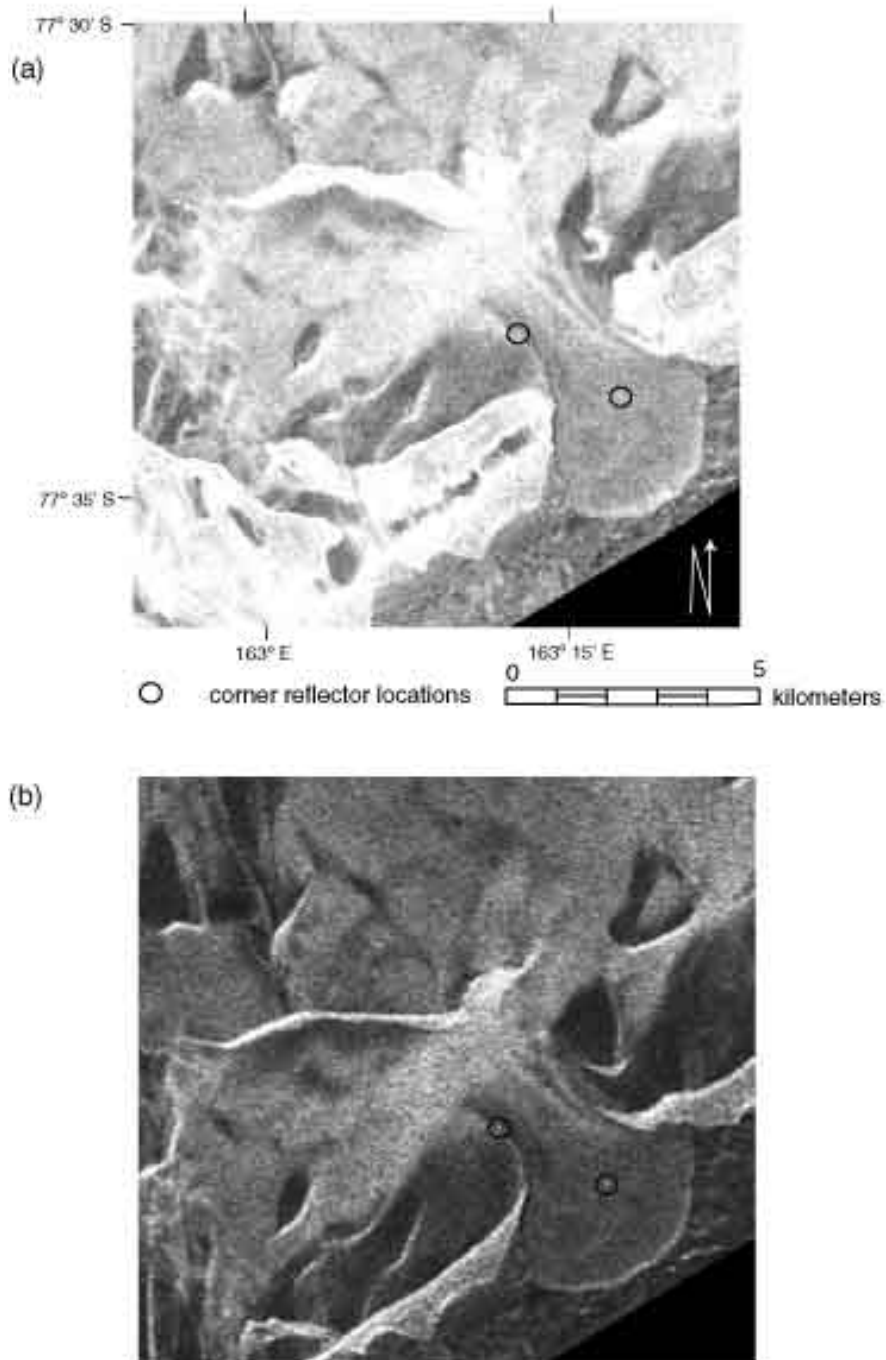


Figure 6.11: (a) Manually-correlated and (b) uncorrected ERS-2 SAR of Commonwealth Glacier and surrounding area. Both images are approximately same scale. Both images ©1999 European Space Agency.

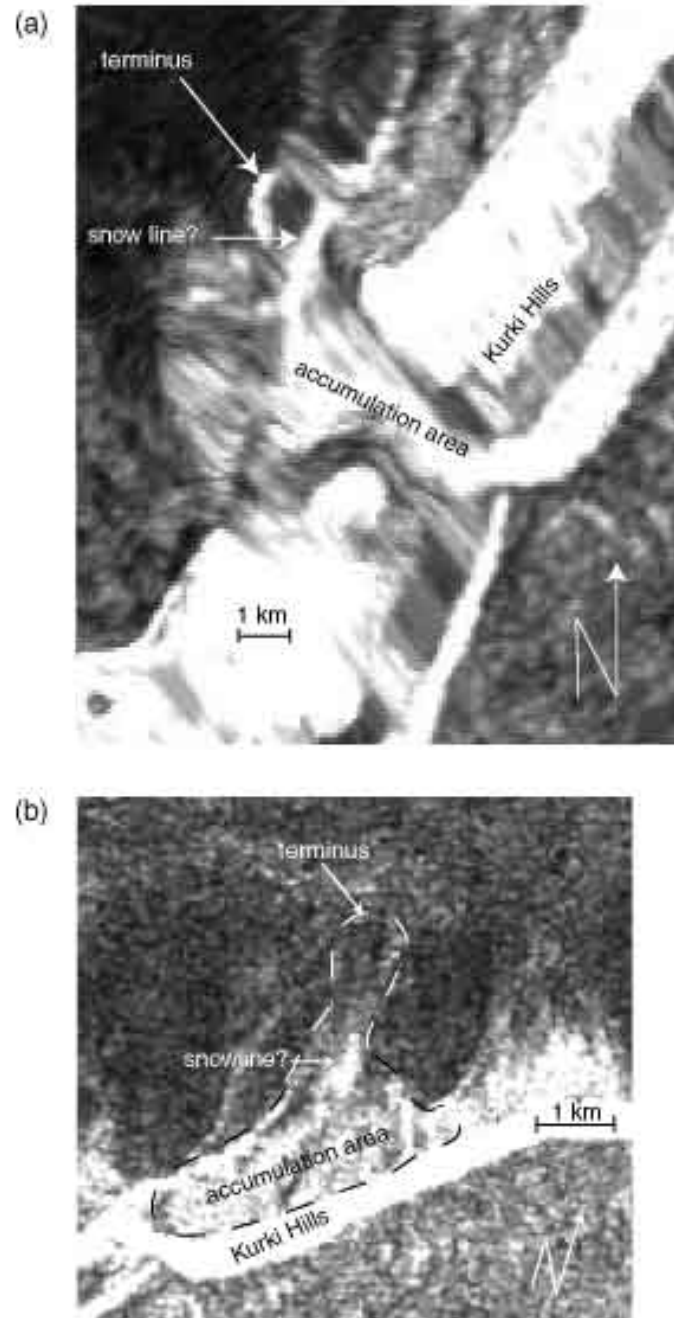
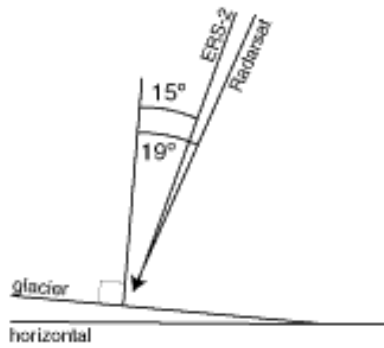


Figure 6.12: (a) Terrain corrected and (b) uncorrected Radarsat ScanSAR of Howard Glacier. Dashed line indicates approximate outline of glacier. Both images ©1999 Canadian Space Agency.

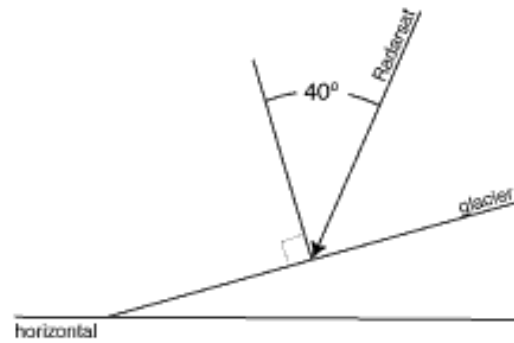
Commonwealth Glacier



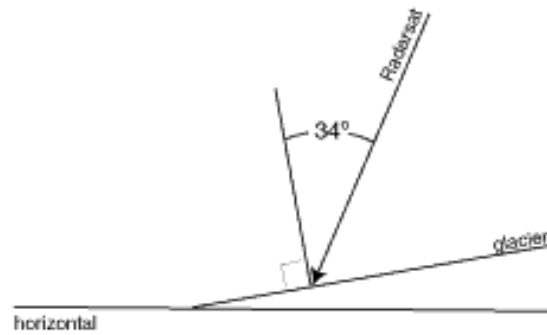
5° average glacier slope
(0° - 10° slope)

Howard Glacier

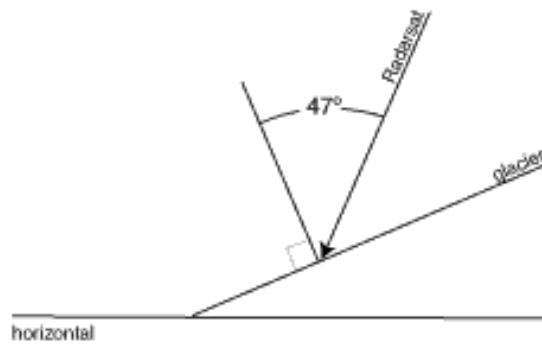
97



16° average glacier slope



10° minimum glacier slope



23° maximum glacier slope

Figure 6.13: SAR local incidence angles on Commonwealth (left column) and Howard (right column) Glaciers.

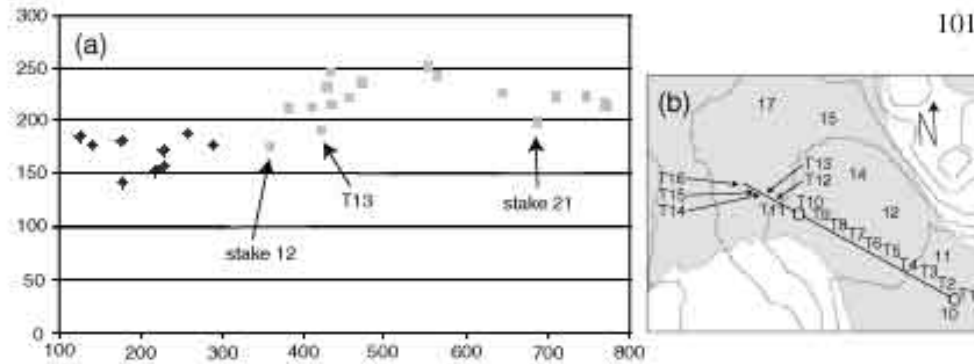


Figure 7.2: (a) SAR image brightness relative to surface elevation on Commonwealth Glacier. Black diamonds represent surfaces in the ablation area, and gray squares represent ones in the accumulation area. SAR brightness from 1/15/1999 ERS-2 terrain corrected SAR. (b) Figure 5.8 reference map.

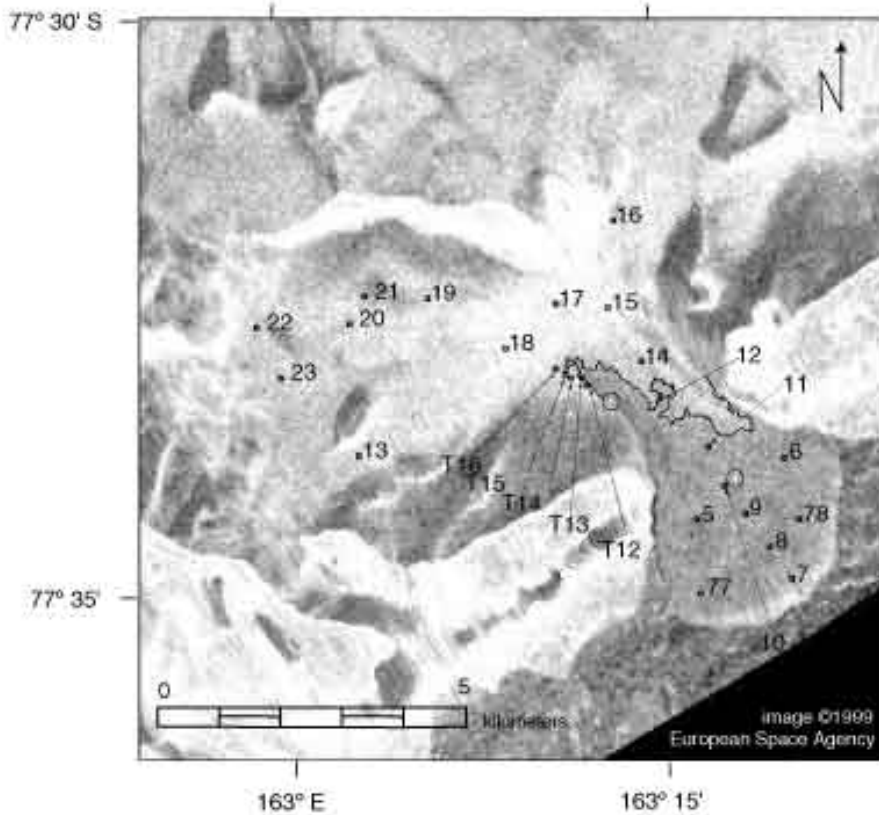


Figure 7.3: Commonwealth Glacier ERS-2 SAR 1/15/1999 snow measurement locations. Circles indicate reflector locations, and line is SAR snowline.

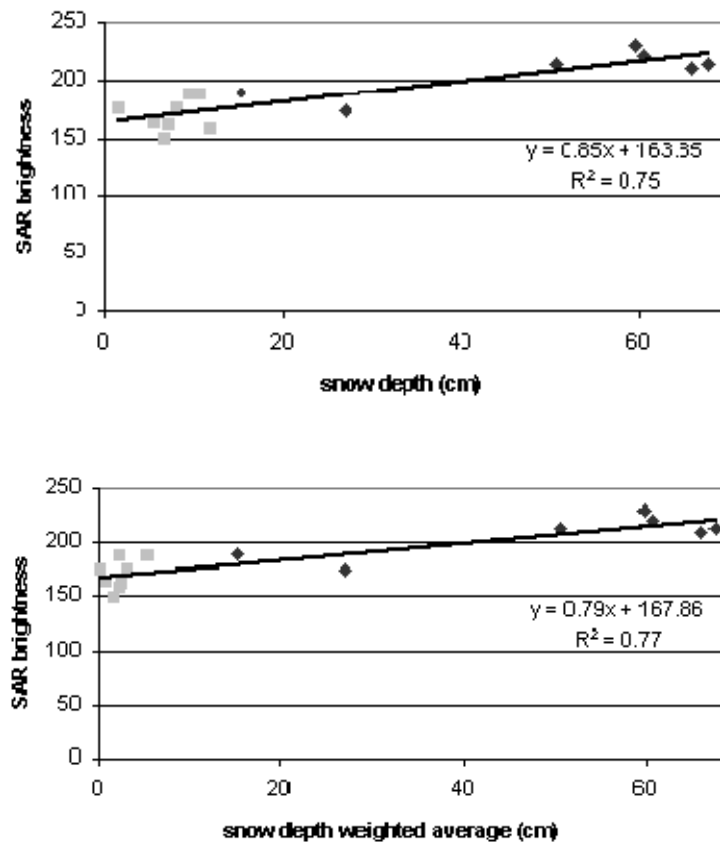


Figure 7.4 ERS-2 brightness to snow depth

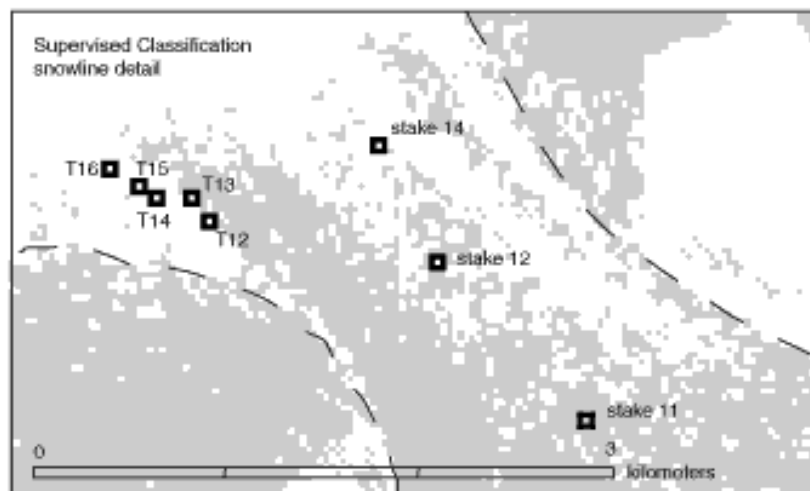
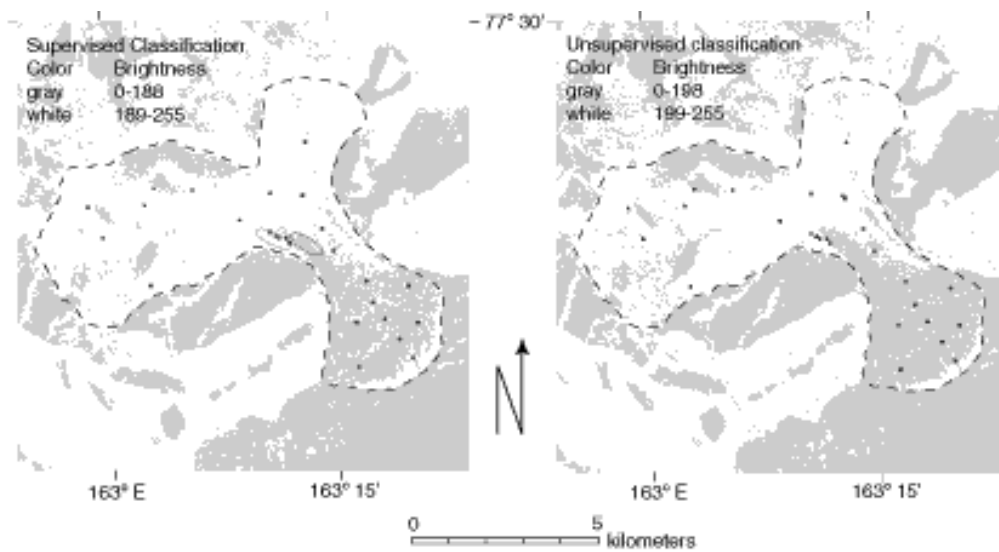


Figure 7.6: Commonwealth Glacier ERS-2 SAR 1/15/1999 snowline classification maps. Approximate outline of glacier shown in dashed line, within the glacier area, gray pixels are classified as ice and white pixels as snow. Ovals on supervised classification image are the training areas locations. Both images ©1999 European Space Agency.

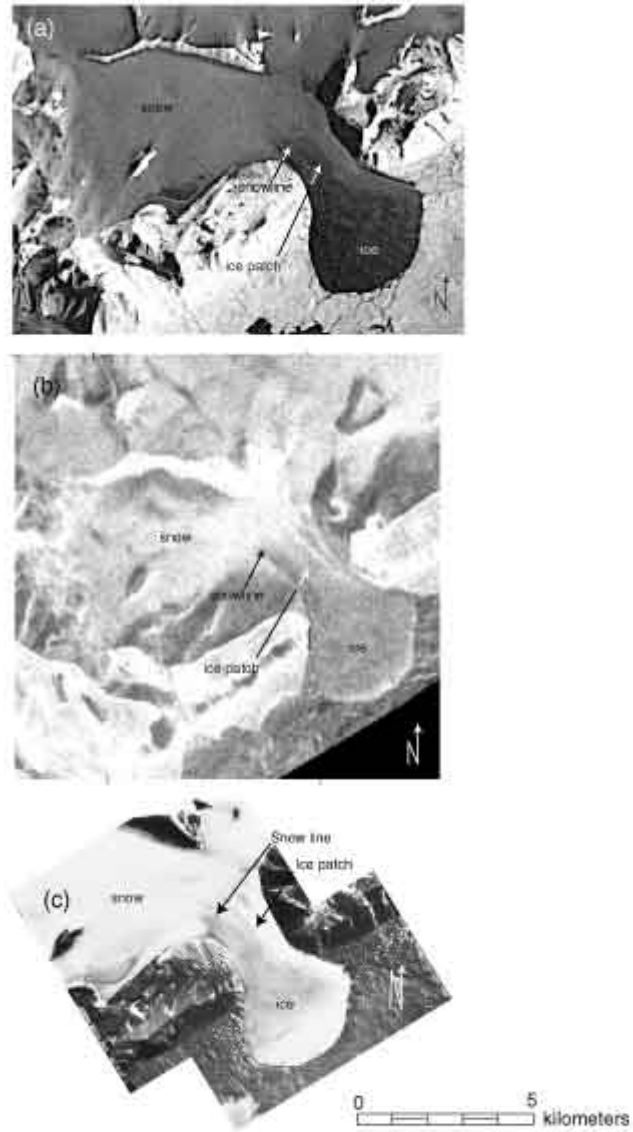


Figure 7.7: Comparison of Commonwealth Glacier. (a) January 6, 1993 Landsat 6 band 4 (J.C. Thomas, USGS). (b) ERS-2 January 15, 1999 ©1999 European Space Agency. (c) Two merged aerial photos taken November 1993 (USGS).

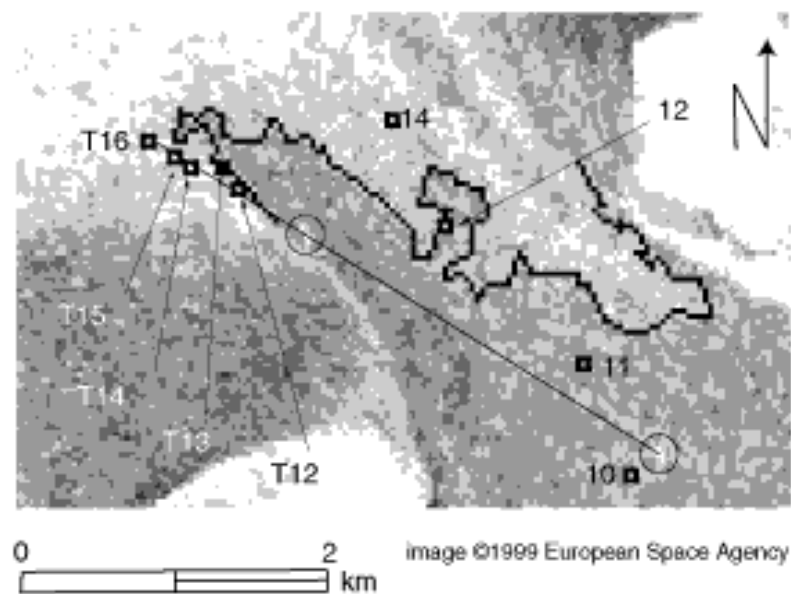
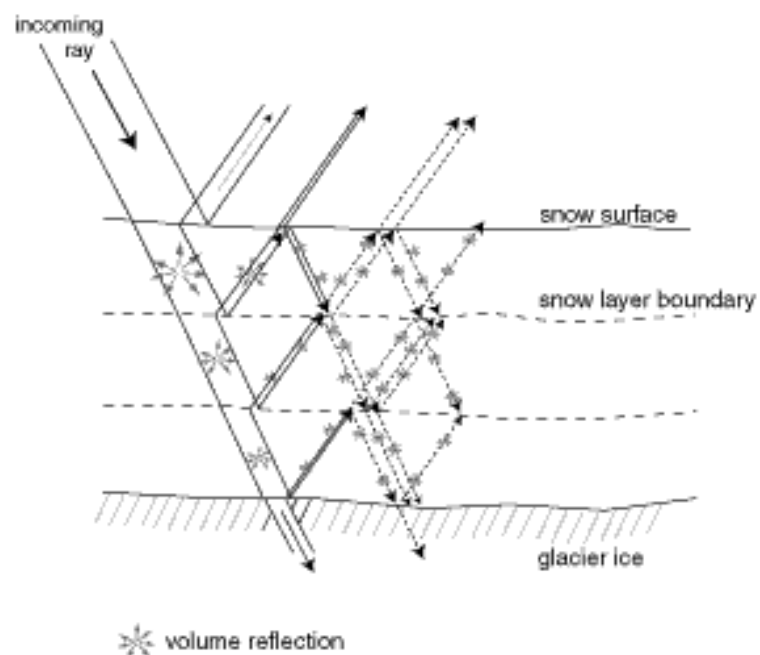


Figure 7.8: Detail of snowline on Commonwealth Glacier ERS-2 SAR 1/15/1999. Circles indicate reflectors, straight line is transect, and irregular line is SAR snowline.



113

Figure 7.9: Enhanced volume backscatter.

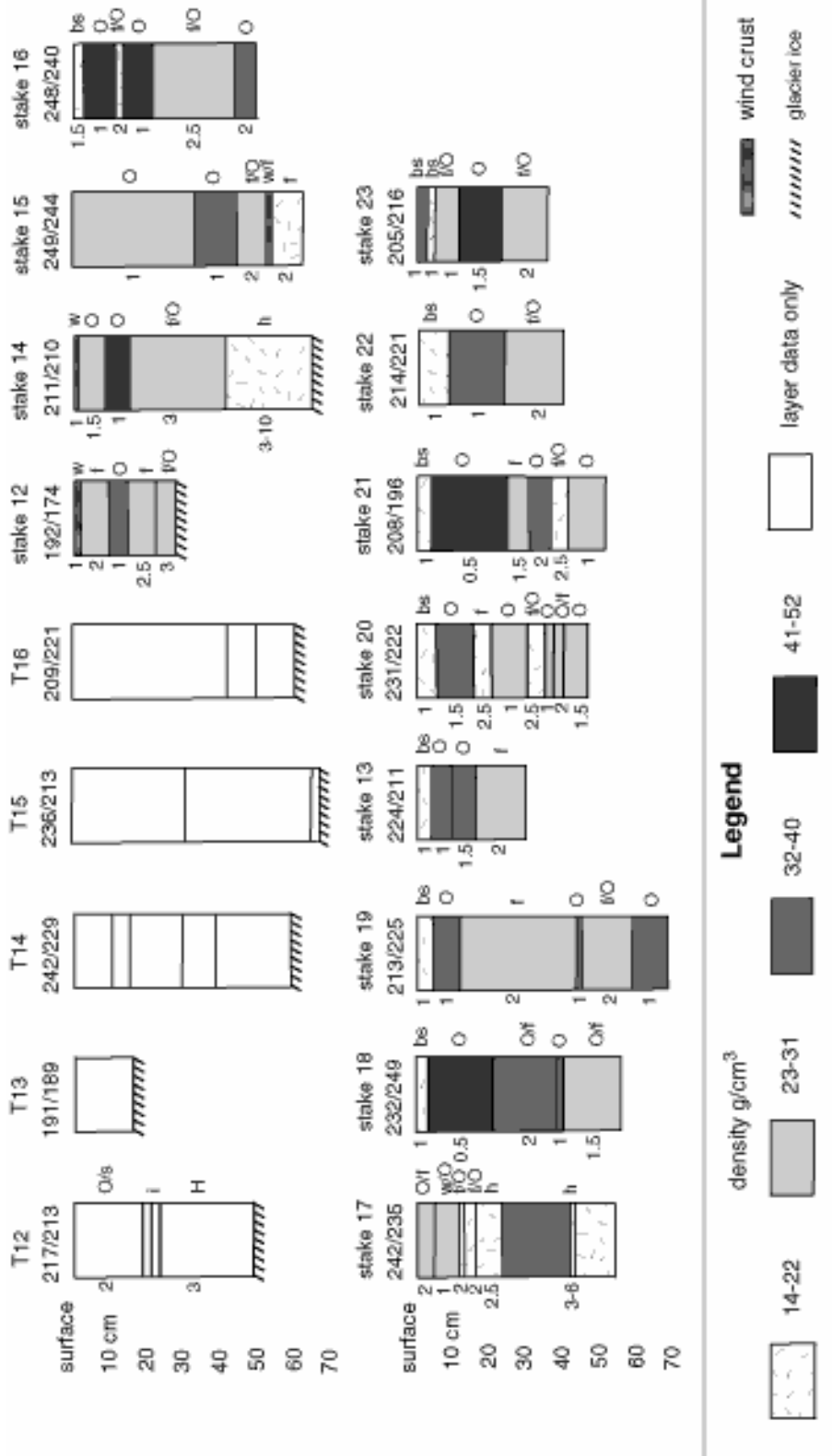


Figure 7.10: Commonwealth Glacier snow stratigraphy measured 1/19 to 1/20/99. Numbers to the far left indicate depth of layers. Grain size (mm) to the immediate left of layer. SAR brightness on top of each layer: first number is the exact location, the second number is a four-pixel average. T12, T13, T14, T15, T16, stake 12, and stake 14 show layers to glacier ice, all other locations to previous year snow surface. Mechanical structure to the right of layer: f—facets, O—rounds, w—wind crust, h—hoar, bs—broken stella, H—hoar, i—ice.

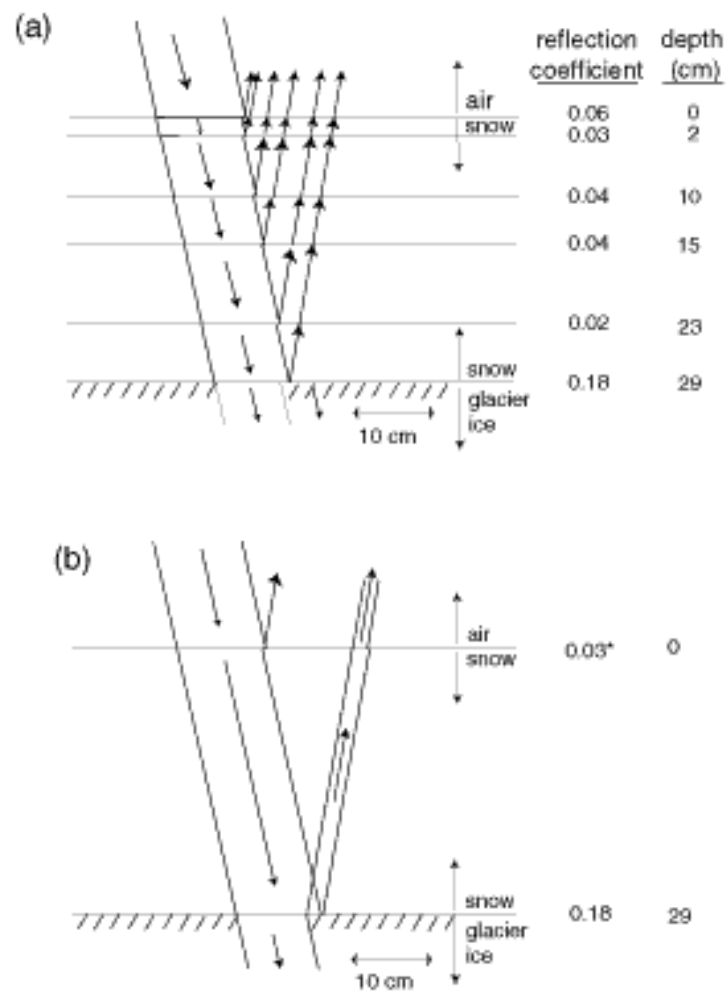


Figure 7.11: Reflections and refractions of the SAR beam at stake 12. Arrows indicate less than 10% of original power. (a) All layers recorded at stake 12. (b) Estimated refractions and reflections at stake 12 if there were no intervening layers.

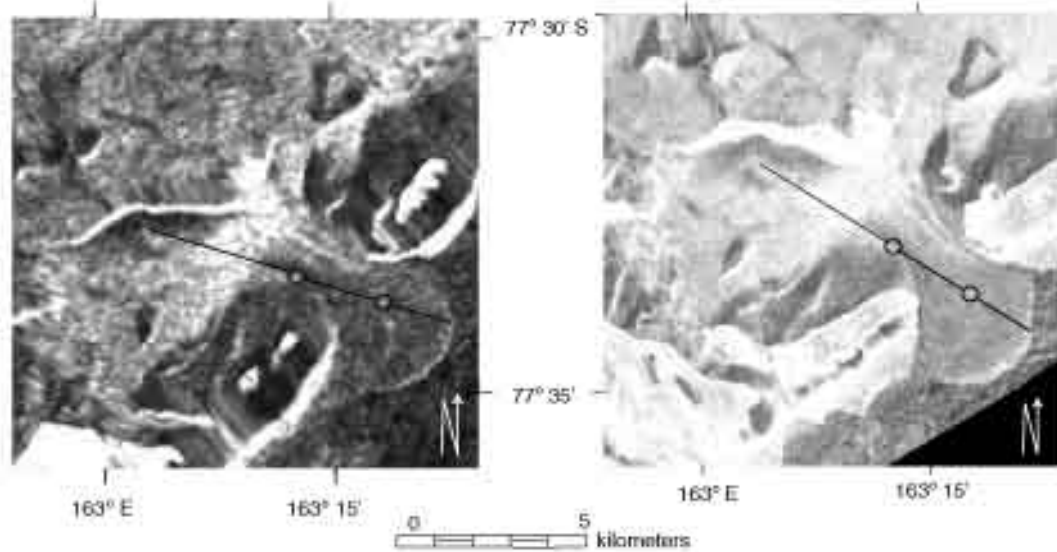


Figure 7.13: Terrain corrected SAR image transect locations. (a) 1/19/1999 Radarsat ScanSAR (image ©1999 Canadian Space Agency), (b) 1/15/1999 ERS-2 (image ©1999 European Space Agency). Reflector locations indicated by circles, transect indicated by line.

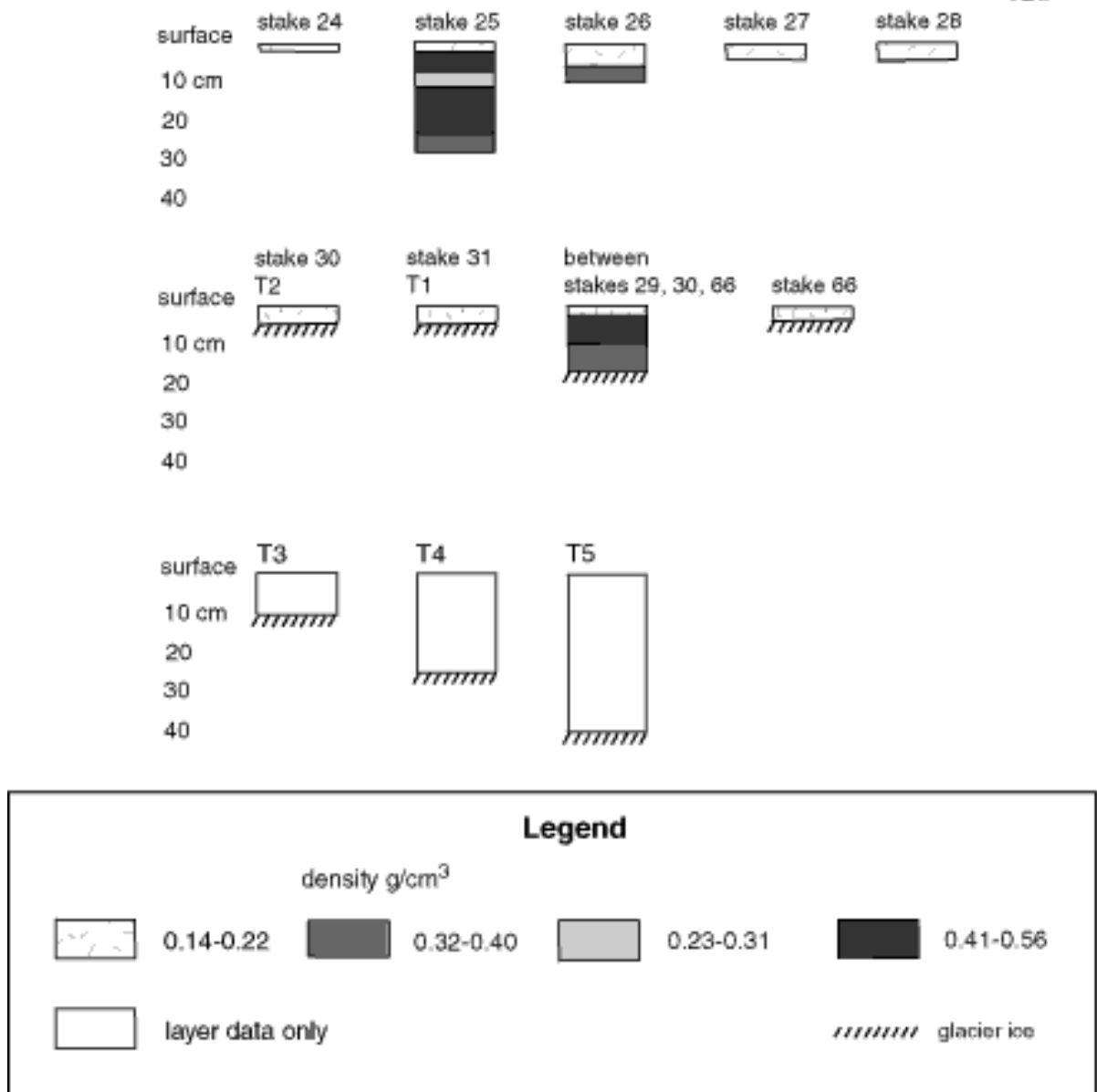


Figure 7.16: Howard Glacier snow layers graph. All measurements to previous year snow surface or glacier ice. Sites 30, 31, 66 are in ablation area. T3-T5 depths determined with probe rod and no layer data taken.

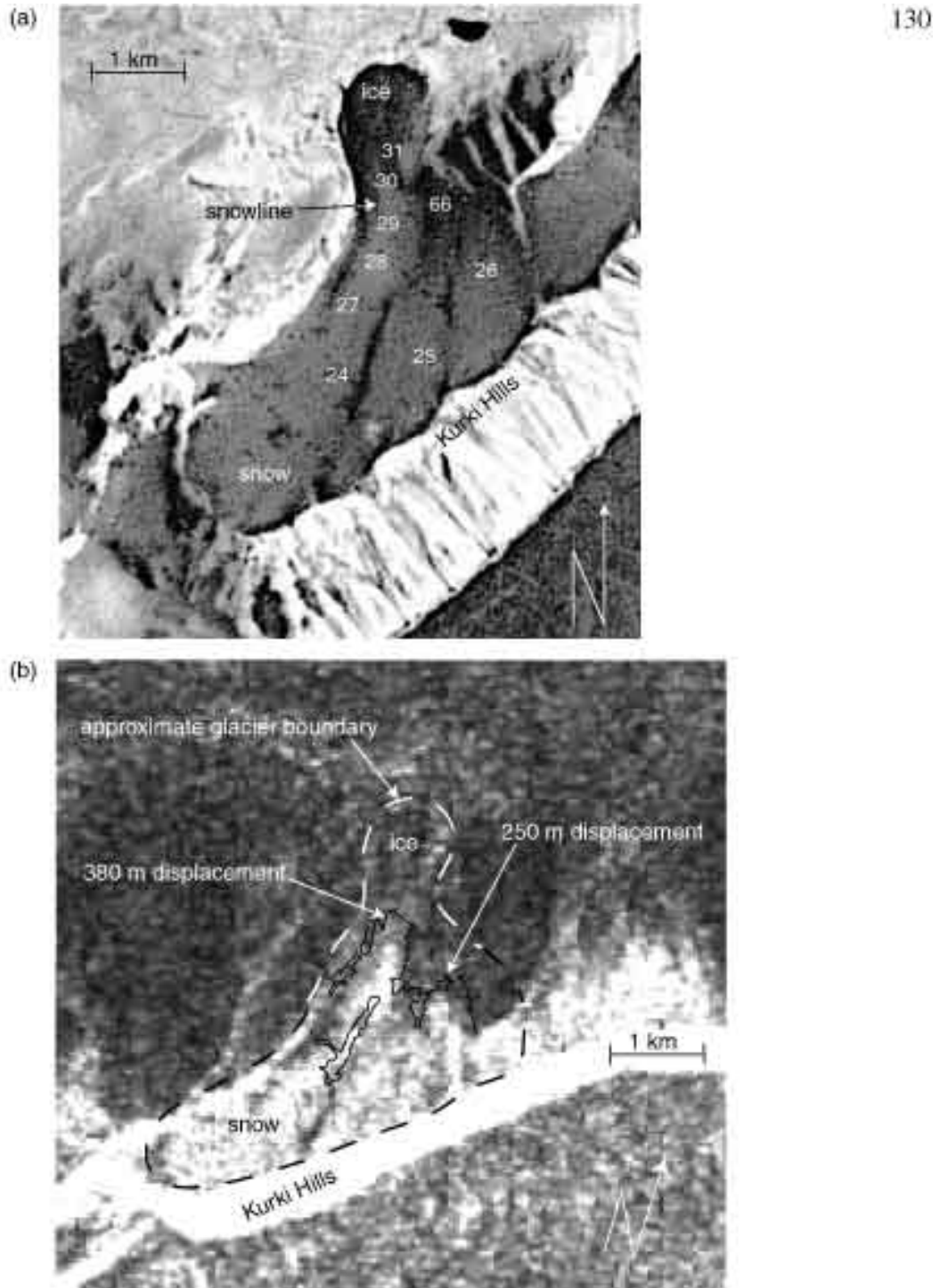


Figure 7.17: Landsat and Radarsat comparison of Howarth Glacier snowline.
 (a) January 6, 1993 Landsat 6 band 44 image, numbers indicate stake location
 (b) January 19, 1999 Radarsat ScanSAR. The black line is the snowline from (a) placed to a visual approximation of its proper location.

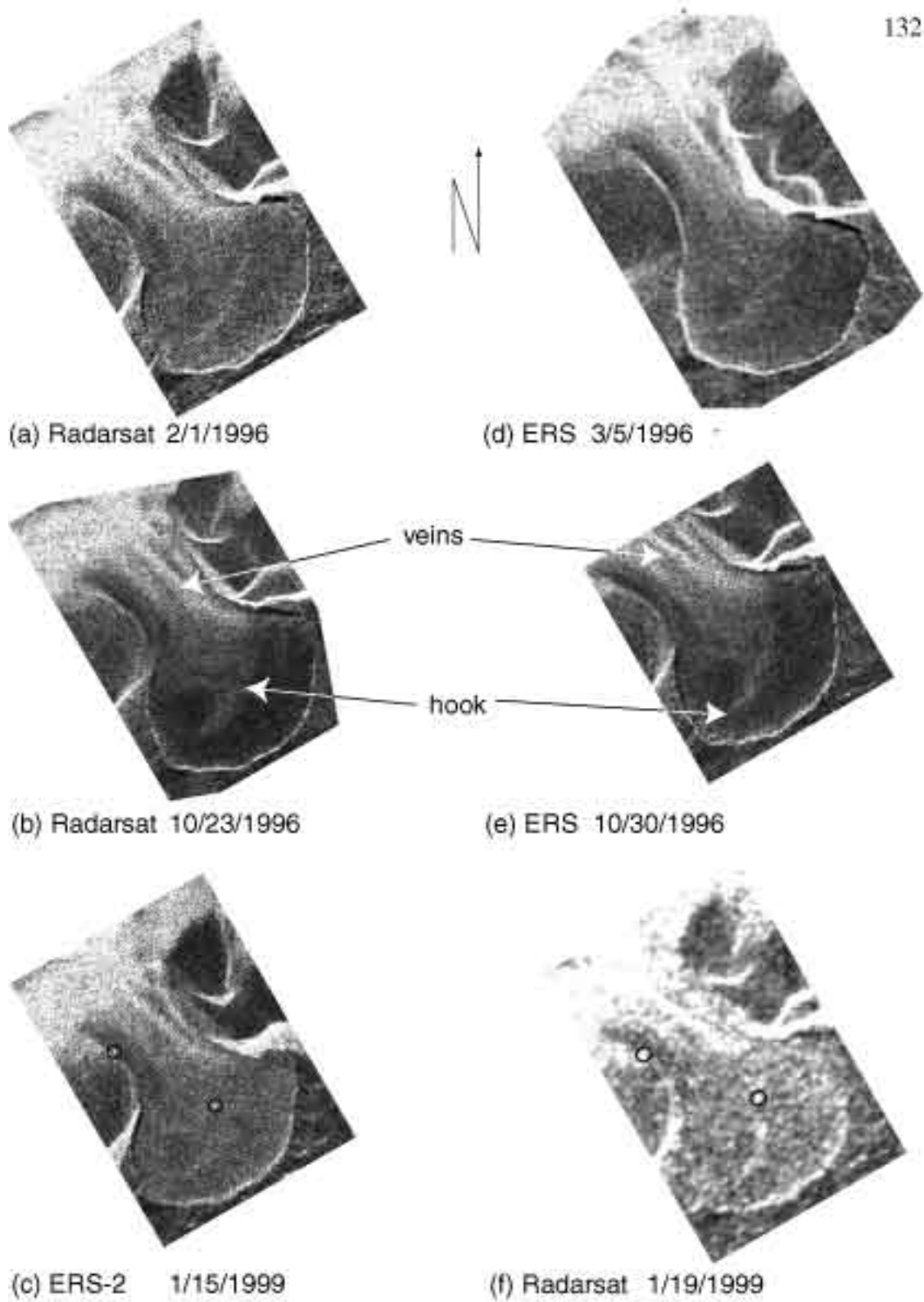


Figure 7.18: Six SAR views of Commonwealth Glacier. Reflectors highlighted with circles.

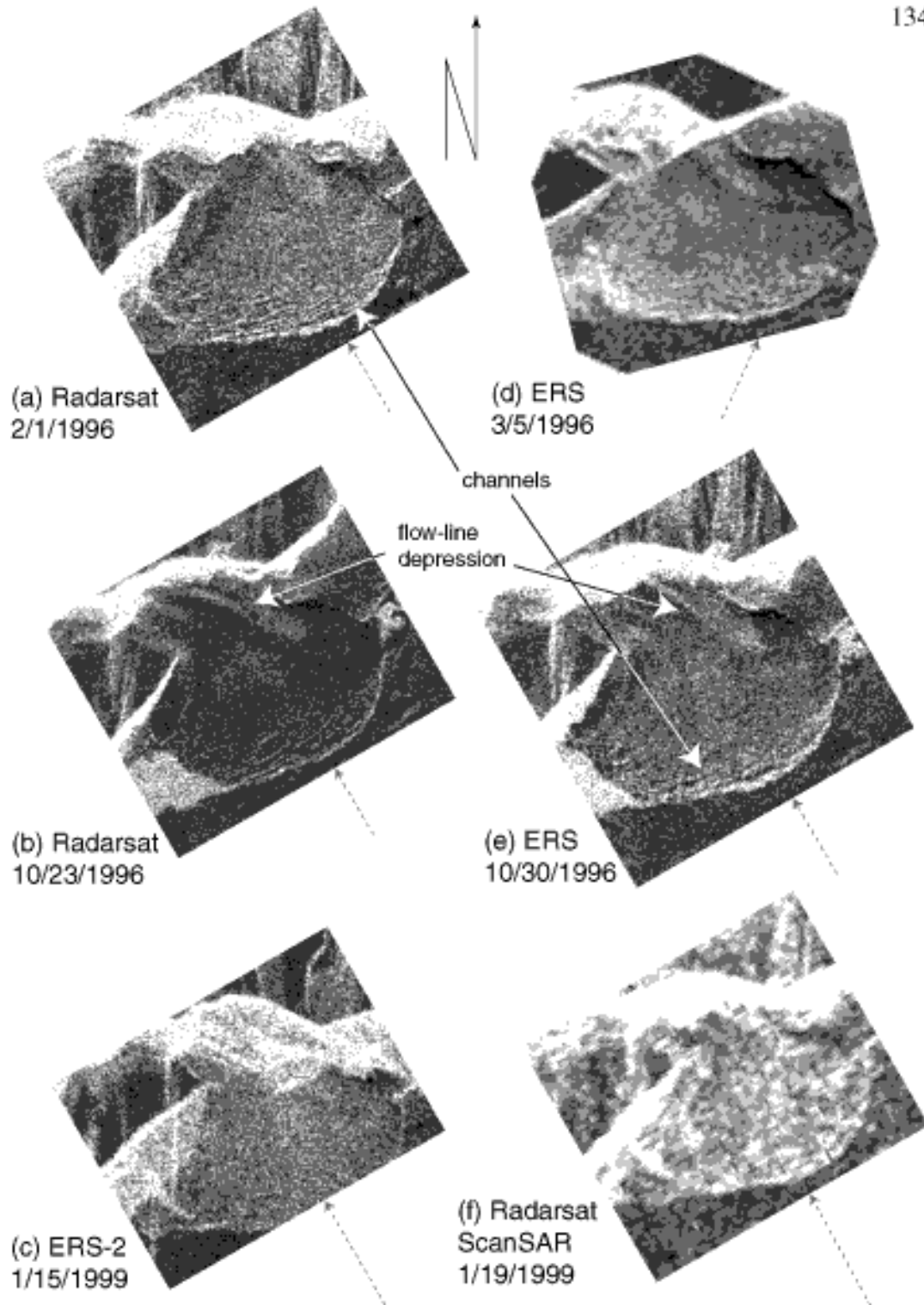


Figure 7.19: The terminus of Canada Glacier as represented by six uncorrected SAR images. Dashed arrow indicates SAR beam direction.

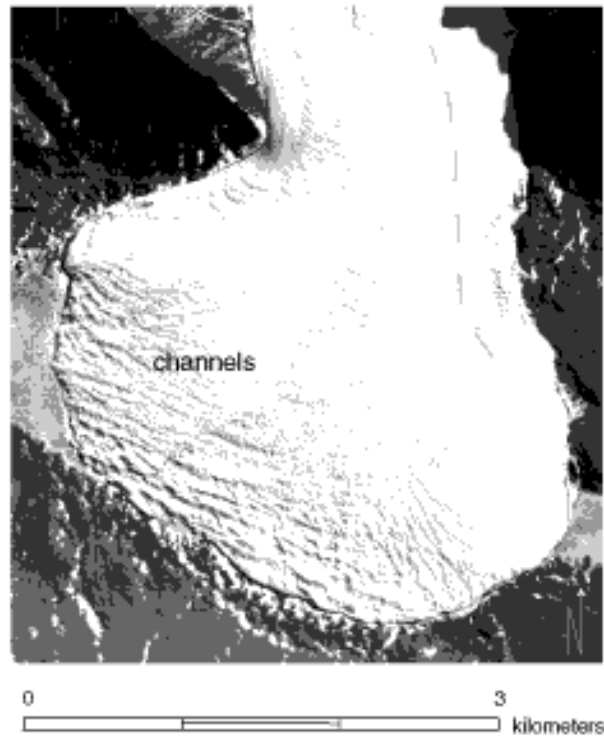


Figure 7.20: Aerial photo of Canada CGacier taken November 1993 (INSTARFF MCM LTER website). Dashed line shows approximate location of the flow line depression.

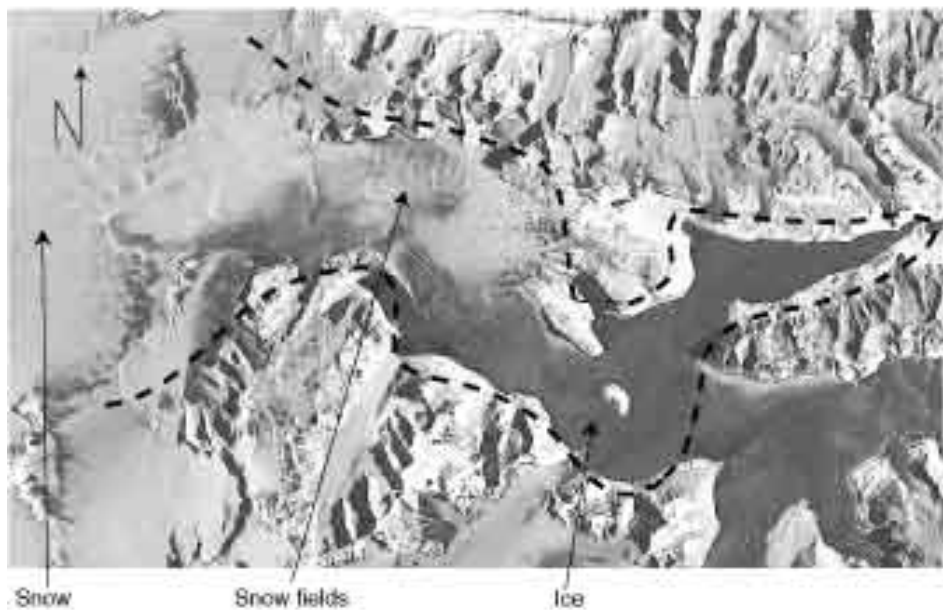
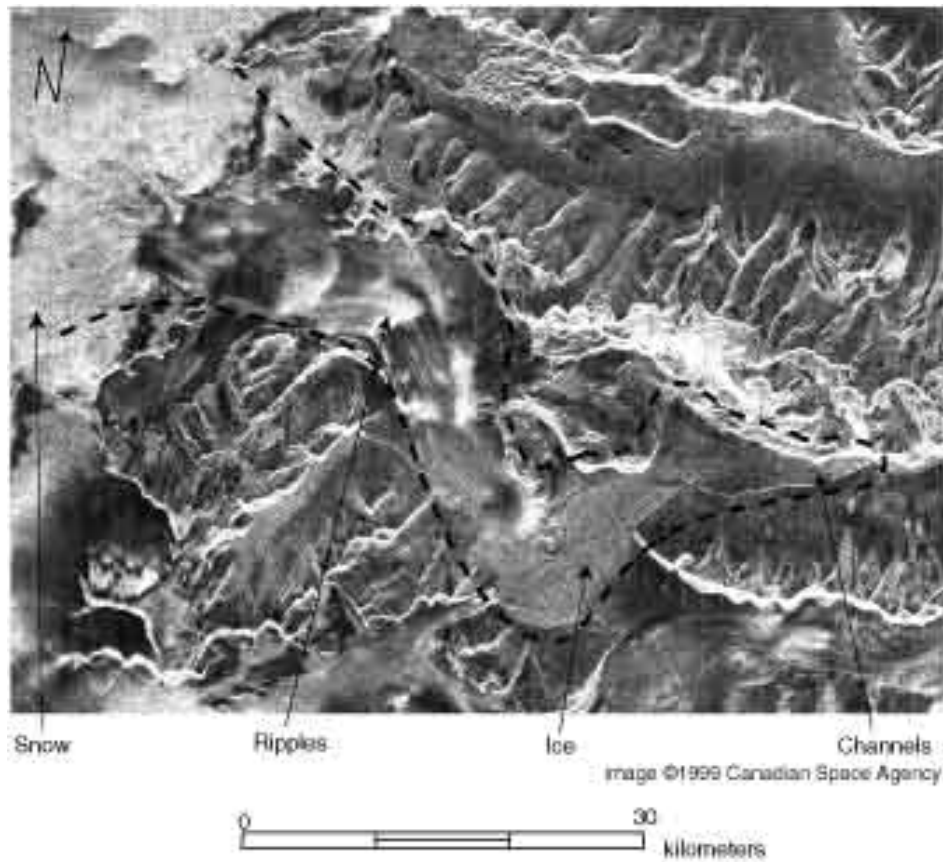
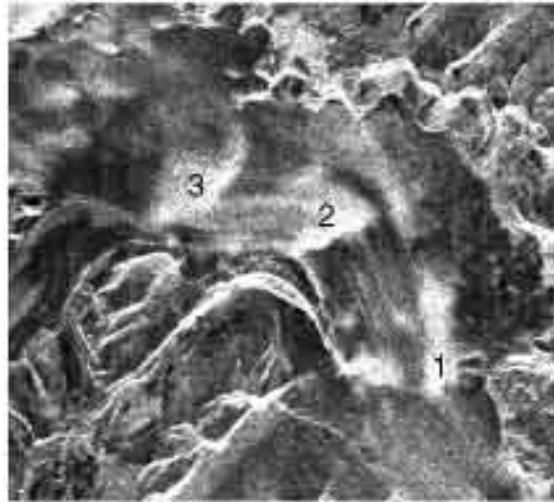


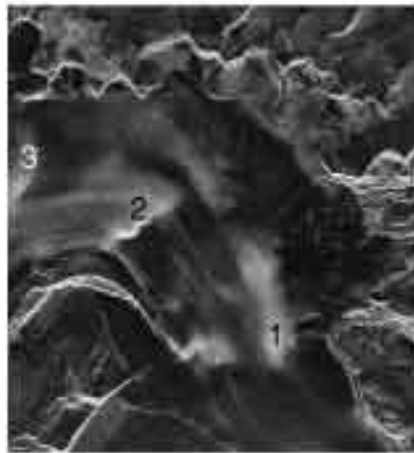
Figure 7.21: Images of Taylor Glacier. (a) January 19, 1999 Radarsat uncorrected ScanSAR. (b) January 6, 1993 Landsat 6 (band 4). Taylor Glacier indicated by dashed line.



Radarsat 2/1/1996



Radarsat ScanSAR 1/19/1999



Radarsat 10/23/1996



ERS 10/30/1996



Landsat 6, band 4 3/16/1999

Figure 7.22: Ripples on the upper Taylor Glacier as represented by four SAR images and one Landsat. Numbers on images indicate ripple number. (ERS 3/5/1996 and 1/19/1999 did not image Taylor Glacier ripples.)



Radarsat 2/1/1996



ERS 3/5/1996



Radarsat 10/23/1996



ERS 10/30/1996



Radarsat 1/19/1999



Figure 7.23: Lower Taylor Glacier as represented by five SAR images.

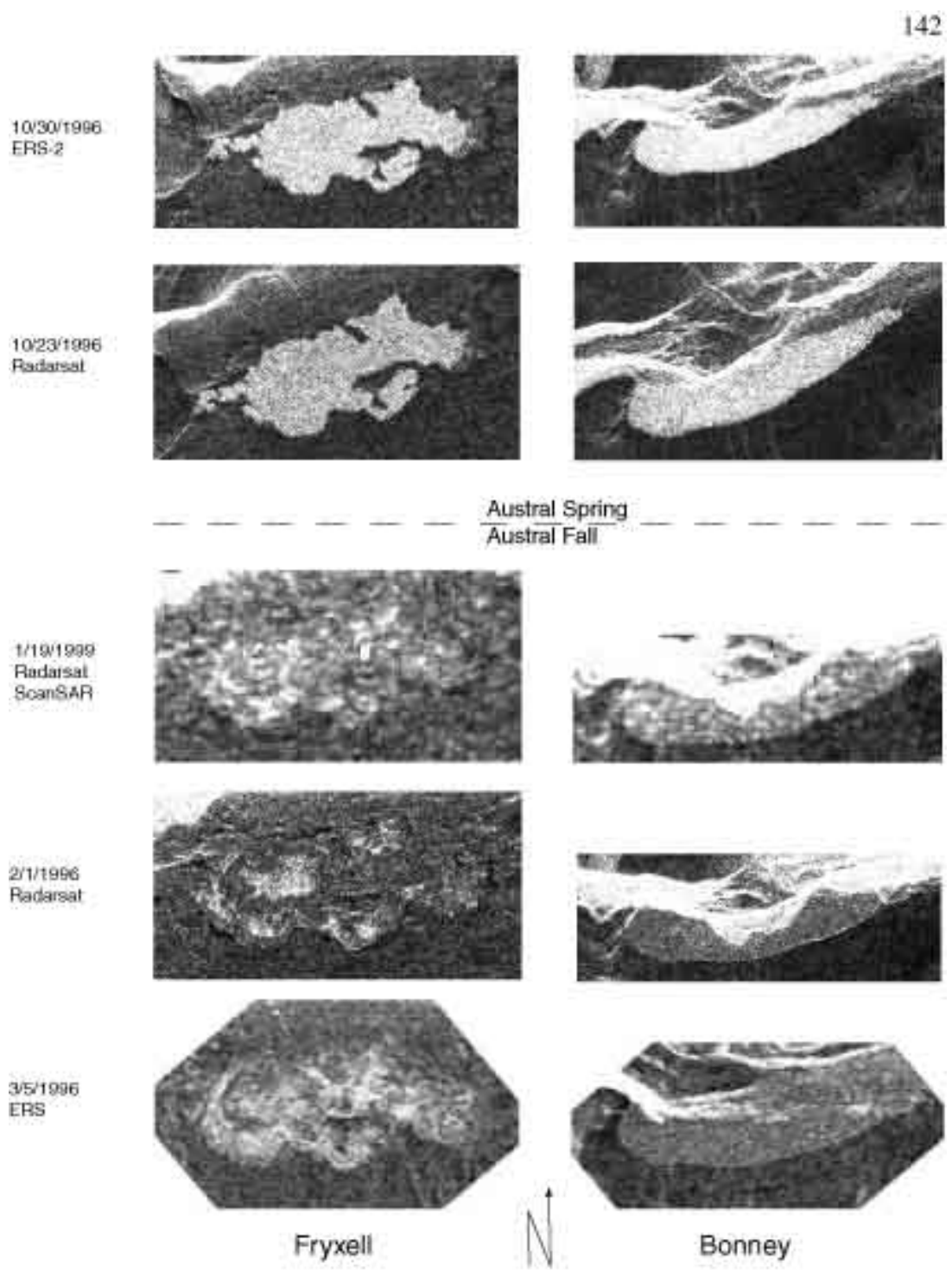


Figure 7.25: Comparison of backscatter of lake surfaces t t season.

